

FEDERAL ASSISTANCE PROGRAM/PROJECT STATUS REPORT

Replaces EIA-459F

All Other Editions Are Obsolete

OMB Burden Disclosure Statement

Public reporting burden for this collection of information is estimated to average 47.5 hours per response, including the time for reviewing instructions, searching existing data sources, gathering and maintaining the data needed, and completing and reviewing the collection of information. Send comments regarding this burden estimate or any other aspect of this collection of information, including suggestions for reducing this burden, to Office of Information Resources Management, AD-241.2 - GTN, Paperwork Reduction Project (1910-0400), U.S. Department of Energy, 1000 Independence Avenue, S.W., Washington, DC 20585; and to the Office of Management and Budget (OMB), Paperwork Reduction Project (1910-0400), Washington, DC 20503.

1. Program/Project Identification No. DE-FC26-00-NT40916	2. Program/Project Title: FUNDAMENTALS OF NATURAL GAS AND SPECIES FLOWS FROM HYDRATE DISSOCIATION - APPLICATIONS TO SAFETY AND SEA FLOOR INSTABILITY	3. Reporting Period <u>October 2002</u> through <u>September 2003</u>
4. Name and Address Goodarz Ahmadi Department of Mechanical and Aeronautical Engineering Clarkson University Potsdam, NY 13699-5725		5. Program/Project Start Date: November 2000 6. Completion Date October 2004
7. Approach Changes None 9 None		
8. Performance Variances, Accomplishments, or Problems Semi-analytical 1-D and axisymmetric computational models for natural gas flow in the hydrate reservoir were developed. Variations of pressure and temperature profiles, as well as the movement of dissociation front and amount of natural gas production were evaluated. An experimental setup for formation and dissociation of hydrate, which allows for the visual inspection of the process was developed. Variations of gas pressure and temperature during hydrate formation and dissociation processes in crushed ice and mixture of crushed ice and glass beads were measured. Fabrication of the shear flow device was completed and preliminary experimentation of shearing of liquid flows were performed. Formulation of a thermodynamically consistent model for multiphase liquid-gas flows in porous media was completed. Progress was made in the formulation of a thermodynamically consistent model for multiphase flows during hydrate dissociation. Progress was also made in the analysis of the case of dense liquid-solid mixture flows over a slope.		
9. Open Items 9 None		
10. Status Assessment and Forecast No Deviation from Plan is Expected 9X No Deviation from Plan is Expected		
11. Description of Attachments Detail progress report 9 None		
12. Signature of Recipient and Date Goodarz Ahmadi, September 7, 2003	13. Signature of U.S. Department of Energy (DOE) Reviewing Representative and Date	

DOE DE-FG26-00NT-40916

THIRD YEAR PROGRESS REPORT

September 2003

TITLE: **Fundamentals of Natural Gas and Species Flows from Hydrate Dissociation - Applications to Safety and Sea Floor Instability**

PI: Goodarz Ahmadi

INSTITUTION: Clarkson University
Potsdam, NY 13699-5725
Tel: (315) 268-2322
Fax: (315) 268-6438
Email: ahmadi@clarkson.edu

GRANT NO.: DE-FC26-00-NT40916

PERIOD OF

PERFORMANCE: October 1, 2002 to September 30, 2003

PROJECT DURATION: November 1, 2000 to October 31, 2004

DISCLAIMER

“This report was prepared as an account of work sponsored by an agency of the United States Government. Neither the United State Government nor any agency thereof, nor any of their employees, makes any warranty, express or implied, or assume any legal liability or responsibility for the accuracy, completeness, or usefulness of any information, apparatus, product, or process disclosed, or represents that its use would not infringe privately owned right. Reference herein to any specific commercial product, process, or service by trade name, trademark, manufacturer, or otherwise does not necessarily constitute or imply its endorsement , recommendation, or favoring by the United State Government or any agency thereof. The views and opinions of authors expressed herein do not necessarily state or reflect those of the United State Government or any agency thereof.”

TITLE: **Fundamentals of Natural Gas and Species Flows from Hydrate Dissociation - Applications to Safety and Sea Floor Instability**

PI: Goodarz Ahmadi

INSTITUTION: Clarkson University
Potsdam, NY 13699-5725
Tel: (315) 268-2322
Fax: (315) 268-6438
Email: ahmadi@clarkson.edu

GRANT NO.: DE-FC26-00-NT40916

PERIOD OF

PERFORMANCE: October 1, 2002 to September 30, 2003

PROJECT DURATION: November 1, 2000 to October 31, 2004

DOE Project Officer: Dr. Thomas Mroz/Dr. John Rogers

ABSTRACT

In the third year of the project major progresses were made in various tasks of the project. Semi-analytical computational models for natural gas flow in hydrate reservoirs were developed and the effects of variations in porosity and permeability on pressure and temperature profiles and the movement of a dissociation front were studied. Experimental data for variations of gas pressure and temperature during propane hydrate formation and dissociation for crushed ice and mixture of crushed ice and glass beads under laboratory environment were obtained. The experimental setup for shear flow device was fabricated and preliminary experiments on liquid phase shearing were performed. A thermodynamically consistent model for multiphase liquid-gas flows through porous media was developed. Numerical models for hydrate dissociation process in linear and axisymmetric reservoirs were developed. Progress was made in studying dense two-phase solid-liquid mixture flows over an inclined chute at different angles of orientations. The model predictions are compared with the experimental data and good agreement was found. Analysis of gas-liquid flows in fractures was also initiated.

TABLE OF CONTENTS

	Page
FEDERAL ASSISTANCE PROGRAM/PROJECT STATUS REPORT	i
TITLE PAGE	ii
DISCLAMER	iii
ABSTRACT	1
TABLE OF CONTENTS	2
INTRODUCTION	3
Objectives	3
Significance	4
RESUTLS AND DISCUSSIONS	4
Axisymmetric Reservoir Condition during Hydrate Dissociation	4
Thermodynamically Consistent Model for	
Multiphase Flows in Porous Media	24
Multiphase Flows	45
Experimental Hydrate Formation and Dissociation	
in Unconsolidated Media	55
Experimental Shear Flow Device	88
PLANS FOR NEXT YEAR	90
REFERENCES	91

INTRODUCTION

Objectives

The general objective of this project is to provide the needed fundamental understanding of natural gas-water-solid mixture flows in the reservoir during hydrate dissociation. One main goal is to understand the nature of loss of strength and the potential for sea floor instability due to hydrate dissociation in an unconsolidated reservoir. The other main goal is to develop an advanced computational capability for handling the safety issues related to natural gas production and pressure buildup during drilling into a hydrate reservoir. The specific objectives are:

- To develop a model for multiphase flows of natural gas-water with and without solid particles for application to natural gas production from hydrate dissociation in consolidated and unconsolidated reservoirs.
- To provide reliable data for phasic mean velocities during the dissociation of the propane hydrate in an experimental hydrate chamber, as well as in the shear flow device.
- To establish the material parameters of the model including the relative permeability in terms of the physical properties of the hydrate reservoir and dissociation conditions.
- To develop an accurate computational capability incorporating the new model for analyzing natural gas, water and/or slurry flows in configurations of interest to natural gas production from hydrate reservoir and during drilling.
- To solve a number of technologically important safety-related problems relevant to gas pressure buildup and gas-water mixture flows during drilling into a reservoir due to hydrate dissociation.
- To assess the potential for sea floor instability due to hydrate dissociation in unconsolidated sediment as a result of loss of strength and soil liquefaction process.
- To verify the validity of the developed model by comparing the predicted results with the experimental data under idealized conditions and the available field observation.

Significance

The current state of understanding of hydrate dissociation process is in its infancy. In particular, the nature of gas-liquid and solid flows in consolidated and unconsolidated sediments during the hydrate dissociation is not well understood. In addition, a satisfactory computational model describing the natural gas production and pressure buildup during the drilling into a hydrate reservoir does not exist. The goal of this project is to provide the needed fundamental understanding of the flow properties and such a computational model. We plan to make use of the thermodynamically consistent modeling approach of multiphase mixture flows, in addition to innovative experimentation. A fundamental understanding of multiphase flow during hydrate dissociation will have a significant impact on the safety of fissile fuel exploration and to the future development of environmentally acceptable hydrate-based energy production.

RESULTS AND DISCUSSIONS

Axisymmetric Reservoir Condition during Hydrate Dissociation

We have performed a new study concerning natural gas production with constant well output from a hydrate reservoir. This case is more realistic as in practice the well output is expected to be kept at a constant rate. The case that the reservoir is partially saturated with hydrate and also contains pressurized natural gas is analyzed. The linearized form of the governing equations is used in the analysis. The special case that a well is drilled in an unbounded axisymmetric hydrate reservoir is studied. When the well output is at a fixed rate, a set of self-similar solutions for temperature and pressure distributions in the reservoir can be found. The approach leads to a system of coupled algebraic equations for the location of the decomposition front and the temperature and pressure at the front. This system of equation is then solved by an iterative scheme. Numerical results for time evolutions of pressure and temperature profiles in the hydrate reservoir, as well as the location of the front, are obtained for several well natural gas production rates and reservoir temperatures.

Mathematical Model

In this section, the mathematical formulations of the model for evaluation of pressure and temperature fields are summarized. Consider a hydrate reservoir with a fixed production rate depressurizing well as shown in Figure 1. The governing equation for the pressure distribution in the reservoir, which is obtained from the continuity equation and Darcy's law, is given as

$$\frac{k_n}{2\Phi_n\mu} \left(\frac{\partial^2 P_n^2}{\partial r^2} + \frac{1}{r} \frac{\partial P_n^2}{\partial r} \right) = \frac{\partial P_n}{\partial t} \quad (1)$$

where

$$\Phi_1 = (1 - \alpha) \Phi \quad (2)$$

$$\Phi_2 = (1 - \beta) \Phi \quad (3)$$

and r is the radial distance from the well, t is time, μ is the coefficient of viscosity of the gas, k_n is the gas permeability in zone 1 or 2, P_n is the pressure in zone 1 or 2, Φ is the reservoir porosity, α is the water saturation, and β is the hydrate saturation. In Equation (1) and in the subsequent analysis, $n = 1$ corresponds to the gas-region with $r_0 < r < R(t)$, and $n = 2$ denotes the hydrate-region with $R(t) < r < \infty$. Here $R(t)$ is the distance of the dissociation front from the center of well, and r_0 is the well radius.

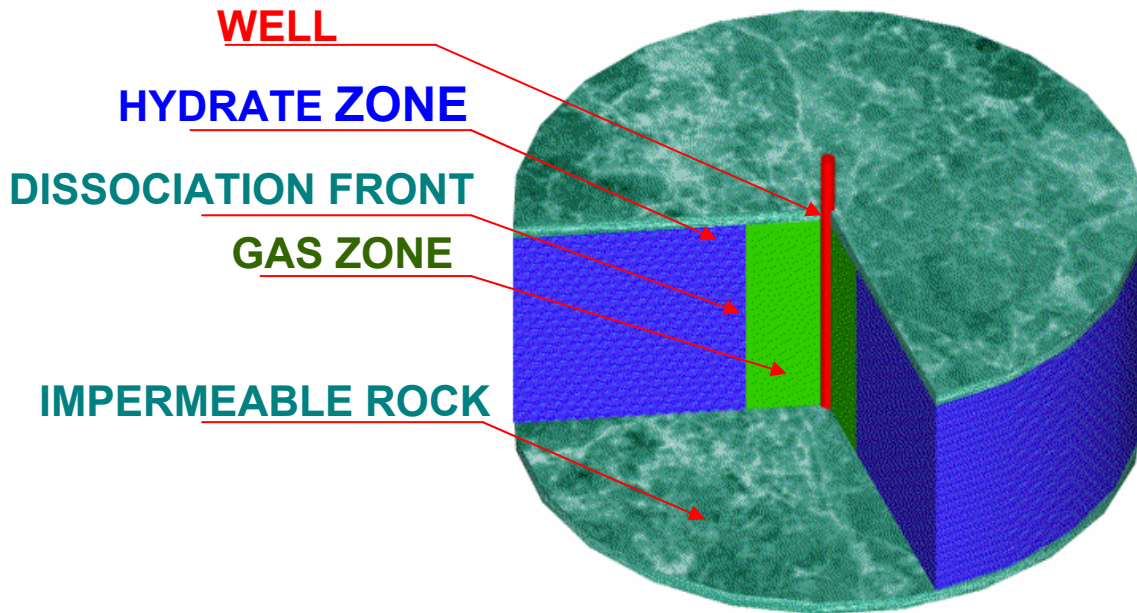


Figure 1. Schematics of a hydrate reservoir with a depressurizing well.

The relation between dissociation temperature T_D and pressure P_D at the decomposition front for phase equilibrium between natural gas and hydrate is given as

$$\log_{10} P_D = a (T_D - T_0) + b (T_D - T_0)^2 + c \quad (4)$$

where T_0 is 273.15K and a , b and c are empirical constants that depend on the hydrate composition. Values of a , b , and c are obtained using the least square error fit to the equilibrium pressure-temperature data for methane hydrate (Makogon, 1997, Ji et al. 2000). i.e.,

$$a = 0.0342 \text{ K}^{-1}, \quad b = 0.0005 \text{ K}^{-2}, \quad c = 6.4804$$

where in Equation (4) P_D is in Pa.

Ji et al. (2000) showed that the prediction of Equation (4) is in good agreement with the data of Marshal et al. (1964). The mass balance for gas at the decomposition front at the distance of $R(t)$ from the well is given as

$$\rho_1 v_1 - \rho_2 v_2 = -[\beta \varepsilon \rho_3 - (1 - \alpha) \rho_1 + (1 - \beta) \rho_2] \Phi \frac{dR}{dt} \quad (5)$$

where ρ_1 is the density of natural gas in zone 1, ρ_2 is the density of natural gas in zone 2, and ρ_3 is the density of hydrate, and ε is the mass fraction of methane gas in the hydrate. Here v_1 and v_2 are, respectively, the velocities of natural gas at the dissociation front in zones 1 and 2.

The densities of the natural gas in zone 1 and 2 at the dissociation front are described by the same equation:

$$\rho_1(R, t) = \rho_2(R, t) = \rho_0 \frac{P_D T_0}{z P_0 T_D} \quad (6)$$

where z is the gas compressibility (deviation) factor, and ρ_0 is the gas density at standard pressure P_0 and temperature T_0 . Insertion of (6) into (5) gives

$$v_1(R, t) - v_2(R, t) = -[\varepsilon \beta \frac{\rho_3 P_0 T_D}{\rho_0 P_D T_0} z - (\beta - \alpha)] \Phi \frac{dR}{dt} \quad (7)$$

Similarly, the mass balance equation for water is:

$$\rho_w \Phi \alpha = (1 - \varepsilon) \rho_3 \Phi \beta \quad (8)$$

where ρ_w is the density of water.

The temperature field is governed by the convective-conductive heat transfer equation

$$\frac{a_n}{r} \frac{\partial}{\partial r} \left(r \frac{\partial T_n}{\partial r} \right) = \frac{\partial T_n}{\partial t} - \frac{c_v k_n}{c_n \mu} \frac{\partial P_n}{\partial r} \left(\frac{\partial T_n}{\partial r} - \delta \frac{\partial P_n}{\partial r} \right) - \eta \frac{\Phi_n c_v}{c_n} \frac{\partial P_n}{\partial t} \quad (9)$$

Here a_n is the heat diffusivity, c_n is the heat capacity, c_v is the constant volume heat capacity of gas, δ is the throttling coefficient, and η is the adiabatic coefficient of the gas. Note that the Joule-Thompson throttling process is accounted for in Equation (9).

For wells with a fixed natural gas output, Q , the boundary conditions are

$$Q = 2\pi r_0 h \frac{k_1}{\mu} \left[\rho \frac{\partial P_1}{\partial r} \right]_{r=r_0} = \frac{\pi k_1 h}{\mu} \frac{\rho_0}{P_0} \left[r \frac{\partial P_1^2}{\partial r} \right]_{r=r_0} = \frac{\pi k_1 h}{\mu} \frac{\rho_0}{P_0} c_1 \quad (10)$$

$$P_2(r, 0) = P_2(\infty, t) = P_e \quad (11)$$

$$P_1(R(t), t) = P_2(R(t), t) = P_D(T_D) \quad (12)$$

$$T_2(r, 0) = T_2(\infty, t) = T_e \quad (13)$$

$$T_1(R(t), t) = T_2(R(t), t) = T_D \quad (14)$$

where h is the thickness of the hydrate reservoir and c_1 is a constant (related to the pressure gradient at the well wall). As noted before, it is assumed that the dissociation front is at the equilibrium pressure and temperature (P_D and T_D) for dissociation of the hydrate

Linearization and Self-Similar Solution

To be able to obtain similar solutions, the governing equations must be first linearized. Here the reservoir and the dissociation pressures are, respectively, used to linearize the pressure equation in the hydrate and the gas zones. That is, using the approximation

$$\frac{\partial P_1^2}{\partial t} \approx 2P_D \frac{\partial \bar{P}_1}{\partial t} \quad \frac{\partial P_2^2}{\partial t} \approx 2P_e \frac{\partial \bar{P}_2}{\partial t} \quad (15)$$

Equation governing the pressure variation may then be linearized as:

$$\frac{\partial \bar{P}_n^2}{\partial r^2} + \frac{1}{r} \frac{\partial \bar{P}_n^2}{\partial r} = \frac{1}{\chi_n} \frac{\partial \bar{P}_n^2}{\partial t} \quad (16)$$

where

$$\chi_1 = \frac{k_1 P_D}{\mu \Phi_1} \quad \chi_2 = \frac{k_2 P_e}{\mu \Phi_2} \quad (17)$$

Self-similar solutions of Equation (16) with appropriate boundary conditions are:

$$\bar{P}_1^2 = P_D^2 - \frac{Q\mu}{2\pi k_1 h} \frac{P_0}{\rho_0} [E_i(-\lambda_1^2) - E_i(-\alpha_1^2)] \quad (18)$$

$$\bar{P}_2^2 = P_e^2 - (P_e^2 - P_D^2) \frac{E_i(-\lambda_2^2)}{E_i(-\alpha_2^2)} \quad (19)$$

where

$$E_i(-\xi) = -\int_{\xi}^{\infty} \frac{e^{-u}}{u} du \quad (20)$$

$$\lambda_1 = \frac{r}{2\sqrt{\chi_1 t}} \quad \lambda_2 = \frac{r}{2\sqrt{\chi_2 t}} \quad (21)$$

$$\alpha_1 = \sqrt{\frac{\gamma}{4\chi_1}} \quad \alpha_2 = \sqrt{\frac{\gamma}{4\chi_2}} \quad (22)$$

Under the condition that the hydrate reservoir contains free natural gas, neglecting the conductive heat transfer in the porous media, which is several orders of magnitude smaller than the convective heat transfer, the heat transfer equation becomes

$$\frac{\partial T_n}{\partial t} = \frac{c_v k_n}{c_n \mu} \frac{\partial P_n}{\partial r} \left(\frac{\partial T_n}{\partial r} - \delta \frac{\partial P_n}{\partial r} \right) + \eta \frac{\Phi_n c_v}{c_n} \frac{\partial P_n}{\partial t} \quad (23)$$

Similarly, solutions to the linearized form of Equation (23) satisfying the appropriate thermal boundary conditions are:

$$T_1 = T_D + A_1 \delta \left[E_i(-\lambda_1^2) - E_i(-\alpha_1^2) + \left(\frac{\eta}{\delta} B_1 - 1 \right) (\Psi_1(\lambda_1^2) - \Psi_1(\alpha_1^2)) \right] \quad (24)$$

$$T_2 = T_e + A_2 \delta \left[E_i(-\lambda_2^2) - \left(\frac{\eta}{\delta} B_2 - 1 \right) \Psi_2(\lambda_2^2) \right] \quad (25)$$

where

$$\Psi_1(\xi) = \int_0^{\xi} \frac{e^{-\eta}}{\eta + C_1 e^{-\eta}} d\eta \quad \Psi_2(\xi) = \int_{\xi}^{\infty} \frac{e^{-\eta}}{\eta + C_2 e^{-\eta}} d\eta \quad (26)$$

$$A_1 = \frac{Q\mu P_0}{4\pi P_D k_1 \rho_0 h}; \quad A_2 = -\frac{1}{2E_i(-\alpha_2^2)} \frac{P_e^2 - P_D^2}{P_e} \quad (27)$$

$$B_1 = \frac{\Phi_1 c_v}{c_1}; \quad B_2 = \frac{\Phi_2 c_v}{c_2} \quad (28)$$

$$C_1 = \frac{Qc_v P_0}{4\pi P_D c_1 \chi_1 h \rho_0}; \quad C_2 = -\frac{P_e^2 - P_D^2}{P_e} \frac{c_v}{c_2} \frac{1}{2E_i(-\alpha_2^2)} \frac{k_2}{\mu \chi_2} \quad (29)$$

The values of pressure P_D and temperature T_D at the dissociation front, and the constant γ , which determines the motion of the decomposition front, are still unknown and must be evaluated numerically for a given set of conditions. From the evaluation of Equation (25) at the decomposition front (i.e. $\lambda_2 = \alpha_2$), it followed that

$$T_D = T_e + A_2 \delta [E_i(-\alpha_2^2) - (\frac{\eta}{\delta} B_2 - 1) \Psi_2(\alpha_2^2)] \quad (30)$$

The equilibrium pressure P_D and the equilibrium temperature T_D are related. Using Equations (18) and (19), the balance of mass at the decomposition front becomes:

$$Q \frac{P_0}{\pi} \frac{e^{-\alpha_1^2}}{h \rho_0} + \frac{2k_2}{\mu} (P_e^2 - P_D^2) \frac{e^{-\alpha_2^2}}{E_i(-\alpha_2^2)} = A\gamma \quad (31)$$

where

$$A = [\varepsilon \beta \frac{\rho_3 P_0 T_D}{\rho_0 T_0} z - (\beta - \alpha) P_D] \Phi \quad (32)$$

Equation (31) may be used to determine the constant γ . Equations (31) and (32) and the relationship between the dissociation temperature and pressure given by Equation (4) are three nonlinear coupled equations for determining γ , T_D and P_D .

The linearization model described in this section that was suggested by Makogon (1997) assumes that the heat convection dominates the conduction and the neglects the heat conduction in the entire reservoir. While this assumption is reasonable away from the dissociation front, it does not allow for the energy balance at the dissociation front to be enforced. Despite this important limitation of the approach, the linearization method provides for a convenient (semi-analytical) method for studying many features of the natural gas production from hydrate reservoirs.

Results

In this section, results for the time evolution of pressure and temperature profiles in the hydrate reservoir due to the presence of a well with different fixed natural gas outputs are presented. In addition, time variations of location of the dissociation front are also evaluated. An initial reservoir pressure of 15MPa is used in these simulations. For different values of well-output and initial reservoir temperatures, the solutions to Equations (31)-(33) are obtained. The resulting values of the dissociation temperature and pressure at the front and of the parameter γ (with an error bound of 0.1%) are listed in Table 1. Here the permeability in the gas zone is 5.2 md and the hydrate zone permeability is 0.4 md.

Table 1. Values of dissociation temperature and pressure and parameter γ for different natural gas production rates for a reservoir with $k_1=5.2$ md and $k_2=0.4$ md.

P_e (MPa)	T_e (K)	Natural Gas Output(kg/s)	T_D (K)	P_D (MPa)	γ (m^2/sec)
15	283	0.03	277.25	4.314	1.61×10^{-6}
15	285	0.03	279.46	5.526	2.45×10^{-6}
15	287	0.04	281.96	6.65	2.71×10^{-5}
15	287	0.03	281.96	6.647	4.67×10^{-6}
15	287	0.02	281.93	6.628	1.4×10^{-7}
15	287	0.01	281.92	6.61	2.51×10^{-8}

When the reservoir pressure, temperature and production rates are specified, the present linearized axisymmetric model leads to fixed values of dissociation-front pressure and temperature. The well pressure, however, changes gradually with time. Table 1 shows that for a fixed reservoir temperature of 287K, when the natural gas output decreases, the dissociation pressure and temperature decrease slightly. The value of parameter γ , which controls the movement of the dissociation front, however, decreases sharply as the gas production decreases. The dissociation pressure and temperature are sensitive functions of reservoir temperature. When the gas production is kept fixed at 0.03 kg/s, a decrease of 2K in the reservoir temperature drops the dissociation pressure by about 17%. In this case, parameter γ also decreases with the decline of reservoir temperature.

For a reservoir temperature of 287K and a natural gas production rate of 0.04 kg/s, variations of decomposition temperature and pressure, and parameter γ with zone permeability are shown in Table 2. When the permeability in the gas zone is fixed at 5.2 md, as the hydrate zone permeability decreases from 3 md to 0.4 md, the dissociation pressure and temperature decrease slightly, while parameter γ increases sharply. This is because,

when the hydrate zone permeability is low, the amount of hydrate that needs to dissociate increases to maintain the well gas flow at a fixed rate. When the permeability in the hydrate zone is fixed, variations of gas zone permeability have a very slight effect on the dissociation temperature, pressure and parameter γ . As noted before, here the natural gas output is fixed, and therefore, the equilibrium conditions at the front do not change appreciably. The main effect of variations of gas zone permeability is on the temperature and pressure profiles, which will be discussed later.

Table 2. Values of dissociating temperature and pressure and parameter γ for a natural gas production rate of 0.04 kg/s for different zone permeabilities

P_e (MPa)	Permeability of gas zone(md)	Permeability of Hydrate zone(md)	T_D (K)	P_D (MPa)	γ (m^2/sec)
15	5.2	3	282.038	6.7	4.96×10^{-10}
15	5.2	1	281.976	6.66	2.5×10^{-8}
15	5.2	0.6	281.964	6.65	2.9×10^{-6}
15	5.2	0.4	281.963	6.65	2.71×10^{-5}
15	1	1	281.978	6.66	2.51×10^{-8}

For a reservoir temperature of 287K and a natural gas production rate of 0.04kg/s, Figure 2 shows variations of pressure and temperature profiles at different times. Here the case that the permeabilities in the hydrate and gas zones are, respectively, 5.2 md and 0.4 md is consider. As noted before, the hydrate reservoir is divided into two zones by the dissociation front, and the temperature variations in the two zones are quite different. Figures 2a and 2b show that the temperature decreases gradually from the undisturbed reservoir value far from the front to the dissociation temperature at the front. In the gas zone, the temperature varies gradually near the dissociation front, but decreases sharply to its minimum values at the well. The temperature profiles in the hydrate and the gas zones are also self-similar, and evolve with time as the decomposition front moves outward.

The corresponding pressure profiles for different times under the same conditions for the far and the near fields are presented in Figures 2c and 2d. The pressure decreases gradually from the reservoir pressure to the decomposition pressure at the front, and then decreases toward the well to its minimum value at the well. Near the well, the pressure gradient becomes quite high.

For the present case where the permeability of the gas zone is thirteen times that of the hydrate zone, the change in the slope of the pressure profile at the dissociation front can be clearly seen from Figure 2c. This is quite different from the one-dimensional model of Ji et

al. (2000), in which the gradient change at the front was hardly noticeable. It should be emphasized that in the earlier study of Ji et al. (2000), the permeability in the gas zone was almost the same as that in the hydrate zone. Figure 2c also shows that the pressure profiles for different times are self-similar in each zone, and expand outward as the dissociation front moves away from the well.

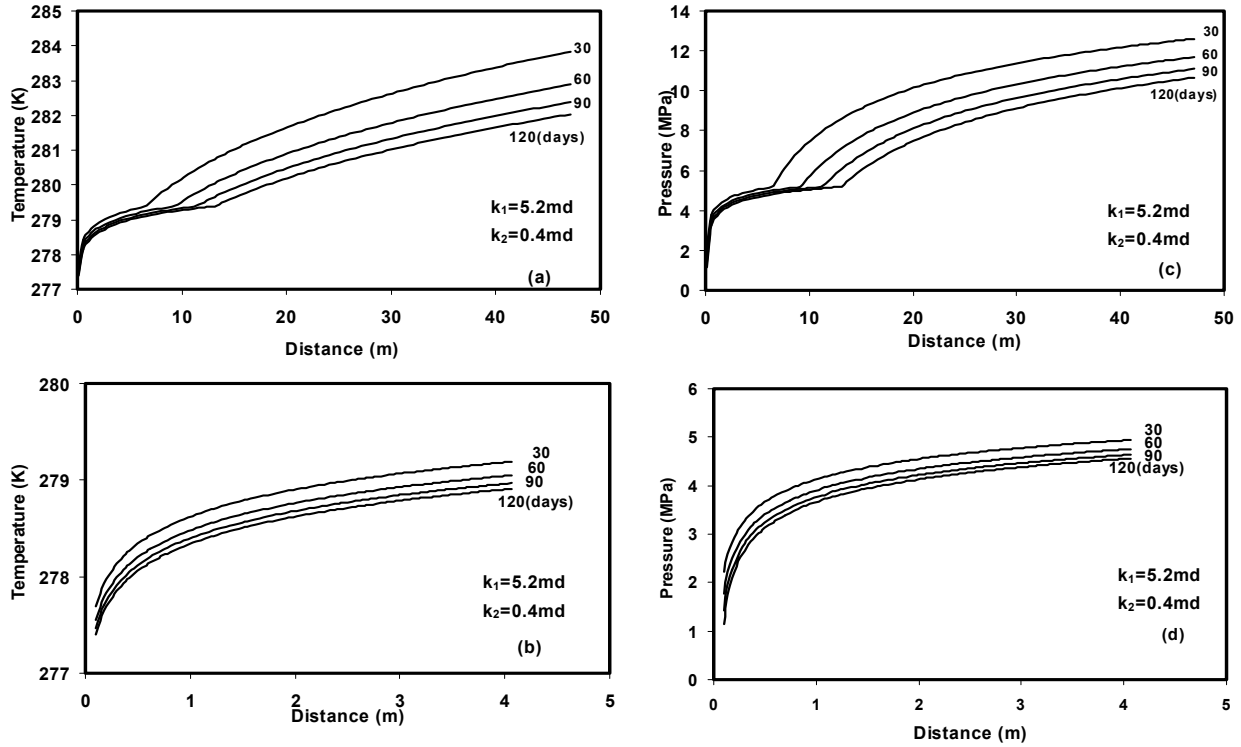


Figure 2. Time variations of pressure and temperature profiles for a reservoir temperature of 287K and a well natural gas output of 0.04kg/s. (a), (c) extended field. (b),(d) near-well.

Figure 2d shows that the pressure at the well drops with time when the natural gas output is kept fixed (at 0.04kg/s). That is, to maintain a constant gas output, the well pressure must be reduced continuously with time. Obviously, this can not continue forever, and after certain time, the pressure at the well becomes too low to allow maintaining a constant flow rate.

For a natural gas production rate of 0.04 kg/s, the time evolutions of the gas mass flux (Dv) and the total mass flow ($2BrDv$) across the reservoir are displayed, respectively, in Figure 3a and 3b. Figure 3a shows that the gas mass flux increases toward the well, and the variation in each zone is roughly time independent. This figure also clearly shows the details

of natural gas production at the dissociation front. At the front, there is a jump in the mass flux due to hydrate decomposition. The jump moves outward with time as the decomposition front penetrates deeper into the hydrate reservoir.

Mass flux and total mass flow profiles for a reservoir temperature of 287K and a well natural gas output of 0.04kg/s are shown in Figure 3. Figure 3b shows the time variation of the total mass flow per unit length at a radial distance of r from the well. The total mass flow profiles in the hydrate and the gas zones remain roughly fixed, except for the jump at the dissociation front. This figure clearly shows the variation of the amount of natural gas generated by hydrate dissociation at the front. There is also a slight decrease in the gas flow in the hydrate zone that is compensated by the slight increase in the gas production by dissociation at the front. Figure 3a indicates that the mass flux due to hydrate dissociation decreases with time. On the other hand, Figure 3b indicates that the total mass flow due to hydrate dissociation remains fixed (or increases slightly) with time.

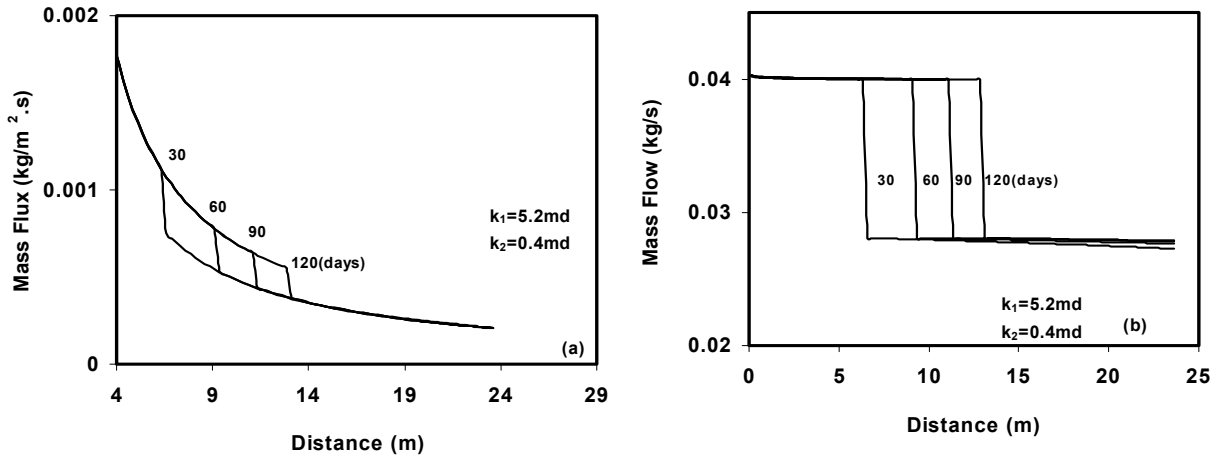


Figure 3. Mass flux and total mass flow profiles for a reservoir temperature of 287K and a well natural gas output of 0.04kg/s.

Figure 4 shows the pressure and temperature profiles for a natural gas production rate of 0.03kg/s in a reservoir with permeabilities in the hydrate and gas zones being equal to 5.2md and 0.4md. The reservoir pressure and temperature are kept constant at 15 MPa and 287 K. This figure shows that large pressure and temperature gradients occur near the front on the hydrate side. The pressure and temperature in the gas region then decrease gradually toward their minimum values at the well. The pressure and temperature profiles in gas zone in Figure 4 are similar to those shown in Figure 2 with certain differences. In addition to the slower movement of the dissociation front for the lower well output in this case, the temperature and pressure gradients near the well become more gradual. Comparing Figures

2d and 4d shows that the time variation of the well pressure also becomes much slower when the gas output decreases. This implies that a constant well output of 0.03 kg/s can be maintained for a much longer time period when compared to that of 0.04 kg/s.

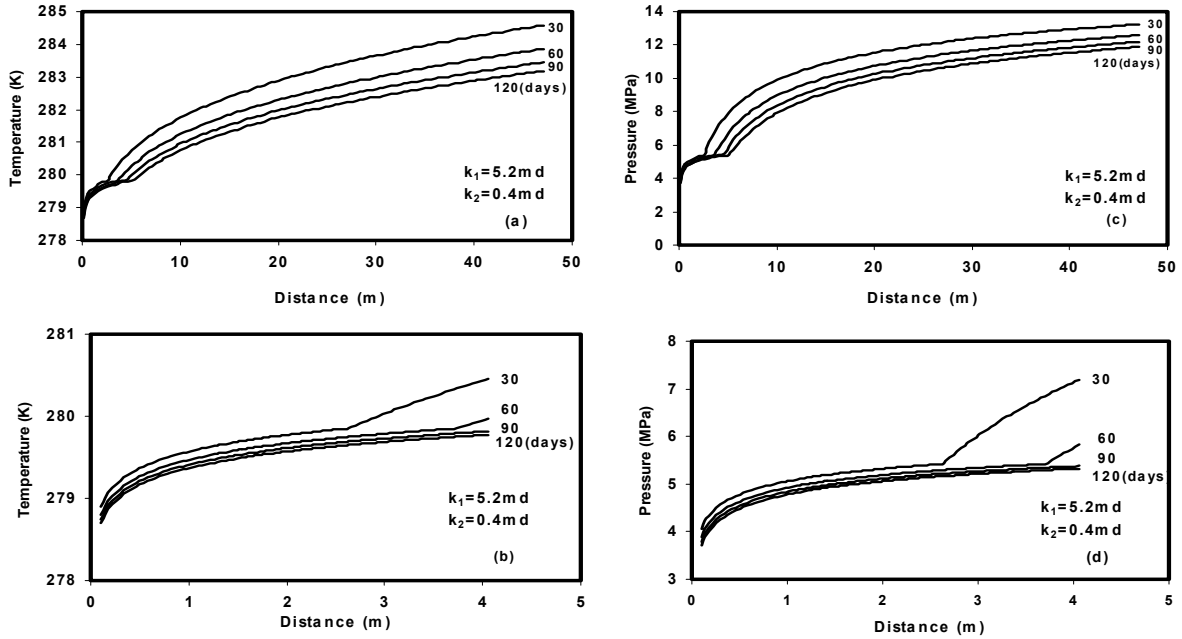


Figure 4. Time variations of pressure and temperature profiles for a reservoir temperature of 287K and a well natural gas output of 0.03kg/s. (a),(c) extended field. (b),(d) near-well.

Time evolutions of mass flux and total mass flow in the reservoir for a well output of 0.03 kg/s are shown in Figure 5. Except for the lower magnitudes, the mass flux and the total mass flow profiles are quite similar to those shown in Figure 3. The details of the hydrate dissociation at the front and the motion of the front can also be seen from this figure.

Under the same reservoir conditions, when the natural gas output is fixed at 0.02 kg/s, Figure 6 shows that the dissociation front moves at a much slower rate. Other features of pressure and temperature profiles in the hydrate zone are similar to those for higher well gas outputs. In this case, however, the pressure and temperature profiles in the hydrate zone have sharp gradients near the front. Figures 6b and 6d show the details of temperature and pressure profiles near the well. The temperature and pressure vary smoothly toward the well and decrease slightly with time. The corresponding mass flux and mass flow profiles are shown in Figure 7. The general features of these profiles are similar to those for higher well outputs. In this case, however, the dissociation front moves only a few meters after 120 days, but similar jumps in the mass flux and mass flow rate are observed.

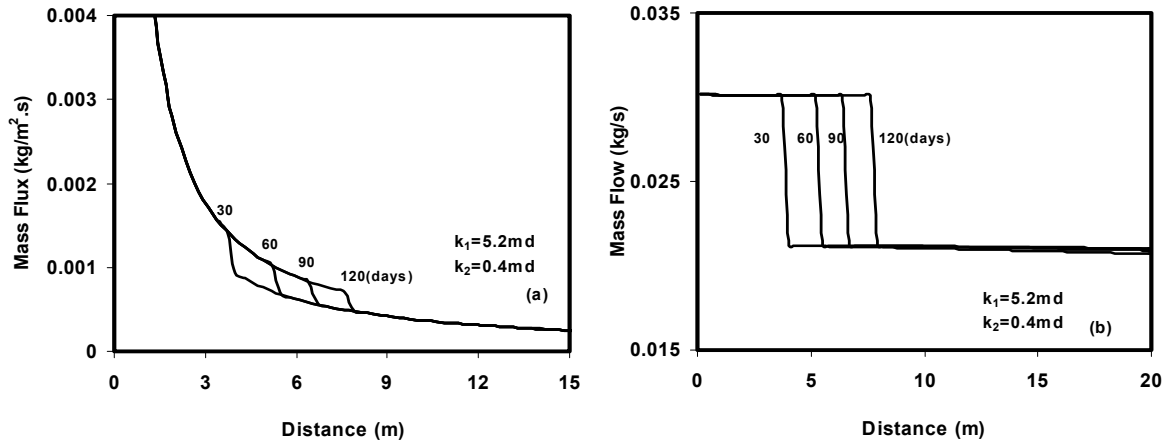


Figure 5. Mass flux and total mass flow profiles for a reservoir temperature of 287K and a well natural gas output of 0.03kg/s.

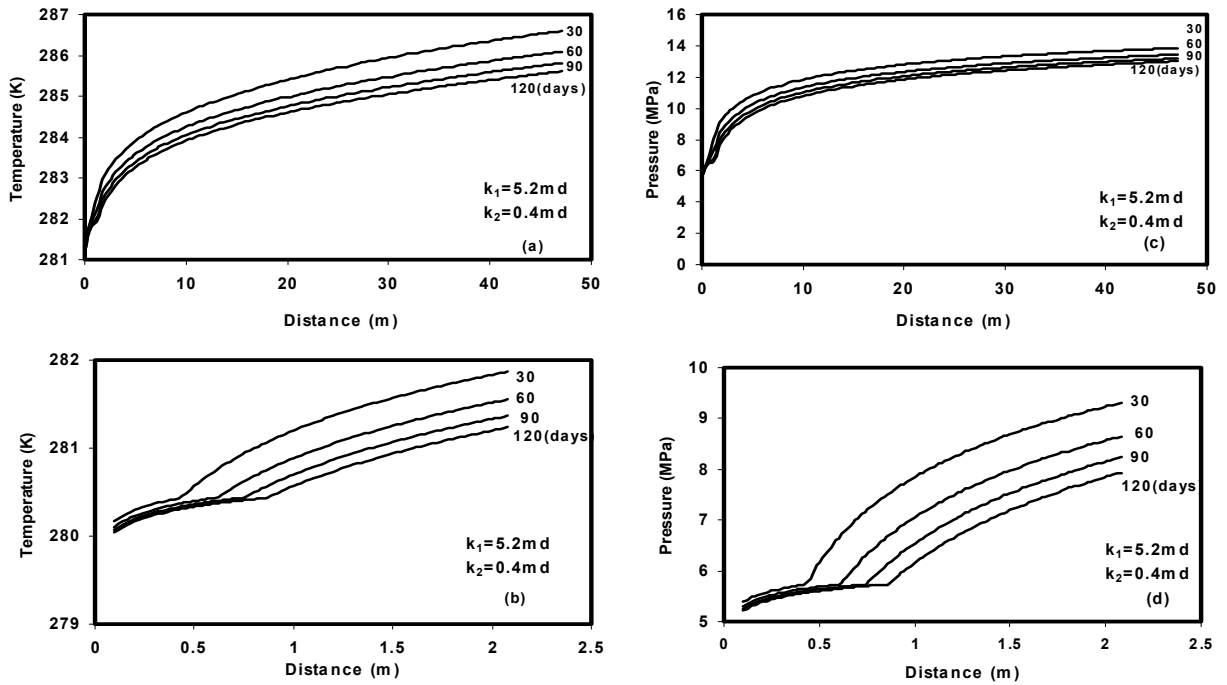


Figure 6. Time variations of pressure and temperature profiles for a reservoir temperature of 287K and a well natural gas output of 0.02kg/s. (a),(c) extended field. (b),(d) near-well.

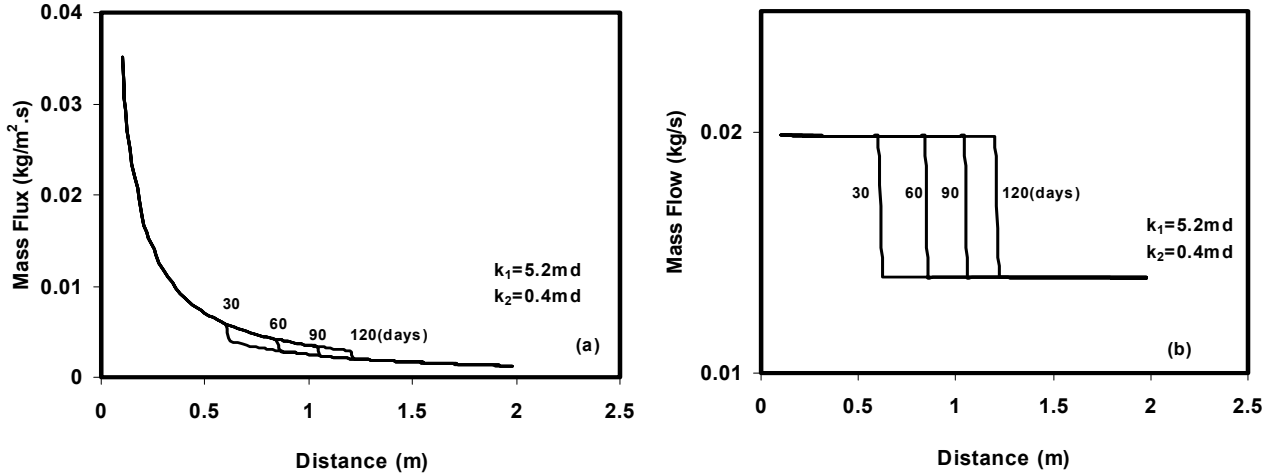


Figure 7. Mass flux and total mass flow profiles for a reservoir temperature of 287K and a well natural gas output of 0.02kg/s.

For the case that the natural gas output is kept fixed at 0.03kg/s, for a reservoir temperature of 285 K (2 K lower than the case shown in Figure 4), the pressure and temperature profiles are presented in Figure 8. The zone permeabilities are also kept the same. While the general features of the pressure and temperature profiles in Figure 8 are similar to those shown in Figure 4, the dissociation pressure and temperature at the front are somewhat smaller. The movement of the front has also noticeably slowed down for this lower-temperature reservoir. This observation further emphasizes the importance of heat transfer for hydrate dissociation and natural gas production processes. In this axisymmetric model, the heat required for hydrate dissociation must be supplied by the hydrate reservoir. Therefore, the reservoir temperature becomes an important controlling parameter. It should be emphasized that, for thin hydrate reservoirs, heat could also be supplied from the lower warmer region, which would significantly affect the natural gas production process.

Figure 9 shows the temperature and pressure profiles when the reservoir temperature is 283K, the other reservoir conditions are kept fixed, and the well output is 0.03 kg/s. Compared with Figure 4 and Figure 8, it is seen that the temperature and the pressure profiles are quite similar. However, due to the lower decomposition temperature and pressure, the rate of reduction of pressure at the well increases. In particular, Figure 9d shows that the well pressure becomes too low at about 120 days to maintain a constant gas output of 0.03 kg/s. Therefore, as the reservoir temperature decreases, the time duration that a fixed natural gas output can be maintained becomes shorter.

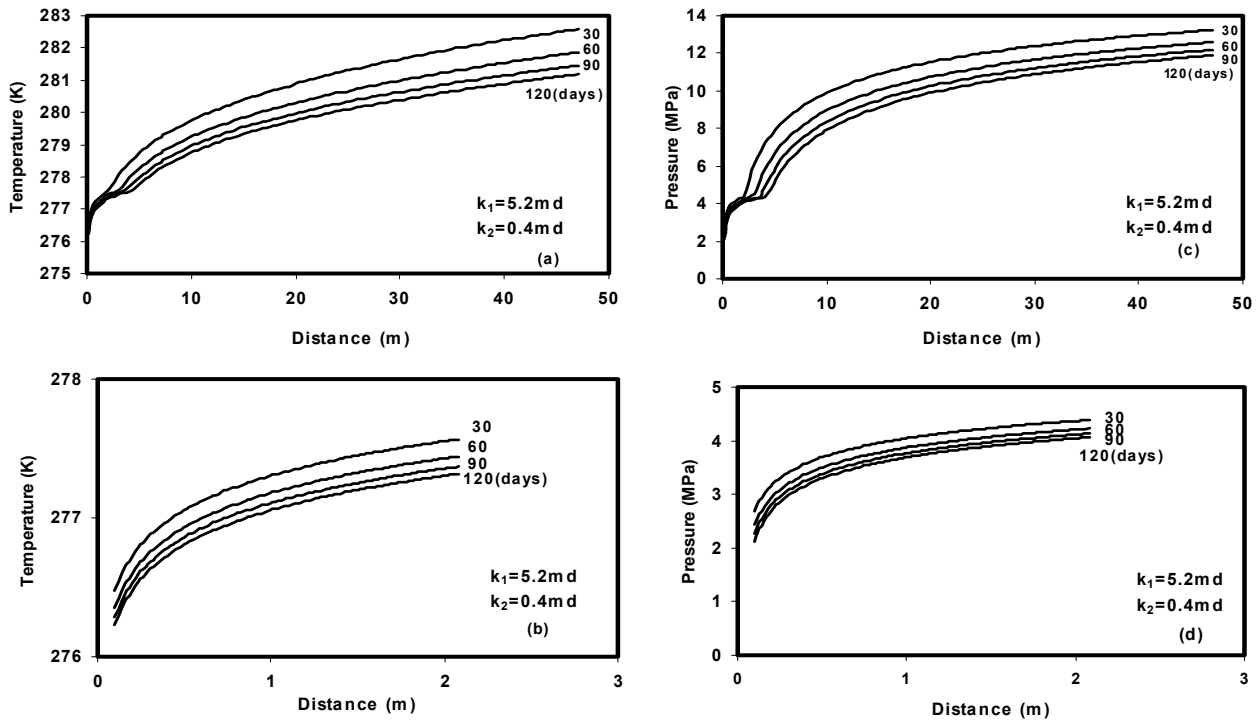


Figure 8. Time variations of pressure and temperature profiles for a reservoir temperature of 285K and a well natural gas output of 0.03kg/s. (a),(c) extended field. (b),(d) near-well.

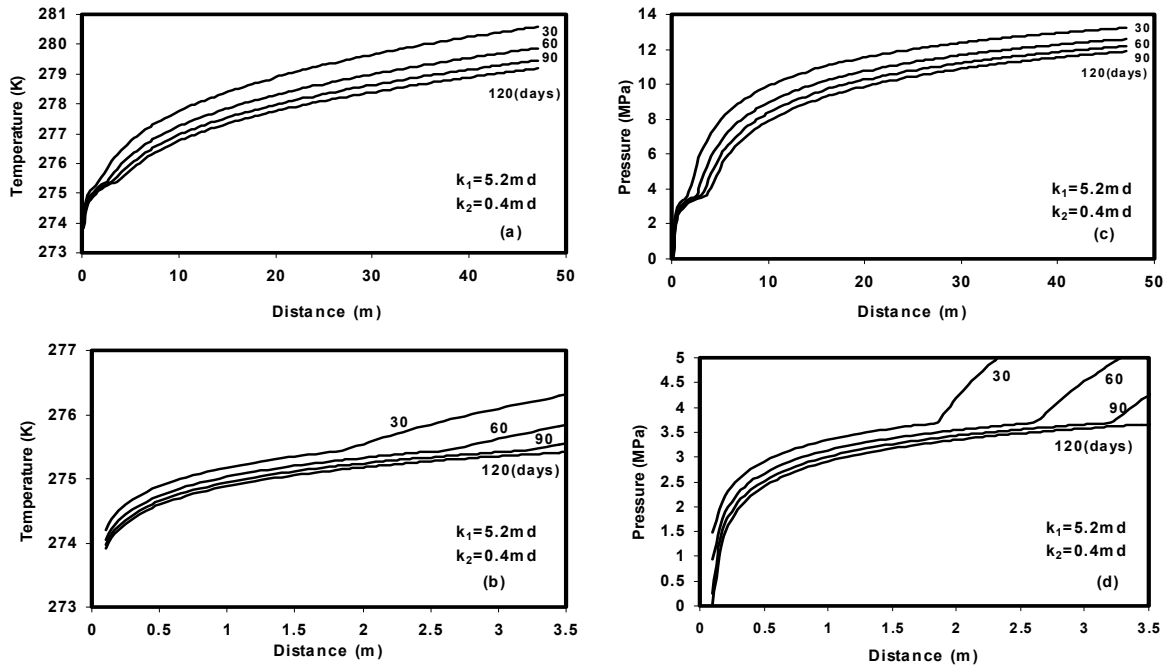


Figure 9. Time variations of pressure and temperature profiles for a reservoir temperature of 283K and a well natural gas output of 0.03kg/s. (a),(c) extended field. (b),(d) near-well.

Mass flux and mass flow profiles for reservoir temperatures of 283 K and 285 K are compared in Figure 10. While the mass flux jumps for different reservoir temperatures are comparable, the decomposition front moves faster as when the reservoir temperature is higher. Comparing Figures 5 and 10 shows the same trend of variations.

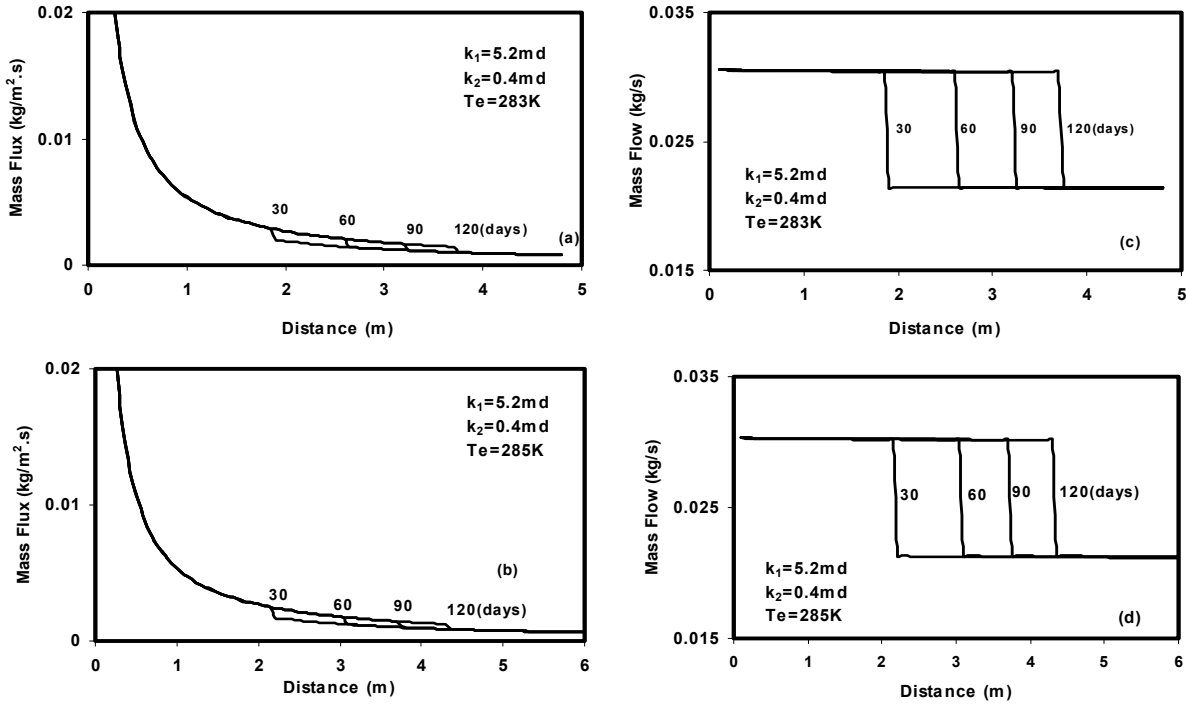


Figure 10. Mass flux and total mass flow profiles for a reservoir pressure of 15 MPa and a well natural gas output of 0.03 kg/s with different reservoir temperatures.

Effect of variations in zone permeability on the reservoir temperature and pressure profiles are shown in Figure 11. Here the case that the reservoir temperature is 287 K and the natural gas output is 0.04 kg/s is studied. Figure 11a and 11b shows the profile for the case that the permeabilities in the gas and hydrate zones are both 1 md. In this case the temperature has a smooth decreasing trend in the hydrate zone and decreases with a sharper slope in the gas zone. The pressure shows a gradual reduction in the entire reservoir, but with a sharper slope in the gas zone. Similar to the one-dimensional case reported by Ji et al. (2000), it is rather difficult to identify the change in slope in the pressure profile at the front when the zone permeabilities are equal.

Figures 11c and 11d show the profiles when the permeability in gas zone is 5.2 md and the hydrate zone permeability is 1 md. In this case, there is an obvious pressure gradient change at the dissociation front. From Equation (5), we expect that the gas flow out of front into the gas zone should be larger than the gas flow into the front from hydrate zone. While

at the dissociation front, the pressure gradient at the hydrate side is larger than that at the gas side difference in the zone permeability compensate and the flow rate is larger on the gas side.

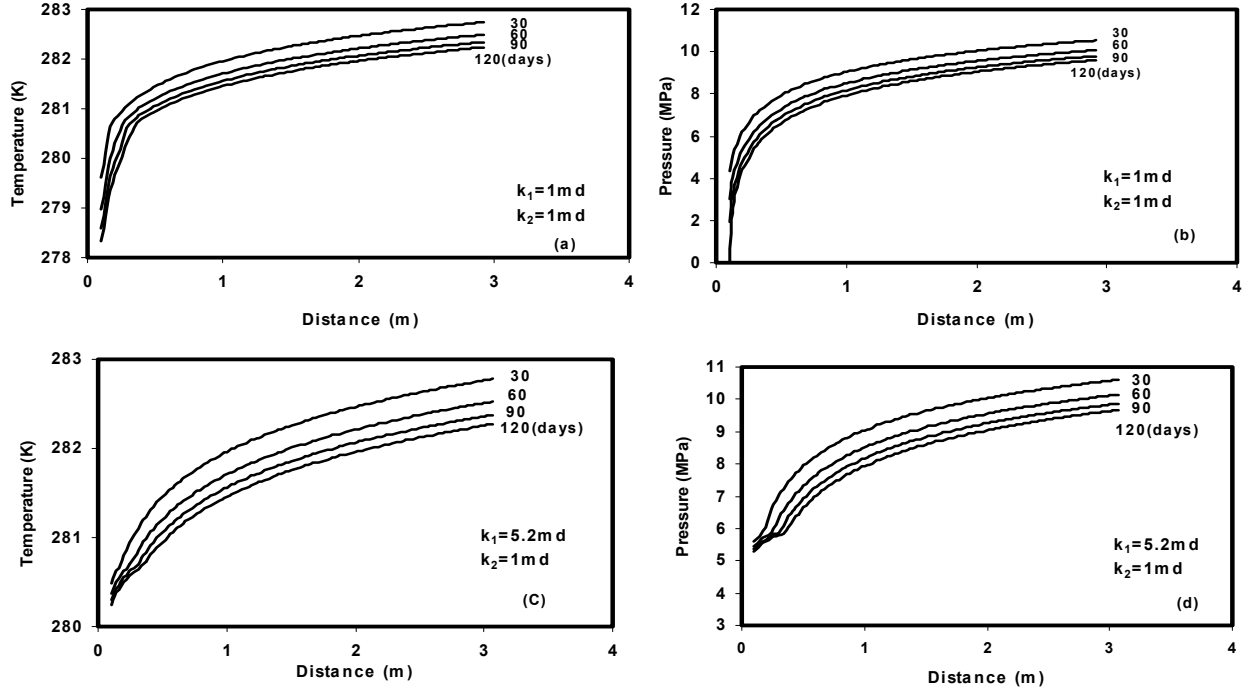


Figure 11. Time variations of pressure and temperature profiles for a reservoir temperature of 287K and a well natural gas output of 0.04kg/s with different permeabilities.

Figure 12 shows the effect of gas zone permeability on the mass flux and total mass flow profiles. The reservoir conditions are identical to those for Figure 11. Comparing Figures 12a and 12c indicates that the variation of gas zone permeability has little effect on the mass flux and total mass flow profiles, as well as the location of dissociation front. This observation shows that the variation of gas zone permeability only affects the reservoir temperature and pressure profiles, and its effect on hydrate dissociation at the decomposition front is slight.

Comparing Figures 3 and 12 shows that the hydrate zone permeability significantly affects the natural gas total mass flow profiles. For $k_2 = 0.4$ md, the front is at 15 m after 90 days, while for a reservoir with $k_2 = 1$ md the dissociation front is at about 0.5 m from well. That is, at a constant well mass flow rate, smaller k_2 , will lead to a faster penetration of the

front into the reservoir. This is because more hydrate needs to be dissociated to compensate for the lower gas flow rate in the hydrate zone.

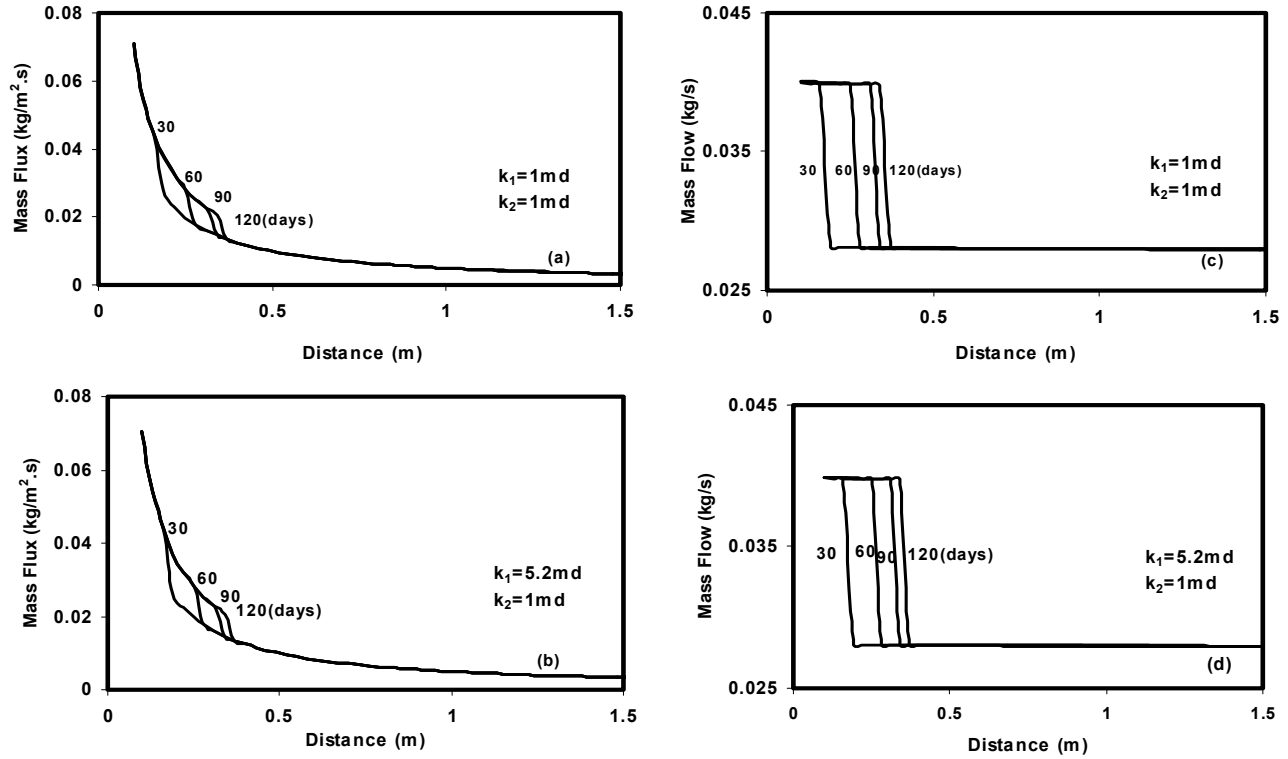


Figure 12. Mass flux and total mass flow profiles for a reservoir temperature of 287K and a well natural gas output of 0.04kg/s for different permeabilities.

Figure 13 shows the movement of the dissociation front for different natural gas outputs. Here the reservoir conditions are assumed to be fixed at 15 MPa and 287 K. The permeabilities in gas and hydrate zones are, respectively, 5.2 md and 0.4 md. Figure 13 shows that the distance of the front from the well increases proportional to the square root of time. As the natural gas output increases, the outward motion of the front speeds up.

For a fixed reservoir pressure and a natural gas output of 0.03 kg/s, time evolutions of dissociation front for different reservoir temperatures are shown in Figure 14. It is observed that at higher reservoir temperature the dissociation front moves away from the well at faster speed. At a fixed flow rate, a higher reservoir temperature leads to higher level of hydrate dissociation that causes a more rapid motion of the front.

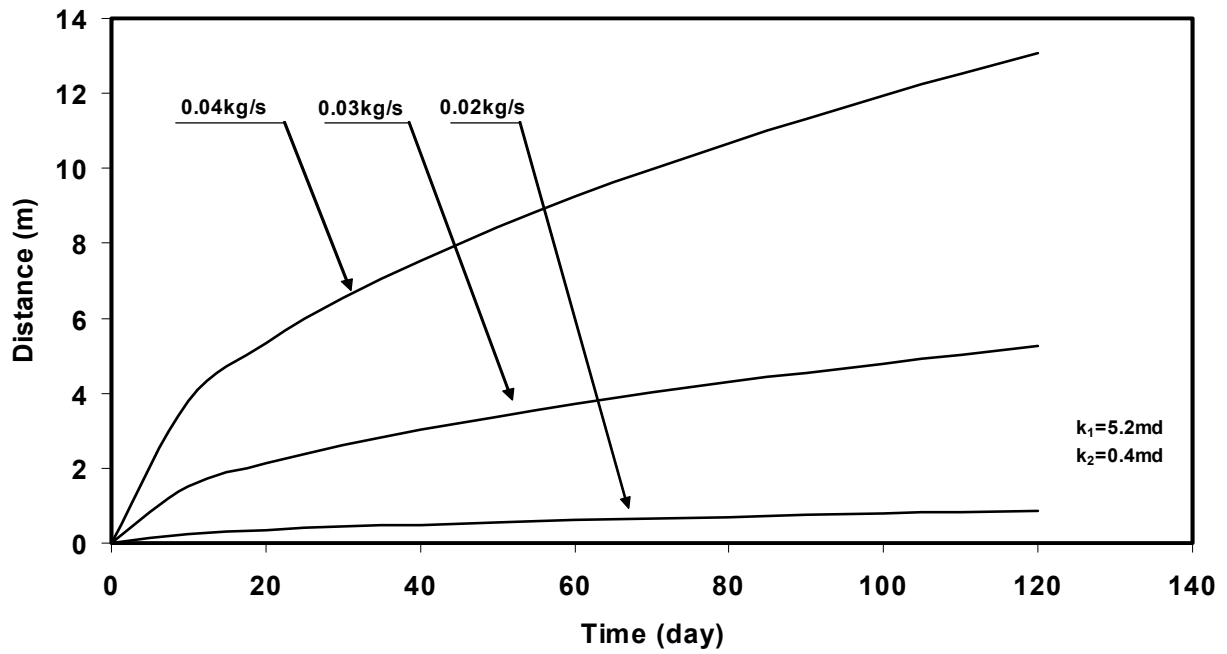


Figure 13. Time variations of the position of the dissociation front for different natural gas outputs.

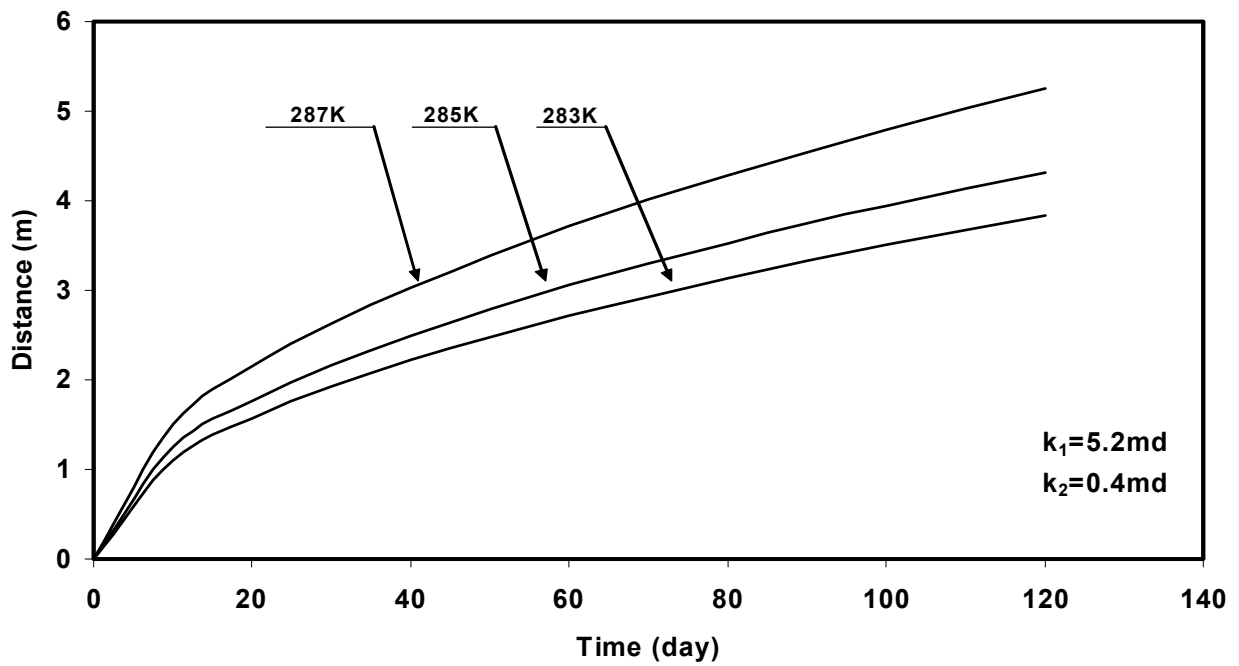


Figure 14. Time variations of the position of the dissociation front for different reservoir temperature for a well natural gas output of 0.03 kg/s.

Figure 15 shows the time evolution of dissociation front for different hydrate zone permeabilities for a natural gas output of 0.04kg/s. Here, the reservoir pressure and temperature are, respectively, 15MPa and 287K. This figure shows that the dissociation front moves faster as the hydrate zone permeability decreases. As noted before, this is because at smaller hydrate zone permeability, the natural gas flow toward the front decreases. To maintain a fixed flow rate, a large amount of hydrate has to dissociate to compensate, and therefore, the dissociation front moves faster.

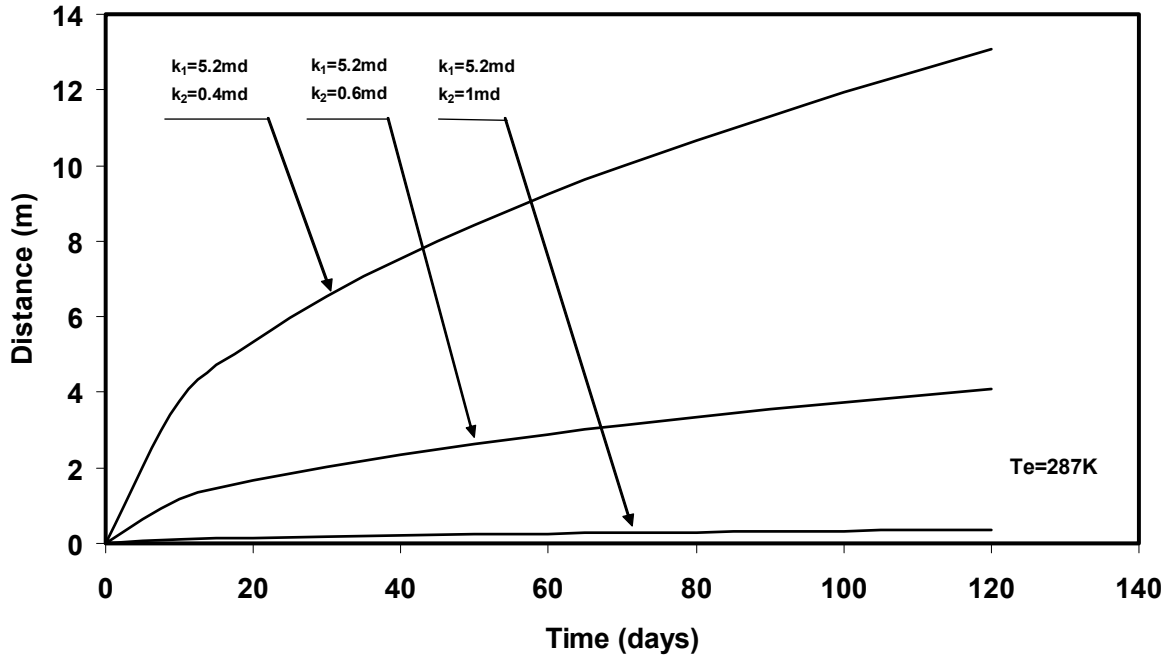


Figure 15. Time variations of the position of the dissociation front for a well natural gas output of 0.04 kg/s and for different permeabilities.

Conclusions of the Dissociation Model

Dissociation of methane hydrate in confined, pressurized reservoirs for fixed well outputs is studied. Evolutions of pressure, temperature, mass flux and mass flow rate profiles in axisymmetric reservoirs under various conditions are analyzed. The effects of variation in well output, reservoir temperature and reservoir zone permeabilities are studied. On the basis of the results presented, the following conclusions may be drawn:

- i. Under favorable conditions natural gas can be produced at a fixed rate from hydrate reservoirs by a depressurization well.

- ii. For a large homogenous hydrate reservoir containing free natural gas, the dissociation pressure and temperature are fixed, and depend only on the reservoir conditions and the well output.
- iii. For fixed reservoir pressure and temperature, and a constant well production rate, the well pressure decreases with time. Thus, to maintain a constant natural gas output, the well pressure needs to be continuously reduced.
- iv. At low well output, the decrease in the well pressure is very slight. At high well outputs, the well pressure decreases rather quickly and constant output can only be maintained for a short period of the time.
- v. The reservoir permeability in the hydrate zone significantly affects the natural gas production process.
- vi. For a fixed natural gas output, the pressure and temperature profiles have a smooth variation in the hydrate zone, but have sharper slope in the gas zone.
- vii. The gas mass flow rates in the hydrate and in the gas zone are roughly constant, with a sharp jump at the dissociation front.

As noted before, the presented linearization approach neglects the heat conduction in the reservoir and cannot enforce the balance of energy at the dissociation front. When this limitation is removed, the similarity solutions do not hold and the original nonlinear governing equations must be solved numerically. Such a study is also performed and the results are being compiled into a manuscript for publication in archival journals.

Thermodynamically Consistent Model for Multiphase Flows in Porous Media

A thermodynamically consistent continuum model for multiphase fluid mixture (including gas-liquid such as natural gas-water) flows through poro-elastic media is developed. The basic conservation laws developed via a volume averaging technique are considered. Effects of phasic equilibrated forces are included in the model. Based on the thermodynamics of the multiphase mixture flows, appropriate constitutive equations are formulated. The entropy inequality is exploited, and the method of Lagrangian multiplier is used along with the phasic conservation laws to derive the constitutive equations for the phasic stress tensors, equilibrated stress vectors and the interactions terms. The special cases of wave propagation in poro-elastic media saturated with multiphase fluids, and multiphase flows through porous media are studied. It is shown that the present theory leads to the extended Darcy's law and contains, as its special case, Biot's theory of saturated poro-elastic media.

Balance Laws

Consider a dispersed mixture of m distinct fluid phases in a deformable porous media. In the absence of chemical reaction and interfacial mass transfer, starting from the global conservation laws for each phase and using an spatial averaging method, the local forms of the laws for different constituents were developed by Whitaker (1986), Ahmadi (1987), Hassanizadeh and Gray (1993), and Kaviani (1995), among others. Accordingly, the differential forms of the equations of conservation of mass for each of phases becomes,

$$\frac{\partial \rho^s}{\partial t} + \frac{\partial}{\partial x_j} (\rho^s \tilde{v}_j^s) = 0 \quad (1)$$

$$\frac{\partial \rho^f}{\partial t} + \frac{\partial}{\partial x_j} (\rho^f \tilde{v}_j^f) = 0 \quad (2)$$

Here ρ is the mass density, and \tilde{v}_i is the volume averaged mean velocity vector. The superscripts f refers to the f^{th} fluid phase and superscript s identifies the solid (porous) media. When the particulate and fluid phases are incompressible, it follows that

$$\rho^s = \rho_0^s v^s, \quad \rho^f = \rho_0^f v^f \quad (3)$$

where v is the mean volume fraction, and ρ_0 is the density of the material of a constituent.

Note that throughout this paper the concept of interpenetrating continua are used and it is assumed that the equivalent phasic continua simultaneously occupy the same volume

elements. If the density of the material of a constituent, ρ_0 , is constant, Equations (1) and (2) can be restated as

$$\frac{\partial v^s}{\partial t} + \frac{\partial}{\partial x_j} (v^s \tilde{v}^s_j) = 0 \quad (4)$$

$$\frac{\partial v^f}{\partial t} + \frac{\partial}{\partial x_j} (v^f \tilde{v}^f_j) = 0 \quad (5)$$

The following constraint for fully saturated mixtures is imposed,

$$\sum_{f=1}^m v^f + v^s = 1 \quad (6)$$

Based on the Equation (2), the conservation of mass for the fluid mixture flow may be restated as

$$\frac{\partial \rho}{\partial t} + \frac{\partial}{\partial x_j} (\rho \tilde{v}_j) = 0 \quad (7)$$

where the density of the fluid mixture is

$$\rho = \sum_{f=1}^m \rho^f \quad (8)$$

The velocity of the mixture is also defined as

$$\rho \tilde{v}_j = \sum_{f=1}^m \rho^f \tilde{v}_j^f \quad (9)$$

The local forms of balance of linear momentum for each phase are given as,

$$\rho^s \frac{d\tilde{v}_i^s}{dt} = \rho^s f_i^s + \frac{\partial t_{ji}^s}{\partial x_j} + \bar{P}_i^s \quad (10)$$

$$\rho^f \frac{d\tilde{v}_i^f}{dt} = \rho^f f_i^f + \frac{\partial t_{ji}^f}{\partial x_j} + \bar{P}_i^f \quad (11)$$

where f_i is the body force per unit mass, t_{ij} is the average stress tensor, and \bar{P}_i is the

interaction momentum supply. The net interaction momentum supply for multiphase mixtures must be zero, i.e.;

$$\sum_{f=1}^m \bar{P}_i^f + \bar{P}_i^s = 0 \quad (12)$$

Equations governing the balance of equilibrated force are given by

$$\rho^s k^s \left\{ \frac{d\dot{v}^s}{dt} + (\dot{v}^s)^2 \right\} = \frac{\partial h_i^s}{\partial x_i} + \rho^s \ell^s + g^s \quad (13)$$

$$\rho^f k^f \left\{ \frac{d\dot{v}^f}{dt} + (\dot{v}^f)^2 \right\} = \frac{\partial h_i^f}{\partial x_i} + \rho^f \ell^f + g^f \quad (14)$$

where k is the equilibrated inertia, h_i is the equilibrated stress vector, ℓ is the equilibrated force per unit mass and g is the interaction equilibrated force supply (internal equilibrated force). Note that $\sum_{f=1}^m g^f + g^s \neq 0$, since g includes the inherent internal equilibrated force of each constituent.

The equation of conservation of equilibrated inertia are given as,

$$\frac{dk^s}{dt} - 2\dot{v}^s k^s = 0 \quad (15)$$

$$\frac{dk^f}{dt} - 2\dot{v}^f k^f = 0 \quad (16)$$

Equations governing the balance of equilibrated force and conservation of equilibrated inertia are the traces of the general stress-moment and micro-inertia equations developed by Twiss and Eringen (1971) and Ahmadi (1987).

The equation of conservation of energy for porous media and the fluid phase are given as

$$\rho^s \frac{de^s}{dt} = q_{j,j}^s + t_{ji}^s \tilde{v}_{j,i}^s + h_j^s \dot{v}_{j,j}^s - g^s \dot{v}^s - \bar{P}_j^s \tilde{v}_j^s + r^s + e^{s+} \quad (17)$$

$$\rho^f \frac{de^f}{dt} = q_{j,j}^f + t_{ji}^f \tilde{v}_{j,i}^f + h_j^f \dot{v}_{j,j}^f - g^f \dot{v}^f - \bar{P}_j^f \tilde{v}_j^f + r^f + e^{f+} \quad (18)$$

where e is mean internal energy per unit mass, q_j is the mean heat flux vector pointing outward of an enclosed volume, r is the internal heat source per unit volume and e^+ is the interaction energy supply. Note that,

$$\sum_{f=1}^m e^{f+} + e^{s+} = 0 \quad (19)$$

The entropy inequality for the mixture is given as,

$$\sum_{f=1}^m \left[\rho^f \dot{\eta}^f - (q_j^f / \theta^f)_{,j} - \frac{r^f}{\theta^f} \right] + \rho^s \dot{\eta}^s - (q_j^s / \theta^s)_{,j} - \frac{r^s}{\theta^s} \geq 0 \quad (20)$$

Here η is the mean entropy per unit mass and θ is the mean temperature.

Throughout this work the regular Cartesian tensor notation with Latin subscripts is used. Indices after a comma denote partial derivatives and d/dt stands for the substantial (total) time derivative.

The Helmholtz free energy function for the fluid phases and porous body are defined as,

$$\psi^s = e^s - \eta^s \theta^s \quad (21)$$

$$\psi^f = e^f - \eta^f \theta^f \quad (22)$$

By eliminating the internal heat source, r , between Equations (17), (18), and (20) and using Equations (21) and (22) the Clausius-Duhem inequality may be restated as,

$$\begin{aligned} & \sum_{f=1}^m \frac{1}{\theta^f} [-\rho^f (\dot{\psi}^f + \eta^f \dot{\theta}^f) + t_{ji}^f \tilde{v}_{j,i}^f + \frac{1}{\theta^f} q_j^f \theta_{,j}^f + h_j^f \dot{v}_{,j}^f - g^f \dot{v}^f - \tilde{v}_j^f \bar{P}_j^f + e^{f+}] \\ & + \frac{1}{\theta^s} [-\rho^s (\dot{\psi}^s + \eta^s \dot{\theta}^s) + t_{ji}^s \tilde{v}_{j,i}^s + \frac{1}{\theta^s} q_j^s \theta_{,j}^s + h_j^s \dot{v}_{,j}^s - g^s \dot{v}^s - \tilde{v}_j^s \bar{P}_j^s + e^{s+}] \geq 0 \end{aligned} \quad (23)$$

Taking the time derivative of the Equation (6), we find

$$\dot{v}^s - \tilde{v}_j^s v_{,j}^s + \sum_{f=1}^m [\dot{v}^f - \tilde{v}_j^f v_{,j}^f] = 0 \quad (24)$$

The method of Lagrangian multipliers developed by Truesdell and Noll (1965) is used here to include the effect of constraints on the constitutive equations. Accordingly, multiplying Equations (24), (4) and (5), respectively, by Lagrangian multiplier functions, $\Lambda(x, t)$, $\frac{\Lambda^f(x, t)}{\theta^f}$, and $\frac{\Lambda^s(x, t)}{\theta^s}$, and adding the result to the entropy inequality given by Equation (23), it follows that

$$\begin{aligned} \sum_{f=1}^m \frac{1}{\theta^f} [& -\rho^f (\dot{\psi}^f + \eta^f \dot{\theta}^f) + t_{ji}^f \tilde{v}_{j,i}^f + \frac{1}{\theta^f} q_j^f \theta_{,j}^f + h_j^f \dot{v}_{,j}^f + \Lambda^f v^f \tilde{v}_{j,j}^f \\ & - (g^f - \Lambda \theta^f - \Lambda^f) \dot{v}^f - (\bar{P}_j^f + \Lambda \theta^f v_{,j}^f) \tilde{v}_j^f + e^{f+}] \\ & + \frac{1}{\theta^s} [-\bar{\rho}^s (\dot{\psi}^s + \eta^s \dot{\theta}^s) + t_{ji}^s \tilde{v}_{j,i}^s + \frac{1}{\theta^s} q_j^s \theta_{,j}^s + h_j^s \dot{v}_{,j}^s + \Lambda^s v^s \tilde{v}_{j,j}^s \\ & - (g^s - \Lambda \theta^s - \Lambda^s) \dot{v}^s - (\bar{P}_j^s + \Lambda \theta^s v_{,j}^s) \tilde{v}_j^s + e^{s+}] \geq 0 \end{aligned} \quad (25)$$

For the fully saturated multiphase fluid flows (with incompressible constituents) through poro-elastic media, inequality (25) is the appropriate expression of the second law of thermodynamics.

Constitutive Equations

In this section, based on the averaged entropy inequality given by Equation (25), formulation of constitutive equations for multiphase flows in poro-elastic media is described. The following set of constitutive independent variables are postulated

$$\{\mathbf{S}^s\} = \{\mathbf{k}^s, \mathbf{v}^s, \mathbf{v}_{,i}^s, \dot{\mathbf{v}}^s, \dot{\mathbf{v}}_{,i}^s, \theta^s, \theta_{,i}^s, \mathbf{d}_{ij}^s, \mathbf{e}_{ii}^s\} \quad (26)$$

$$\{\mathbf{S}^f\} = \{\mathbf{k}^f, \mathbf{v}^f, \mathbf{v}_{,i}^f, \dot{\mathbf{v}}^f, \dot{\mathbf{v}}_{,i}^f, \theta^f, \theta_{,i}^f, \mathbf{d}_{ij}^f, \mathbf{e}_{ii}^f, \mathbf{e}_{ii}^s\} \quad (27)$$

$$\{\mathbf{S}^{fs}\} = \tilde{\mathbf{v}}_i^{fs} \quad (28)$$

where \mathbf{d}_{ij} is the deformation rate tensor defined as

$$\mathbf{d}_{ij}^s = \frac{1}{2} (\tilde{v}_{i,j}^s + \tilde{v}_{j,i}^s), \quad \mathbf{d}_{ij}^f = \frac{1}{2} (\tilde{v}_{i,j}^f + \tilde{v}_{j,i}^f) \quad (29)$$

and, \mathbf{e}_{ij}^s and \mathbf{e}_{ij}^f are the solid and fluid strain tensors given by

$$\mathbf{e}_{ij}^s = \frac{1}{2}(\tilde{\mathbf{u}}_{i,j}^s + \tilde{\mathbf{u}}_{j,i}^s) \quad (30)$$

$$\mathbf{e}_{ij}^f = \frac{1}{2}(\tilde{\mathbf{u}}_{i,j}^f + \tilde{\mathbf{u}}_{j,i}^f) \quad (31)$$

Here $\tilde{\mathbf{u}}_i^s$ and $\tilde{\mathbf{u}}_i^f$ are the displacement vector of the porous matrix and f^{th} fluid constituents. In Equation (28) the relative velocity of the f^{th} fluid phase with respect to the porous medium, $\tilde{\mathbf{v}}_i^{\text{fs}}$, is defined as

$$\tilde{\mathbf{v}}_i^{\text{fs}} = \tilde{\mathbf{v}}_i^f - \tilde{\mathbf{v}}_i^s \quad (32)$$

It should be noted here that the mass densities are not included in the set of constitutive independent variables given by Equations (26), (27), and (28). This is because, for mixtures with incompressible constituents, the phasic mass densities are given in terms of phasic volume fractions in accordance to equation (3). The dilatational strains of the fluid and solid constituents, however, are included in Equations (26) and (27).

We now propose the following set of frame-indifferent constitutive equations:

$$\begin{aligned} \psi^s &= \psi^s(\mathbf{k}^s, \mathbf{v}^s, \mathbf{v}_{,i}^s, \dot{\mathbf{v}}^s, \dot{\mathbf{v}}_{,i}^s, \theta^s, \theta_{,i}^s, \mathbf{d}_{ij}^s, \mathbf{e}_{ij}^s, \mathbf{e}_{ii}^s) & \psi^f &= \psi^f(\mathbf{k}^f, \mathbf{v}^f, \mathbf{v}_{,i}^f, \dot{\mathbf{v}}^f, \dot{\mathbf{v}}_{,i}^f, \theta^f, \theta_{,i}^f, \mathbf{d}_{ij}^f, \mathbf{e}_{ij}^f, \mathbf{e}_{ii}^s) \\ \mathbf{t}_{ij}^s &= \mathbf{t}_{ij}^s(\mathbf{k}^s, \mathbf{v}^s, \mathbf{v}_{,i}^s, \dot{\mathbf{v}}^s, \dot{\mathbf{v}}_{,i}^s, \theta^s, \theta_{,i}^s, \mathbf{d}_{ij}^s, \mathbf{e}_{ij}^s, \mathbf{e}_{ii}^s) & \mathbf{t}_{ij}^f &= \mathbf{t}_{ij}^f(\mathbf{k}^f, \mathbf{v}^f, \mathbf{v}_{,i}^f, \dot{\mathbf{v}}^f, \dot{\mathbf{v}}_{,i}^f, \theta^f, \theta_{,i}^f, \mathbf{d}_{ij}^f, \mathbf{e}_{ij}^f, \mathbf{e}_{ii}^s) \\ \mathbf{h}_i^s &= \mathbf{h}_i^s(\mathbf{k}^s, \mathbf{v}^s, \mathbf{v}_{,i}^s, \dot{\mathbf{v}}^s, \dot{\mathbf{v}}_{,i}^s, \theta^s, \theta_{,i}^s, \mathbf{d}_{ij}^s, \mathbf{e}_{ij}^s, \mathbf{e}_{ii}^s) & \mathbf{h}_i^f &= \mathbf{h}_i^f(\mathbf{k}^f, \mathbf{v}^f, \mathbf{v}_{,i}^f, \dot{\mathbf{v}}^f, \dot{\mathbf{v}}_{,i}^f, \theta^f, \theta_{,i}^f, \mathbf{d}_{ij}^f, \mathbf{e}_{ij}^f, \mathbf{e}_{ii}^s) \\ \mathbf{q}^s &= \mathbf{q}^s(\mathbf{k}^s, \mathbf{v}^s, \mathbf{v}_{,i}^s, \dot{\mathbf{v}}^s, \dot{\mathbf{v}}_{,i}^s, \theta^s, \theta_{,i}^s, \mathbf{d}_{ij}^s, \mathbf{e}_{ij}^s, \mathbf{e}_{ii}^s), & \mathbf{q}^f &= \mathbf{q}^f(\mathbf{k}^f, \mathbf{v}^f, \mathbf{v}_{,i}^f, \dot{\mathbf{v}}^f, \dot{\mathbf{v}}_{,i}^f, \theta^f, \theta_{,i}^f, \mathbf{d}_{ij}^f, \mathbf{e}_{ij}^f, \mathbf{e}_{ii}^s) \\ \eta^s &= \eta^s(\mathbf{k}^s, \mathbf{v}^s, \mathbf{v}_{,i}^s, \dot{\mathbf{v}}^s, \dot{\mathbf{v}}_{,i}^s, \theta^s, \theta_{,i}^s, \mathbf{d}_{ij}^s, \mathbf{e}_{ij}^s, \mathbf{e}_{ii}^s) \\ \eta^f &= \eta^f(\mathbf{k}^f, \mathbf{v}^f, \mathbf{v}_{,i}^f, \dot{\mathbf{v}}^f, \dot{\mathbf{v}}_{,i}^f, \theta^f, \theta_{,i}^f, \mathbf{d}_{ij}^f, \mathbf{e}_{ij}^f, \mathbf{e}_{ii}^s) \\ \mathbf{P}_j^s &= \mathbf{P}_j^s(\mathbf{k}^s, \mathbf{v}^s, \mathbf{v}_{,i}^s, \dot{\mathbf{v}}^s, \dot{\mathbf{v}}_{,i}^s, \theta^s, \theta_{,i}^s, \mathbf{d}_{ij}^s, \tilde{\mathbf{v}}_i^{\text{fs}}, \mathbf{e}_{ij}^s, \mathbf{e}_{ii}^s) \\ \mathbf{P}_j^f &= \mathbf{P}_j^f(\mathbf{k}^f, \mathbf{v}^f, \mathbf{v}_{,i}^f, \dot{\mathbf{v}}^f, \dot{\mathbf{v}}_{,i}^f, \theta^f, \theta_{,i}^f, \mathbf{d}_{ij}^f, \tilde{\mathbf{v}}_i^{\text{fs}}, \mathbf{e}_{ij}^f, \mathbf{e}_{ii}^s) \\ \mathbf{g}^s &= \mathbf{g}^s(\mathbf{k}^s, \mathbf{v}^s, \mathbf{v}_{,i}^s, \dot{\mathbf{v}}^s, \dot{\mathbf{v}}_{,i}^s, \theta^s, \theta_{,i}^s, \mathbf{d}_{ij}^s, \tilde{\mathbf{v}}_i^{\text{fs}}, \mathbf{e}_{ij}^s, \mathbf{e}_{ii}^s) \\ \mathbf{g}^f &= \mathbf{g}^f(\mathbf{k}^f, \mathbf{v}^f, \mathbf{v}_{,i}^f, \dot{\mathbf{v}}^f, \dot{\mathbf{v}}_{,i}^f, \theta^f, \theta_{,i}^f, \mathbf{d}_{ij}^f, \tilde{\mathbf{v}}_i^{\text{fs}}, \mathbf{e}_{ij}^f, \mathbf{e}_{ii}^s) \\ \mathbf{e}^{s+} &= \mathbf{e}^{s+}(\mathbf{k}^s, \mathbf{v}^s, \mathbf{v}_{,i}^s, \dot{\mathbf{v}}^s, \dot{\mathbf{v}}_{,i}^s, \theta^s, \theta_{,i}^s, \mathbf{d}_{ij}^s, \tilde{\mathbf{v}}_i^{\text{fs}}, \mathbf{e}_{ij}^s, \mathbf{e}_{ii}^s) \\ \mathbf{e}^{f+} &= \mathbf{e}^{f+}(\mathbf{k}^f, \mathbf{v}^f, \mathbf{v}_{,i}^f, \dot{\mathbf{v}}^f, \dot{\mathbf{v}}_{,i}^f, \theta^f, \theta_{,i}^f, \mathbf{d}_{ij}^f, \tilde{\mathbf{v}}_i^{\text{fs}}, \mathbf{e}_{ij}^f, \mathbf{e}_{ii}^s) \end{aligned} \quad (33)$$

It should be noted here that, according to the principle of equipresence of continuum mechanics, in general, all the constitutive dependent variables must be functions of all the

independent constitutive variables. However, for simplicity of analysis, this principle was not fully utilized in constitutive equations given by (33). Furthermore, it is also assumed that, the porous medium free energy function is also a function of strain rate tensor.

Evaluating $\dot{\psi}^s$ and $\dot{\psi}^f$ from Equations (33), and substituting the results into the inequality (25), it follows that

$$\begin{aligned}
& \sum_{f=1}^m \frac{1}{\theta^f} [-\rho^f \left(\frac{\partial \psi^f}{\partial \theta^f} + \eta^f \right) \dot{\theta}^f - \rho^f \left(\frac{\partial \psi^f}{\partial \dot{v}^f} \dot{v}^f + \frac{\partial \psi^f}{\partial \dot{v}_{,j}^f} \dot{v}_{,j}^f + \frac{\partial \psi^f}{\partial \dot{\theta}_{,j}^f} \dot{\theta}_{,j}^f + \frac{\partial \psi^f}{\partial \dot{d}_{ij}^f} \dot{d}_{ij}^f \right) \\
& + (t_{ji}^f + (-\rho^f \frac{\partial \psi^f}{\partial e_{kk}^f} - \frac{v^f \theta^f}{(1-v^s) \theta^s} \frac{\partial \psi^s}{\partial e_{kk}^f} + \Lambda^f v^f) \delta_{ij} + \rho^f \frac{\partial \psi^f}{\partial v_{,j}^f} v_{,i}^f) d_{ij}^f \\
& + (\rho^f \frac{\partial \psi^f}{\partial v_{,j}^f} v_{,i}^f) \tilde{v}_{[i,j]}^f + (h_j^f - \rho^f \frac{\partial \psi^f}{\partial v_{,j}^f}) \dot{v}_{,j}^f - (-\pi^f + \rho^f \frac{\partial \psi^f}{\partial v^f} + g^f - \Lambda \theta^f - \Lambda^f) \dot{v}^f \\
& - (\bar{P}_j^f + \Lambda \theta^f v_{,j}^f) \tilde{v}_j^f + q_j^f (\ln \theta^f)_{,j} + e^{f+}] \\
& + \frac{1}{\theta^s} [-\rho^s \left(\frac{\partial \psi^s}{\partial \theta^s} + \eta^s \right) \dot{\theta}^s - \rho^s \left(\frac{\partial \psi^s}{\partial \dot{v}^s} \dot{v}^s + \frac{\partial \psi^s}{\partial \dot{v}_{,j}^s} \dot{v}_{,j}^s + \frac{\partial \psi^s}{\partial \dot{\theta}_{,j}^s} \dot{\theta}_{,j}^s + \frac{\partial \psi^s}{\partial \dot{d}_{ij}^s} \dot{d}_{ij}^s \right) \\
& + (t_{ji}^s + \Lambda^s v^s \delta_{ji} + \rho^s \frac{\partial \psi^s}{\partial v_{,j}^s} v_{,i}^s - \rho^s \frac{\partial \psi^s}{\partial e_{kk}^s} - \theta^s \sum_{f=1}^m \frac{\rho^f}{\theta^f} \frac{\partial \psi^f}{\partial e_{kk}^s} \delta_{ij}) d_{ij}^s + (\rho^s \frac{\partial \psi^s}{\partial v_{,j}^s} v_{,i}^s) \tilde{v}_{[i,j]}^s \\
& + (h_j^s - \rho^s \frac{\partial \psi^s}{\partial v_{,j}^s}) \dot{v}_{,j}^s - (-\pi^s + \rho^s \frac{\partial \psi^s}{\partial v^s} + g^s - \Lambda \theta^s - \Lambda^s) \dot{v}^s \\
& - (\bar{P}_j^s + \Lambda \theta^s v_{,j}^s) \tilde{v}_j^s + q_j^s (\ln \theta^s)_{,j} + e^{s+}] \geq 0
\end{aligned} \tag{34}$$

where, $\tilde{v}_{[i,j]}$ is the anti-symmetric part of the velocity gradient tensor. The micro pressures in the distributed solid and fluid bodies, π^s and π^f , are defined as

$$\pi^s = -2\rho^f \frac{\partial \psi^s}{\partial k^s} k^s \tag{35}$$

$$\pi^f = -2\rho^f \frac{\partial \psi^f}{\partial k^f} k^f \tag{36}$$

Demanding that the entropy inequality (34) holds for all independent variations of $\dot{\theta}^f, \dot{\theta}_{,i}^f, \dot{\theta}^s, \dot{\theta}_{,i}^s, \dot{v}^f, \dot{v}_{,i}^f, \dot{v}^s, \dot{v}_{,i}^s, \dot{d}_{ij}^f, \dot{d}_{ij}^s$ and $\tilde{v}_{[j,i]}^f, \tilde{v}_{[j,i]}^s$, it follows that

$$\eta^s = -\frac{\partial \psi^s}{\partial \theta^s}, \quad \eta^f = -\frac{\partial \psi^f}{\partial \theta^f} \quad (37)$$

$$\frac{\partial \psi^f}{\partial \dot{v}^f} = \frac{\partial \psi^f}{\partial \dot{v}_{,i}^f} = \frac{\partial \psi^s}{\partial \dot{v}^s} = \frac{\partial \psi^s}{\partial \dot{v}_{,i}^s} = 0 \quad (38)$$

$$\rho^f \varepsilon_{ikj} \frac{\partial \psi^f}{\partial v_{,k}^f} v_{,j}^f = \rho^s \varepsilon_{ikj} \frac{\partial \psi^s}{\partial v_{,k}^s} v_{,j}^s = 0 \quad (39)$$

$$\frac{\partial \psi^f}{\partial \theta_{,i}^f} = \frac{\partial \psi^f}{\partial d_{ij}^f} = \frac{\partial \psi^s}{\partial \theta_{,i}^s} = \frac{\partial \psi^s}{\partial d_{ij}^s} = 0 \quad (40)$$

Introducing the elastic and dissipative parts of the stress tensor and equilibrated stress vector as

$$t_{ij}^s = {}_E t_{ij}^s + {}_D t_{ij}^s, \quad t_{ij}^f = {}_E t_{ij}^f + {}_D t_{ij}^f \quad (41)$$

$$h_i^s = {}_E h_i^s + {}_D h_i^s, \quad h_i^f = {}_E h_i^f + {}_D h_i^f \quad (42)$$

where the elastic parts of the stresses as obtained from entropy inequality (34), are given by

$${}_E t_{ij}^s = -\Lambda^s v^s \delta_{ij} - \rho^s \frac{\partial \psi^s}{\partial v_{,i}^s} v_{,j}^s + \rho^s \frac{\partial \psi^s}{\partial e_{ij}^s} + \theta^s \sum_{f=1}^m \frac{\rho^f}{\theta^f} \frac{\partial \psi^f}{\partial e_{kk}^s} \delta_{ij} \quad (43)$$

$${}_E t_{ij}^f = (\rho^f \frac{\partial \psi^f}{\partial e_{mm}^f} + \frac{v^f \theta^f}{(1-v^s) \theta^s} \rho^s \frac{\partial \psi^s}{\partial e_{mm}^f} - \Lambda^f v^f) \delta_{ij} - \rho^f \frac{\partial \psi^f}{\partial v_{,i}^f} v_{,j}^f \quad (44)$$

$${}_E h_i^s = \rho^s \frac{\partial \psi^s}{\partial v_{,i}^s}, \quad {}_E h_i^f = \rho^f \frac{\partial \psi^f}{\partial v_{,i}^f} \quad (45)$$

Using Equations (37)-(40), and (43)-(45), inequality (34) reduces to

$$\begin{aligned} & \sum_{f=1}^m \frac{1}{\theta^f} [{}_D t_{ji}^f d_{ij}^f + {}_D h_j^f \dot{v}_{,j}^f - (-\pi^f + \rho^f \frac{\partial \psi^f}{\partial v^f} + g^f - \Lambda \theta^f - \Lambda^f) \dot{v}^f - (\bar{P}_j^f + \Lambda \theta^f v_{,j}^f) \tilde{v}_j^f \\ & \quad + q_j^f (\ln \theta^f)_{,j} + e^{f+}] \\ & + \frac{1}{\theta^s} [{}_D t_{ji}^s d_{ij}^s + {}_D h_j^s \dot{v}_{,j}^s - (-\pi^s + \rho^s \frac{\partial \psi^s}{\partial v^s} + g^s - \Lambda \theta^s - \Lambda^s) \dot{v}^s - (\bar{P}_j^s + \Lambda \theta^s v_{,j}^s) \tilde{v}_j^s \\ & \quad + q_j^s (\ln \theta^s)_{,j} + e^{s+}] \geq 0 \end{aligned} \quad (46)$$

For the dissipative parts of stresses of an isotropic mixture the following set of

constitutive equations is then proposed,

$${}_D t_{ij}^s = 0 \quad (47)$$

$${}_D t_{ij}^f = \lambda^f d_{mm}^f \delta_{ij} + 2\mu^f d_{ij}^f \quad (48)$$

$${}_D h_k^s = 0 \quad (49)$$

$${}_D h_k^f = H^f \dot{v}_{,k}^f \quad (50)$$

The entropy inequality (46) imposes the following restrictions on the viscosity coefficients

$$3\lambda^f + 2\mu^f \geq 0, \quad \mu^f \geq 0 \quad (51)$$

From inequality (46) the constitutive equations for the internal equilibrated forces are proposed as

$$g^s = \pi^s - \rho^s \frac{\partial \psi^s}{\partial v^s} + \Lambda \theta^s + \Lambda^s - G^s \dot{v}^s \quad (52)$$

$$g^f = \pi^f - \rho^f \frac{\partial \psi^f}{\partial v^f} + \Lambda \theta^f + \Lambda^f - G^f \dot{v}^f \quad (53)$$

where

$$G^s \geq 0, \quad G^f \geq 0 \quad (54)$$

Isothermal Mixture

We now assume an isothermal mixture for deriving the additional required constitutive equations. For an isothermal mixture, $\theta^f = \theta^s = \theta$, the interaction momentum supply terms of entropy inequality must satisfy the following inequality,

$$-(\bar{P}_j^s + \Lambda \theta v_{,j}^s) \tilde{v}_j^s + \sum_{f=1}^m -(\bar{P}_j^f + \Lambda \theta v_{,j}^f) \tilde{v}_j^f \geq 0 \quad (55)$$

Using the Equations (6) and (12), Equation (55) may be restated as:

$$\sum_{f=1}^m (\bar{P}_j^f + \Lambda \theta v_{,j}^f) (\tilde{v}_j^s - \tilde{v}_j^f) \geq 0 \quad (56)$$

The mean interaction momentum supply for the fluid phases satisfying Equation (56) are given as

$$\bar{P}_j^f = \sum_{f'=1}^m D^{ff'} (\tilde{v}_j^s - \tilde{v}_j^{f'}) + p v_{,j}^f \quad (57)$$

where the drag coefficient $D^{ff'}$ is a positive definite ($m \times m$) matrix, and $p = -\Lambda\theta$ is the hydrostatic pressure. The corresponding momentum supply for the porous matrix is given by

$$\bar{P}_j^s = \sum_{f=1}^m \sum_{f'=1}^m D^{ff'} (\tilde{v}_j^{f'} - \tilde{v}_j^s) + p v_{,j}^s \quad (58)$$

The Helmholtz free energy function for the porous matrix and the phasic fluid phases are assumed to be given as

$$\begin{aligned} \rho^s \psi^s = & \alpha^s v_{,j}^s v_{,j}^s \\ & + v^s \left[\frac{1}{2} a_0^s (v^s)^2 + \frac{1}{2} \lambda^s e_{kk}^s e_{mm}^s + \mu^s e_{ij}^s e_{ij}^s + b_0^s v^s e_{kk}^s + \sum_{f=1}^m c_0^{sf} v^s e_{kk}^f \right. \\ & \left. + \frac{1}{2} \sum_{f=1}^m d_0^{sf} e_{kk}^f e_{mm}^f + \sum_{f=1}^m e_0^{sf} e_{kk}^f e_{mm}^s \right] \end{aligned} \quad (59)$$

$$\begin{aligned} \rho^f \psi^f = & \alpha^f v_{,j}^f v_{,j}^f \\ & + v^f \left[\frac{1}{2} \alpha_0^f (v^f)^2 + b_0^f v^f e_{kk}^s + c_0^f v^f e_{kk}^f + \frac{1}{2} d_0^f e_{kk}^f e_{mm}^f + e_0^f e_{kk}^f e_{mm}^s + \frac{1}{2} f_0^f e_{kk}^s e_{mm}^s \right] \end{aligned} \quad (60)$$

where α^s and α^f are positive functions of corresponding volume fractions. For the strain free energy functions given by Equation (59) and (60) to be positive, the following restriction on the material properties are imposed

$$\begin{aligned} \mu^s & \geq 0, \quad \lambda^s \geq 0 \\ \alpha^s & \geq 0, \quad a_0^s \geq 0, \quad (b_0^s)^2 \leq a_0^s \lambda^s \\ d_0^{sf} & \geq 0, \quad e_0^{sf} \geq 0, \quad (c_0^{sf})^2 \leq d_0^{sf} e_0^{sf} \\ \alpha^f & \geq 0, \quad a_0^f \geq 0, \quad f_0^f \geq 0, \\ (b_0^f)^2 & \leq a_0^f f_0^f, \quad d_0^f \geq 0, \quad (e_0^f)^2 \leq d_0^f f_0^f \end{aligned} \quad (61)$$

Equations (35) and (36) for the free energy functions given (59) and (60), imply that the micro pressures vanish identically, i.e.,

$$\pi^s = \pi^f = 0 \quad (62)$$

The elastic part of the constitutive equations for poro-elastic matrix and the fluid phases given by (43)-(45) now become

$$\begin{aligned} {}_E t_{ij}^s = & -\Lambda^s v^s \delta_{ij} - 2\alpha^s v_{,i}^s v_{,j}^s + \lambda^s e_{kk}^s \delta_{ij} + 2\mu^s e_{ij}^s \\ & + v^s [b_0^s v^s + \sum_{f=1}^m b_0^f v^f + \sum_{f=1}^m (e_0^f + e_0^{sf}) e_{mm}^f + \sum_{f=1}^m f_0^f e_{mm}^s] \delta_{ij} \end{aligned} \quad (63)$$

$$\begin{aligned} {}_E t_{ij}^f = & -\Lambda^f v^f \delta_{ij} - 2\alpha^f v_{,i}^f v_{,j}^f \\ & + v^f [c_0^f v^f + \frac{v^f}{1-v^s} c_0^{sf} v^s + (d_0^f + \frac{v^f}{1-v^s} d_0^{sf}) e_{kk}^f \\ & + (e_0^f + \frac{v^f}{1-v^s} e_0^{sf}) e_{kk}^s] \delta_{ij} \end{aligned} \quad (64)$$

$${}_E h_i^s = 2\alpha^s v_{,j}^s \quad (65)$$

$${}_E h_i^f = 2\alpha^f v_{,j}^f \quad (66)$$

Similarly, the constitutive equations for the internal equilibrated forces given by (52) and (53) now become

$$g^s = -a_0^s (v^s)^2 - v^s v_{,j}^s v_{,j}^s \frac{d}{dv^s} \left(\frac{\alpha^s}{v^s} \right) - v^s (b_0^s e_{kk}^s + \sum_{f=1}^m c_0^{sf} e_{kk}^f) - p + \Lambda^s - G^s \dot{v}^s \quad (67)$$

$$g^f = -a_0^f (v^f)^2 - v^f v_{,j}^f v_{,j}^f \frac{d}{dv^f} \left(\frac{\alpha^f}{v^f} \right) - v^f (b_0^f e_{kk}^f + c_0^f e_{kk}^f) - p + \Lambda^f - G^f \dot{v}^f \quad (68)$$

The constitutive relationships for the multiphase flows given by the Equations (57), (58), (62)-(68) are consistent with the average Clausius-Duhem inequality.

Equations of Motion

Direct substitution of the constitutive equations into the equations of balance of linear momentum and balance of equilibrated force given by Equations (10), (11), (13) and (14)

yield the basic equation of motion of multiphase flow through poro-elastic media. These equations for porous media and fluid phase are:

Linear momentum of porous media and fluid phases

$$\begin{aligned}
\rho_0^s v^s \frac{d\tilde{v}_i^s}{dt} = & \rho^s f_i^s - (\Lambda^s v^s)_{,i} - 2(\alpha^s v_{,j}^s v_{,i}^s)_{,j} + [v^s \mu^s (\tilde{u}_{i,j}^s + \tilde{u}_{j,i}^s)]_{,j} \\
& + [v^s \lambda^s \tilde{u}_{k,k}^s + v^s [b_0^s v^s + \sum_{f=1}^m b_0^f v^f + \sum_{f=1}^m (e_0^f + e_0^{sf}) \tilde{u}_{m,m}^f + \sum_{f=1}^m f_0^f \tilde{u}_{m,m}^s]]_{,i} \\
& + \sum_{f=1}^m \sum_{f'=1}^m D^{ff'} (\tilde{v}_i^{f'} - \tilde{v}_i^s) + p v_{,i}^s
\end{aligned} \tag{69}$$

$$\begin{aligned}
\rho_0^f v^f \frac{d\tilde{v}_i^f}{dt} = & \rho^f f_i^f - (\Lambda^f v^f)_{,i} - 2(\alpha^f v_{,j}^f v_{,i}^f)_{,j} + [\mu^f (\tilde{v}_{j,i}^f + \tilde{v}_{i,j}^f)]_{,j} \\
& + \sum_{f'=1}^m D^{ff'} (\tilde{v}_i^{f'} - \tilde{v}_i^f) + p v_{,i}^f \\
& + [\lambda^f \tilde{v}_{j,j}^f + v^f [c_0^f v^f + \frac{v^f}{1-v^s} c_0^{sf} v^s + (d_0^f + \frac{v^f}{1-v^s} d_0^{sf}) \tilde{u}_{k,k}^f \\
& + (e_0^f + \frac{v^f}{1-v^s} e_0^{sf}) \tilde{u}_{k,k}^s]]_{,i}
\end{aligned} \tag{70}$$

Equilibrated force of porous media and fluid phase

$$\begin{aligned}
\rho_0^s v^s k^s (\frac{d\dot{v}^s}{dt} + (\dot{v}^s)^2) = & 2(\alpha^s v_{,j}^s)_{,j} - a_0^s (v^s)^2 - v^s \frac{d}{dv^s} (\frac{\alpha^s}{v^s}) v_{,j}^s v_{,j}^s \\
& - v^s (b_0^s e_{kk}^s + \sum_{f=1}^m c_0^{sf} e_{kk}^f) - p + \Lambda^s - G^s \dot{v}^s + \rho^s \ell^s
\end{aligned} \tag{71}$$

$$\begin{aligned}
\rho_0^f v^f k^f (\frac{d\dot{v}^f}{dt} + (\dot{v}^f)^2) = & 2(\alpha^f v_{,j}^f)_{,j} + (H^f \dot{v}_{,j}^f)_{,j} - a_0^f (v^f)^2 - v^f \frac{d}{dv^f} (\frac{\alpha^f}{v^f}) v_{,j}^f v_{,j}^f \\
& - v^f (b_0^f e_{kk}^f + c_0^f e_{kk}^f) - p + \Lambda^f - G^f \dot{v}^f + \rho^f \ell^f
\end{aligned} \tag{72}$$

Equations (69)-(72) together with equations of conservation of mass for porous media and fluid phase given by Equations (4), (5), the saturation condition (6), and the equilibrated

inertia given by Equations (15) and (16) form a complete set of $8(m+1)+1$ equations for determining $8(m+1)+1$ unknowns, $\tilde{v}_i^s, \tilde{v}_i^f, v^s, v^f, \dot{v}^s, \dot{v}^f, k^s, k^f, \Lambda^s, \Lambda^f$ and p .

Simplified Equations of Motions

In the absence of equilibrated inertia and equilibrated body force and when the dissipative parts of the equilibrated force are also negligible, i.e.

$$k^s = 0, k^f = 0, \ell^f = 0, \ell^s = 0, H^f = 0 \quad (73)$$

Equations (71) and (72) can be solved for the Lagrangian multiplier Λ^s and Λ^f ,

$$\Lambda^s = -2\alpha^s v_{,ij}^s - \left(\frac{d\alpha^s}{dv^s} + \frac{\alpha^s}{v^s} \right) v_{,j}^s v_{,j}^s + a_0^s (v^s)^2 + v^s (b_0^s e_{kk}^s + \sum_{f=1}^m c_0^{sf} e_{kk}^f) + p + G^s \dot{v}^s \quad (74)$$

$$\Lambda^f = -2\alpha^f v_{,ij}^f - \left(\frac{d\alpha^f}{dv^f} + \frac{\alpha^f}{v^f} \right) v_{,j}^f v_{,j}^f + a_0^f (v^f)^2 + v^f (b_0^f e_{kk}^s + c_0^f e_{kk}^f) + p + G^f \dot{v}^f \quad (75)$$

Employing Equations (74) and (75), Equations (69) and (70) may be restated as

$$\begin{aligned} \rho_0^s v^s \frac{d\tilde{v}_i^s}{dt} = & \rho_0^s v^s f_i^s + 2\alpha^s v^s v_{,jji}^s + 2v^s \frac{d\alpha^s}{dv^s} (v_{,i}^s v_{,jj}^s + v_{,ji}^s v_{,j}^s) \\ & + v^s \frac{d^2\alpha^s}{d(v^s)^2} v_{,j}^s v_{,j}^s v_{,i}^s - 3a_0^s (v^s)^2 v_{,i}^s - 2v^s v_{,i}^s (b_0^s e_{kk}^s + \sum_{f=1}^m c_0^{sf} e_{kk}^f) \\ & + [v^s \mu^s (\tilde{u}_{i,j}^s + \tilde{u}_{j,i}^s)]_{,j} + \sum_{f=1}^m \sum_{f'=1}^m D^{ff'} (\tilde{v}_i^{f'} - \tilde{v}_i^s) - v^s p_{,i} - (G^s v^s \dot{v}^s)_{,i} \\ & + \{v^s \lambda^s \tilde{u}_{k,k}^s + v^s [b_0^s v^s + \sum_{f=1}^m b_0^f v^f + \sum_{f=1}^m (e_0^f + e_0^{sf}) \tilde{u}_{m,m}^f + \sum_{f=1}^m f_0^f \tilde{u}_{m,m}^s]\}_{,i} \end{aligned} \quad (76)$$

$$\begin{aligned}
\rho_0^f v^f \frac{d\tilde{v}_i^f}{dt} = & \rho_0^f v^f f_i^f + 2v^f v_{,jji}^f + 2v^f \frac{d\alpha^f}{dv^f} (v_{,i}^f v_{,jj}^f + v_{,ji}^f v_{,j}^f) \\
& + v^f \frac{d^2 \alpha^f}{d(v^f)^2} v_{,j}^f v_{,j}^f v_{,i}^f - 3a_0^f (v^f)^2 v_{,i}^f - 2v^f v_{,i}^f (b_0^f e_{kk}^s + c_0^f e_{kk}^f) \\
& + [\mu^f (\tilde{v}_{j,i}^f + \tilde{v}_{i,j}^f)]_{,j} + \sum_{f'=1}^m D^{\tilde{f}f'} (\tilde{v}_i^s - \tilde{v}_i^{f'}) - v^f p_{,i} - (G^f v^f \dot{\mathbf{v}}^f)_{,i} \\
& + \{ \lambda^f \tilde{v}_{j,j}^f + v^f [c_0^f v^f + \frac{v^f}{1-v^s} c_0^{sf} v^s + (d_0^f + \frac{v^f}{1-v^s} d_0^{sf}) \tilde{u}_{k,k}^f \\
& \quad + (e_0^f + \frac{v^f}{1-v^s} e_0^{sf}) \tilde{u}_{k,k}^s] \}_{,i}
\end{aligned} \tag{77}$$

Here, Equations (76) and (77) together with Equations (4), (5) and (6) now form a set of $6(m+1)+1$ for determining $6(m+1)+1$ unknowns, $\tilde{v}_i^s, \tilde{v}_i^f, v^s, v^f, \dot{v}^s, \dot{v}^f$ and p .

When the material coefficients $\alpha^s, \alpha^f, \lambda^s, \lambda^f, G^s, G^f, \mu^s$ and μ^f are constants, Equations (76) and (77) may be restated as

$$\begin{aligned}
\rho_0^s v^s \frac{d\tilde{v}_i^s}{dt} = & \rho_0^s v^s f_i^s + 2\alpha^s v^s v_{,jji}^s - 3a_0^s (v^s)^2 v_{,i}^s - 2v^s v_{,i}^s (b_0^s \tilde{u}_{k,k}^s + \sum_{f=1}^m c_0^{sf} \tilde{u}_{k,k}^f) \\
& + \mu^s [v^s (\tilde{u}_{i,j}^s + \tilde{u}_{j,i}^s)]_{,j} + \sum_{f=1}^m \sum_{f'=1}^m D^{\tilde{f}f'} (\tilde{v}_i^{f'} - \tilde{v}_i^s) - v^s p_{,i} - G^s (v^s \dot{\mathbf{v}}^s)_{,i} \\
& + \lambda^s [v^s \tilde{u}_{k,k}^s]_{,i} + \{ v^s [b_0^s v^s + \sum_{f=1}^m b_0^f v^f + \sum_{f=1}^m (e_0^f + e_0^{sf}) \tilde{u}_{m,m}^f + \sum_{f=1}^m f_0^f \tilde{u}_{m,m}^s] \}_{,i}
\end{aligned} \tag{80}$$

$$\begin{aligned}
\rho_0^f v^f \frac{d\tilde{v}_i^f}{dt} = & \rho_0^f v^f f_i^f + 2\alpha^f v^f v_{,jji}^f - 3a_0^f (v^f)^2 v_{,i}^f - 2v^f v_{,i}^f (b_0^f \tilde{u}_{k,k}^s + c_0^f \tilde{u}_{k,k}^f) \\
& + \mu^f [(\tilde{v}_{j,i}^f + \tilde{v}_{i,j}^f)]_{,j} + \sum_{f'=1}^m D^{\tilde{f}f'} (\tilde{v}_i^s - \tilde{v}_i^{f'}) - v^f p_{,i} - G^f (v^f \dot{\mathbf{v}}^f)_{,i} + \lambda^f \tilde{v}_{j,ji}^f \\
& + \{ v^f [c_0^f v^f + \frac{v^f}{1-v^s} c_0^{sf} v^s + (d_0^f + \frac{v^f}{1-v^s} d_0^{sf}) \tilde{u}_{k,k}^f + (e_0^f + \frac{v^f}{1-v^s} e_0^{sf}) \tilde{u}_{k,k}^s] \}_{,i}
\end{aligned} \tag{81}$$

Equations (80) and (81) are the simplified form of the general equations of motion of multiphase flows in poroelastic media.

Special Cases

In this section special limiting cases of the general form of the governing equations are examined.

Saturated Poroelastic Media

Consider a poroelastic media whose pores are saturated with multiphase fluids. For nearly constant solid and fluid volume fractions (nearly constant porosity), the linearized form of Equations (80) and (81) may be restated as

$$\begin{aligned}
 \rho^s \ddot{\mathbf{u}}^s &= \rho^s \mathbf{f}^s + \alpha_1^s \nabla \nabla^2 \mathbf{v}^s - [a_1^s - 2b_0^s v^s - \sum_{f=1}^m b_0^f v^f + 2v^s (b_0^s \nabla \cdot \tilde{\mathbf{u}}^s + \sum_{f=1}^m c_0^{sf} \nabla \cdot \tilde{\mathbf{u}}^f) + G^s \dot{v}^s] \nabla \mathbf{v}^s \\
 &+ \sum_{f=1}^m b_0^f v^s \nabla \mathbf{v}^f + v^s (\mu^s + \lambda^s + \sum_{f=1}^m f_0^f) \nabla \nabla \cdot \tilde{\mathbf{u}}^s + v^s \mu^s \nabla^2 \tilde{\mathbf{u}}^s + v^s \sum_{f=1}^m (e_0^f + e_0^{sf}) \nabla \nabla \cdot \tilde{\mathbf{u}}^f \\
 &+ D(\dot{\tilde{\mathbf{u}}}^f - \dot{\tilde{\mathbf{u}}}^s) - v^s \nabla p - G^s v^s \nabla \dot{v}^s
 \end{aligned} \tag{82}$$

$$\begin{aligned}
 \rho^f \ddot{\mathbf{u}}^f &= \rho^f \mathbf{f}^f + \alpha_1^f \nabla \nabla^2 \mathbf{v}^f - [a_1^f - 2c_0^f v^f - 2 \frac{v^f}{1-v^s} c_0^{sf} v^s + G^f \dot{v}^f] \nabla \mathbf{v}^f \\
 &+ (\frac{v^f}{1-v^s})^2 c_0^{sf} \nabla \mathbf{v}^s + v^f [(d_0^f + \frac{v^f}{1-v^s} d_0^{sf}) \nabla \nabla \cdot \tilde{\mathbf{u}}^f \\
 &+ (e_0^f + \frac{v^f}{1-v^s} e_0^{sf}) \nabla \nabla \cdot \tilde{\mathbf{u}}^s] + (\mu^f + \lambda^f) \nabla \nabla \cdot \tilde{\mathbf{u}}^f + \mu^f \nabla^2 \tilde{\mathbf{u}}^f + \sum_{f'=1}^m D^{ff'} (\dot{\tilde{\mathbf{u}}}^s - \dot{\tilde{\mathbf{u}}}^{f'}) \\
 &- v^f \nabla p - G^f v^f \nabla \dot{v}^f
 \end{aligned} \tag{83}$$

where

$$\alpha_1^s = 2\alpha^s v^s, \quad a_1^s = 3a_o^s (v^s)^2 \tag{84}$$

$$\alpha_1^f = 2\alpha^f v^f, \quad a_1^f = 3a_o^f (v^f)^2 \tag{85}$$

Equations (82) and (83) are the generalized Biot's equations for multiphase flow through poro-elastic media.

The linearized form of continuity equations given by (4) and (5) become

$$\nabla v^s = -v^s \nabla \nabla \cdot \tilde{\mathbf{u}}^s \quad \nabla v^f = -v^f \nabla \nabla \cdot \tilde{\mathbf{u}}^f \quad (86)$$

In the absence of net fluid flow, for a constant pressure field, using (86), the linearized form of the wave propagation for a poro-elastic media saturated with several fluid phases becomes

$$\rho^s \ddot{\tilde{\mathbf{u}}}^s = \rho^s \mathbf{f}^s + (\lambda_1^s + a_2^s v^s) \nabla \nabla \cdot \tilde{\mathbf{u}}^s - \alpha_1^s \nabla \nabla^2 \nabla \cdot \tilde{\mathbf{u}}^s + \mu_1^s \nabla^2 \tilde{\mathbf{u}}^s + \sum_{f=1}^m \mathbf{e}_1^f \nabla \nabla \cdot \tilde{\mathbf{u}}^f \quad (87)$$

$$\rho^f \ddot{\tilde{\mathbf{u}}}^f = \rho^f \mathbf{f}^f + (a_2^f v^f + d_1^f) \nabla \nabla \cdot \tilde{\mathbf{u}}^f + (\mathbf{e}_1^s - c_1^f v^s) \nabla \nabla \cdot \tilde{\mathbf{u}}^s - \alpha_1^f \nabla \nabla^2 \nabla \cdot \tilde{\mathbf{u}}^f \quad (88)$$

where

$$\begin{aligned} a_2^s &= a_1^s - 2b_0^s v^s - b_0^f v^f, \quad a_2^f = a_1^f - 2c_0^f v^f - \frac{2v^f}{1-v^s} c_0^{sf} v^f \\ c_1^f &= \left(\frac{v^f}{1-v^s} \right)^2 c_0^{sf}, \quad d_1^f = v^f (d_0^f + \frac{v^f}{1-v^s} d_0^{sf}) \\ \mathbf{e}_1^s &= v^f (\mathbf{e}_0^f + \frac{v^f}{1-v^s} \mathbf{e}_0^{sf}), \quad \mathbf{e}_1^f = v^s \sum_{f=1}^m (\mathbf{e}_0^f + \mathbf{e}_0^{sf}) \\ \lambda_1^s &= v^s (\mu^s + \lambda^s + f_0^s), \quad \mu_1^s = v^s \mu^s \end{aligned} \quad (89)$$

Here it is assumed $G^s = G^f = 0$, and the damping effects are neglected. The higher order derivative terms given by $\nabla \nabla^2 \nabla \cdot \tilde{\mathbf{u}}^s$ and $\nabla \nabla^2 \nabla \cdot \tilde{\mathbf{u}}^f$ appear in Equations (87) and (88) due to the dependence of free energy functions on the gradient of phasic volume fractions.

Introducing the Helmholtz resolution of the displacement vectors

$$\mathbf{u}^s = \nabla \phi^s + \nabla \times \mathbf{A}^s, \quad \mathbf{u}^f = \nabla \phi^f \quad (90)$$

where ϕ and \mathbf{A} are the scalar and vector potentials, Equations (87) and (88) may be restated as

$$\ddot{\phi}^s = C_D^s \nabla^2 \phi^s - \frac{\alpha_1^s}{\rho^s} \nabla^4 \phi^s + \sum_{f=1}^m \frac{\mathbf{e}_1^f}{\rho^s} \nabla^2 \phi^f \quad (91)$$

$$\ddot{\mathbf{A}}^s = C_S^s \nabla^2 \mathbf{A}^s \quad (92)$$

$$\ddot{\phi}^f = C_D^f \nabla^2 \phi^f + \frac{(e_1^s - c_1^f v^s)}{\rho^f} \nabla^2 \phi^s - \frac{\alpha_1^f}{\rho^f} \nabla^4 \phi^f \quad (93)$$

where the body force is neglected and the speed of dilatational waves, C_D^s , C_D^f , and shear wave C_s^s are defined as

$$C_D^s = \frac{(\lambda_1^s + \mu_1^s + a_2^s v^s)}{\rho^s}, \quad C_s^s = \frac{\mu_1^s}{\rho^s} \quad (94)$$

$$C_D^f = \frac{(a_2^f v^f + d_1^f)}{\rho^f} \quad (95)$$

Equations (91) - (93) are the wave propagation equations in a poro-elastic media saturated with several fluid phases. It is seen that the dilatational waves in the solid and the fluid bodies are coupled, while the shear wave in solid is not affected by the presence of the fluid phase. When there is only a single fluid phase present, these equations reduce to a generalized form of those developed by Biot (1956, 1957) for wave propagation in saturated porous media. The effect of microstructures of the media appears in Equations (91) and (93) through the terms $\nabla^4 \phi^s$ and $\nabla^4 \phi^f$, which have no counter parts in Biot's classical model.

In the absence of a fluid phase, Equations (91) and (92) govern the wave propagation in a dry poro-elastic media. Equation (91) shows that the dilatational waves are dispersed by the effect of porous medium microstructure, while the shear wave remain unchanged except for the variation in the magnitude of the wave speed by the effect of porosity.

Multiphase Flows through Porous Media

For the special case of multiphase flows through a rigid porous media, assuming

$$b_0^f = c_0^{sf} = d_0^{sf} = e_0^f = e_0^{sf} = 0 \quad (96)$$

Equations (5) and (81) may then be restated as

$$\frac{\partial v^f}{\partial t} + \nabla \cdot (v^f \tilde{\mathbf{v}}^f) = 0 \quad (97)$$

$$\begin{aligned} \rho_0^f v^f \frac{d\tilde{\mathbf{v}}^f}{dt} = & \rho_0^f v^f \mathbf{f}^f - v^f \nabla p + \alpha_1^f \nabla \nabla^2 v^f - \beta_1^f \nabla v^f + \mu^f \nabla^2 \tilde{\mathbf{v}}^f \\ & + (\lambda^f + \mu^f) \nabla \nabla \cdot \tilde{\mathbf{v}}^f - \sum_{f'=1}^m \mathbf{D}^{ff'} \cdot \tilde{\mathbf{v}}^{f'} - G^f v^f \nabla \dot{v}^f \end{aligned} \quad (98)$$

where

$$\beta_1^f = v^f (3a_0^f v^f - 2c_0^f) + G^f \dot{v}^f \quad (99)$$

Equations (97) and (98) are the generalized form of Brinkman's equations for multiphase flows through porous media.

Generalized Darcy's Law

For a steady motion and when the spatial variations of fluid velocities are small, Equation (98) reduces to

$$\mathbf{D}^{ff} \cdot \tilde{\mathbf{v}}^f = \rho_0^f v^f \mathbf{f}^f - v^f \nabla p + \alpha_1^f \nabla \nabla^2 v^f - \beta_1^f \nabla v^f - G^f v^f \nabla \dot{v}^f \quad (100)$$

Equation (100) is the generalized Darcy's law for multiphase flows through porous media.

For the case of two-phase flows in porous media, the explicit form of the governing equations are given as

$$D^{11} \tilde{\mathbf{v}}^1 + D^{12} \tilde{\mathbf{v}}^2 = \rho_0^1 v^1 \mathbf{f}^1 - v^1 \nabla p + \alpha_1^1 \nabla \nabla^2 v^1 - \beta_1^1 \nabla v^1 - G^1 v^1 \nabla \dot{v}^1 \quad (101)$$

$$D^{21} \tilde{\mathbf{v}}^1 + D^{22} \tilde{\mathbf{v}}^2 = \rho_0^2 v^2 \mathbf{f}^2 - v^2 \nabla p + \alpha_1^2 \nabla \nabla^2 v^2 - \beta_1^2 \nabla v^2 - G^2 v^2 \nabla \dot{v}^2 \quad (102)$$

Noting that

$$v^1 = s(1 - v^s), \quad v^2 = (1 - s)(1 - v^s) \quad (103)$$

where $(1 - v^s)$ is the porosity and s is the saturation of phase 1, Equations (101) and (102) may be restated as

$$D^{11} \tilde{\mathbf{v}}^1 + D^{12} \tilde{\mathbf{v}}^2 = (1 - v^s) s [\rho_0^1 \mathbf{f}^1 - \nabla p + \alpha_0^1 \nabla \nabla^2 s - \beta_0^1 \nabla s - G_0^1 \nabla \dot{s}] \quad (104)$$

$$D^{21} \tilde{\mathbf{v}}^1 + D^{22} \tilde{\mathbf{v}}^2 = (1 - v^s) (1 - s) [\rho_0^2 \mathbf{f}^1 - \nabla p - \alpha_0^2 \nabla \nabla^2 s + \beta_0^2 \nabla s + G_0^2 \nabla \dot{s}] \quad (105)$$

where the coefficients are

$$\begin{aligned}\alpha_0^1 &= \frac{\alpha_1^1}{s}, \quad \beta_0^1 = \frac{\beta_1^1}{s}, \quad G_0^1 = G^1(1-v^s) \\ \alpha_0^2 &= \frac{\alpha_1^2}{(1-s)}, \quad \beta_0^2 = \frac{\beta_1^2}{(1-s)}, \quad G_0^2 = G^2(1-v^s)\end{aligned}\quad (106)$$

Equations (104) and (105) show that the spatial variations of saturation and time rate of change of saturation affects the phasic velocity field. In addition, the phases exert drag on one another. When $\nabla \nabla^2 s$ in Equations (104) and (105) are neglected, they resemble those proposed by Hasanizadeh and Gray (1993).

When the material parameters given in (106) are constants, Equations (104) and (105) may be restated as

$$D^{11}\tilde{\mathbf{v}}^1 + D^{12}\tilde{\mathbf{v}}^2 = (1-v^s)s[\rho_0^1 \mathbf{f}^1 - \nabla p^1] \quad (107)$$

$$D^{21}\tilde{\mathbf{v}}^1 + D^{22}\tilde{\mathbf{v}}^2 = (1-v^s)(1-s)[\rho_0^2 \mathbf{f}^2 - \nabla p^2] \quad (108)$$

Here the effective pressures, p^1 and p^2 , are defined as

$$p^1 = p - \alpha_0^1 \nabla^2 s + \beta_0^1 s + G_0^1 \dot{s} \quad (109)$$

$$p^2 = p + \alpha_0^2 \nabla^2 s - \beta_0^2 s - G_0^2 \dot{s} \quad (110)$$

The effective capillary pressure, p_c , may then be defined as

$$p_c = p^1 - p^2 = -(\alpha_0^1 + \alpha_0^2) \nabla^2 s + (\beta_0^1 + \beta_0^2) s + (G_0^1 + G_0^2) \dot{s} \quad (111)$$

That is, the phases will experience an effective pressure difference, which is a function of saturation and its spatial and time derivatives. Equation (111) in the absence of the spatial derivative term reduces to that proposed by Beliaev and Hassanizadeh (2001). Beliaev and Hassanizadeh have shown that (111) is capable of accounting for the hysteresis and dynamic effects in two-phase flows in porous media. Note that when both spatial and temporal variations of saturation are small, Equation (111) implies that the effective capillary pressure is a function of saturation, which is in agreement with the commonly assumed procedures, Scheidegger (1974).

The statement of conservation of mass given (97) in term of saturation becomes

$$\frac{\partial s}{\partial t} + \nabla \cdot (s \tilde{\mathbf{v}}^1) = 0 \quad (112)$$

$$\frac{\partial s}{\partial t} - \nabla \cdot [(1-s) \tilde{\mathbf{v}}^2] = 0 \quad (113)$$

Equations (107), (108), (112) and (113) form nine equations for finding $\mathbf{v}^1, \mathbf{v}^2, s, p_1$ and p_2 .

For each of phases, Equations (107) and (108) may be solved and restated as

$$\tilde{\mathbf{v}}_i^1 = K_{11}(\rho^1 f^1 - \nabla p^1) - K_{12}(\rho^2 f^2 - \nabla p^2) \quad (114)$$

$$\tilde{\mathbf{v}}_i^2 = K_{22}(\rho^2 f^2 - \nabla p^2) - K_{21}(\rho^1 f^1 - \nabla p^1) \quad (115)$$

where

$$K_{11} = \frac{s D^{22}}{D^{11} D^{22} - D^{12} D^{21}} (1 - v^s) \quad , \quad K_{12} = \frac{(1-s) D^{12}}{D^{11} D^{22} - D^{12} D^{21}} (1 - v^s) \quad (116)$$

$$K_{22} = -\frac{(1-s) D^{11}}{D^{11} D^{22} - D^{12} D^{21}} (1 - v^s) \quad , \quad K_{21} = -\frac{s D^{21}}{D^{11} D^{22} - D^{12} D^{21}} (1 - v^s) \quad (117)$$

For a single-phase flow through porous media, Equation (115) reduces to the Darcy law.

Conclusion

A continuum model for multiphase flows through poro-elastic media is developed. Based on the thermodynamics of the multiphase mixture flows, appropriate constitutive equations are formulated. The new model included the effects of phasic interaction and the elastic deformation of the media. The special case of wave propagation in poro-elastic media saturated with multiphase fluids is examined. It is shown that the nature of the shear waves is not affected by the presence of the pores saturated with the multiple fluids. The dilatational waves, however, is further dispersed by the microstructure effects of the media. It is also shown that the present theory contains, as its special cases, Biot's theory of poro-elastic media.

The special case of multiphase flows in rigid porous media is treated in detail. It is shown

that the model reduces to a generalized form of Darcy's law that includes the effects of phasic drag. In addition, the model naturally leads to an effective capillary pressure that is a function of saturation, and its spatial and temporal derivatives. As a result the model should be capable of accounting for the hysteresis and dynamic effects observed during drainage and imbibitions.

Multiphase Flows

When hydrate dissociates, it will produce a large amount of gas as well as water. In addition, in non-consolidated sediments the loose sand and soil will be generated. The current models assume only gas will flow and occasionally the effects of water flow are also included. At the present time, no model considers the potential for motion of solid materials during hydrate dissociation. We have developed a model for mixture flows including solid material. In this section some examples of the model predictions are presented and compared with the experimental data when possible.

Two-Phase Liquid-Solid Flows

The thermodynamically consistent model for two-phase liquid-solid flows and a computational procedure is used for solving dense two-phase flows over an inclined chute as a test case. Figure 16 shows a schematic of the dense mixture flow studied.

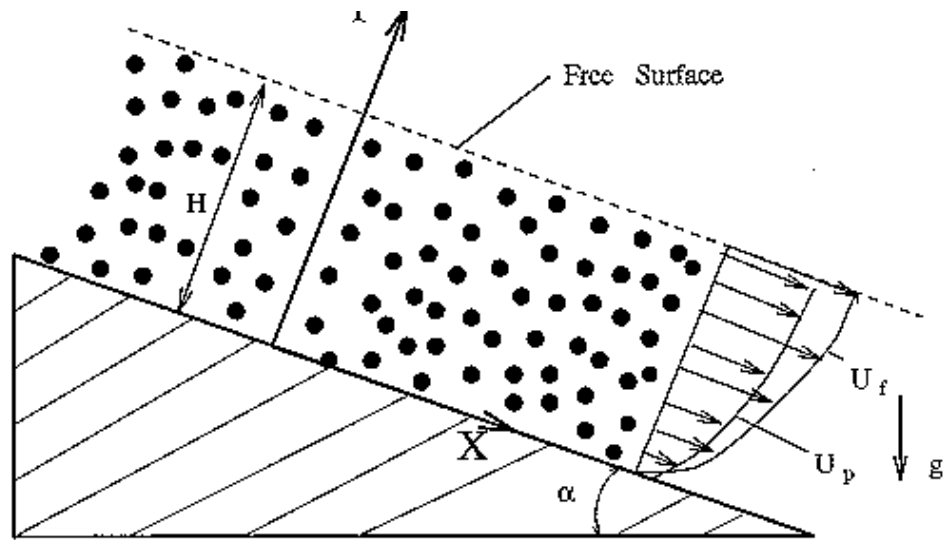


Figure 16. Schematics of the dense mixture flow.

The low speed and high concentration solid-liquid flows down inclined chutes with the liquid phase being in the viscous flow regime for different inclination angles are first simulated. The simulation results are shown in Figure 8 and are compared with the experimental data of Malekzadeh and Savage (1993a) and Malekzadeh (1993b). Malekzadeh's experiments were carried out for a chute with a length of 1.1 m, a width of 5.1

cm and a depth of 8 cm. Glass plates were used as the side-walls of the flume and the bottom was a replaceable rough aluminum surface. The solid particles were 3-mm glass beads with a density of $\rho_o = 2485 \text{ kg/m}^3$ and the liquid was a mixture of 80% Alkyl Benzyl Phtalate and 20% Dibutyl Benzyl Phtalate. This mixture had a density of $\rho_o^f = 1065 \text{ kg/m}^3$ and a viscosity of $\mu_o = 0.0455 \text{ N s/m}^2$. These values of experimental parameters were used in the computer simulation. In addition, a particle-particle restitution coefficient of $r = 0.5$, a particle-wall restitution coefficient of $r_w = 0.45$ and a particle-wall friction coefficient of $\hat{\mu}_w = 0.02$ were also assumed.

For the 3 mm glass beads-liquid mixture flowing down an inclined chute with an inclination of 13° , the simulated phasic velocity, solid phase fluctuation kinetic energy and solid volume fraction profiles are shown in Figure 17. Here the flow height is $H = 14.5 \text{ mm}$ and the loading ratio is $m = 3.65$ (which corresponds to an average solid volume fraction of $\nu_a = 0.57$). Figure 17a shows that in the region close to the chute bed, the velocity gradient is rather large and the velocity profile becomes quite flat near the free surface. This figure also shows that there exists a slip velocity of about 0.02 m/s for the particulate phase at the wall, while the slip between the two phases is generally very small. A careful examination of Figure 17a indicates that the particulate velocity is slightly larger than that of the liquid phase.

The experimental data of Malekzadeh and Savage (1993a) and Malekzadeh (1993b) for the chute mid-section (at $z = 2.5 \text{ cm}$) for the particulate phase velocity profile are reproduced in Figure 17a for comparison. It is observed that the predicted velocity is larger than the experimental data. This is mainly because the present simulation is for a wide chute, while the experimental data was for a narrow rectangular cross section chute. The side-walls of the experimental chute significantly retard the flow, which is not accounted for in the present wide-chute simulation.

Approximate analytical solutions for the homogeneous mixture approximation are also shown in Figure 17a for comparison. The corresponding effective density is $\rho_e = 1873 \text{ kg/m}^3$, and the effective viscosity of the equivalent homogenous fluid is $\mu_e = 2.74 \text{ N s/m}^2$. Figure 17a clearly shows that the analytical solution for the wide-chute agrees with our numerical simulation quite well, while the solution for the rectangular cross-section chute is in reasonable agreement with the experimental data.

The variation of particulate fluctuation kinetic energy k is shown in Figure 17b. It is observed that while the flow is in (low speed) viscous regime, the particulate fluctuation kinetic energy is relatively significant (particularly in the lower half of the channel). This figure also shows that the particulate fluctuation kinetic energy has a peak value near the

wall, and then decreases rapidly toward the free surface. Figure 17c presents the comparison between the predicted solid volume fraction and the experimental data of Malekzadeh and Savage (1993a) and Malekzadeh (1993b). It is observed that the agreement between the numerical simulation results and the experimental data is quite good. This figure also shows that the variation of solid volume fraction is quite small and ν is nearly constant across the depth of the flow. This is perhaps the reason for the success of the homogeneous flow approximation in providing reasonably accurate results in this case.

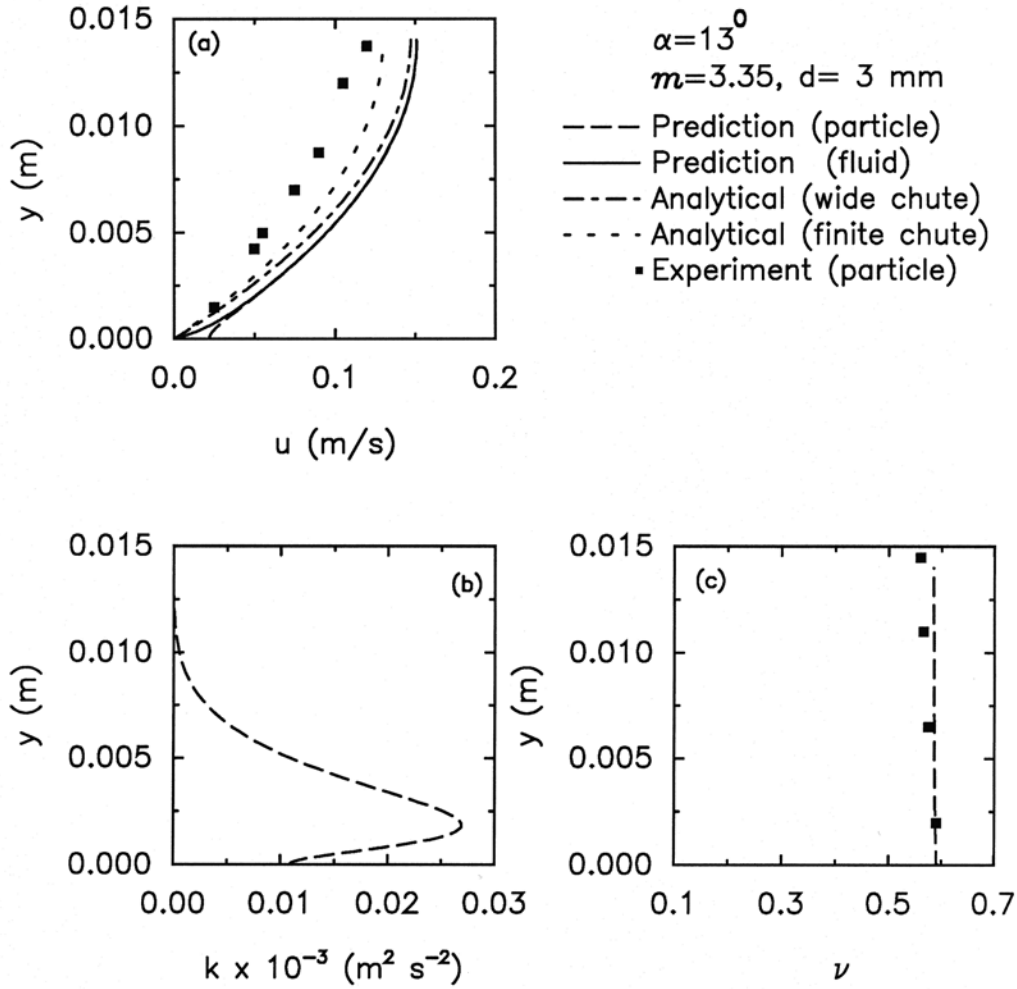


Figure 17. Variations of mean velocity, fluctuation kinetic energy and solid volume fraction profiles for 3 mm glass bead-liquid (20% BDP and 80% ABP) mixture down a 13° inclined chute. Comparison with the experimental data of Malekzadeh and 1-D and 2-D analytical solutions.

Figure 18 presents the variations of the corresponding phasic mean viscosity μ and μ^f and the particulate phase collisional and fluctuation viscosity μ^T . It is observed that μ and μ^f are nearly constant, while μ^T first increases to its maximum value at a short distance from the wall, and then decreases toward the free surface. Comparing with μ and μ^f , however, μ^T is relatively small with its peak being about 5% of μ . This means that the effect of particle's collision is not very significant in such low speed but dense two-phase flows. The effective viscosity μ_e is shown in Figure 18c, indicating that μ_e is roughly constant across the chute. This observation further justifies the use of an effective constant viscosity in our earlier derivations.

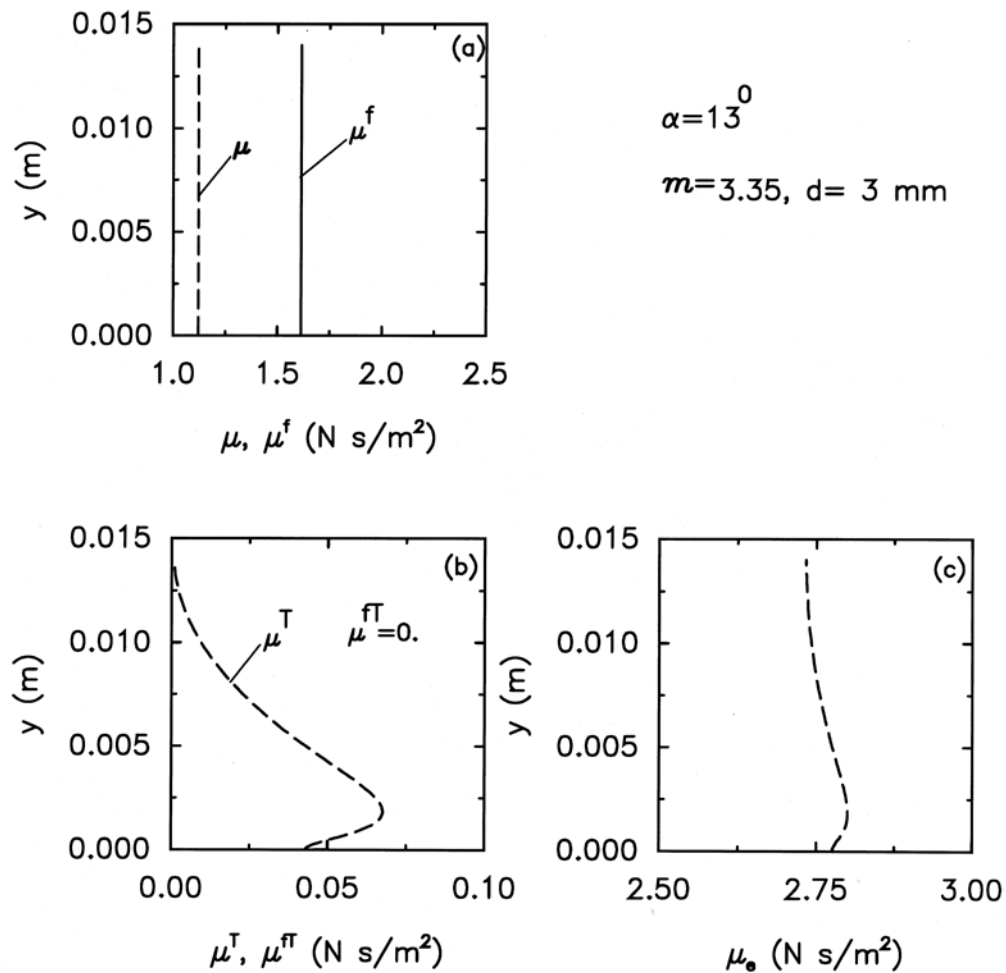


Figure 18. Variations of phasic and effective viscosity profiles for 3 mm glass bead-liquid mixture down a 13° inclined chute.

Variations of the phasic normal and shear stresses, as well as the total normal and shear stresses are shown in Figure 19. Note that the normal stresses shown here are the excess stresses beyond the hydrostatic pressure p^f , which is of the order of 270 N/m^2 near the wall. Since the liquid phase is essentially in the laminar flow regime with negligible fluctuation kinetic energy, the liquid phase excess normal stress is zero. Thus, the total normal stress is the same as the particulate normal stress as shown in Figure 19a. The particulate (total) normal stress has a peak value near the bottom wall and then decreases toward the free surface. The phasic and total shear stress profiles are shown in Figure 19b. The fluid phase shear stress has a large value at the solid wall and monotonically decreases toward the free surface, while the particulate phase shear stress first increases to a peak value near the wall and then decreases toward the free surface. As is expected, the total shear stress has a linear variation across the chute.

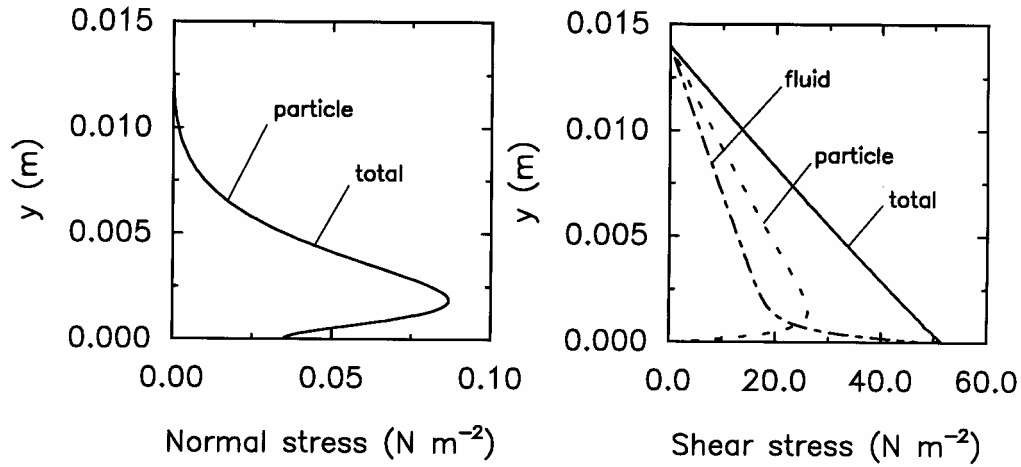


Figure 19. Variations of normal and shear stresses profiles for 3 mm glass bead-liquid mixture down a 13° inclined chute.

The experimental data for the particulate velocity at the chute centerline as reported by Malekzadeh and Savage (1993) and Malekzadeh (1993) for an inclination angle of 17 degrees are reproduced in Figure 20. The flow channel flow height was 10 mm in this case. The present model is used to study chute flow with the inclination angle of 17 degree is studied. All other parameters are kept identical to those used earlier for the inclination angle of 13 degrees described in the earlier reports. The corresponding phasic velocity, fluctuation kinetic energy and solid volume fraction profiles are evaluated and the results are shown in Figure 20. The results for the analytical solutions that were described in the last year report

are also presented in Figure 20 for comparison. It is observed that the agreement of model predictions with the experimental data is quite good.

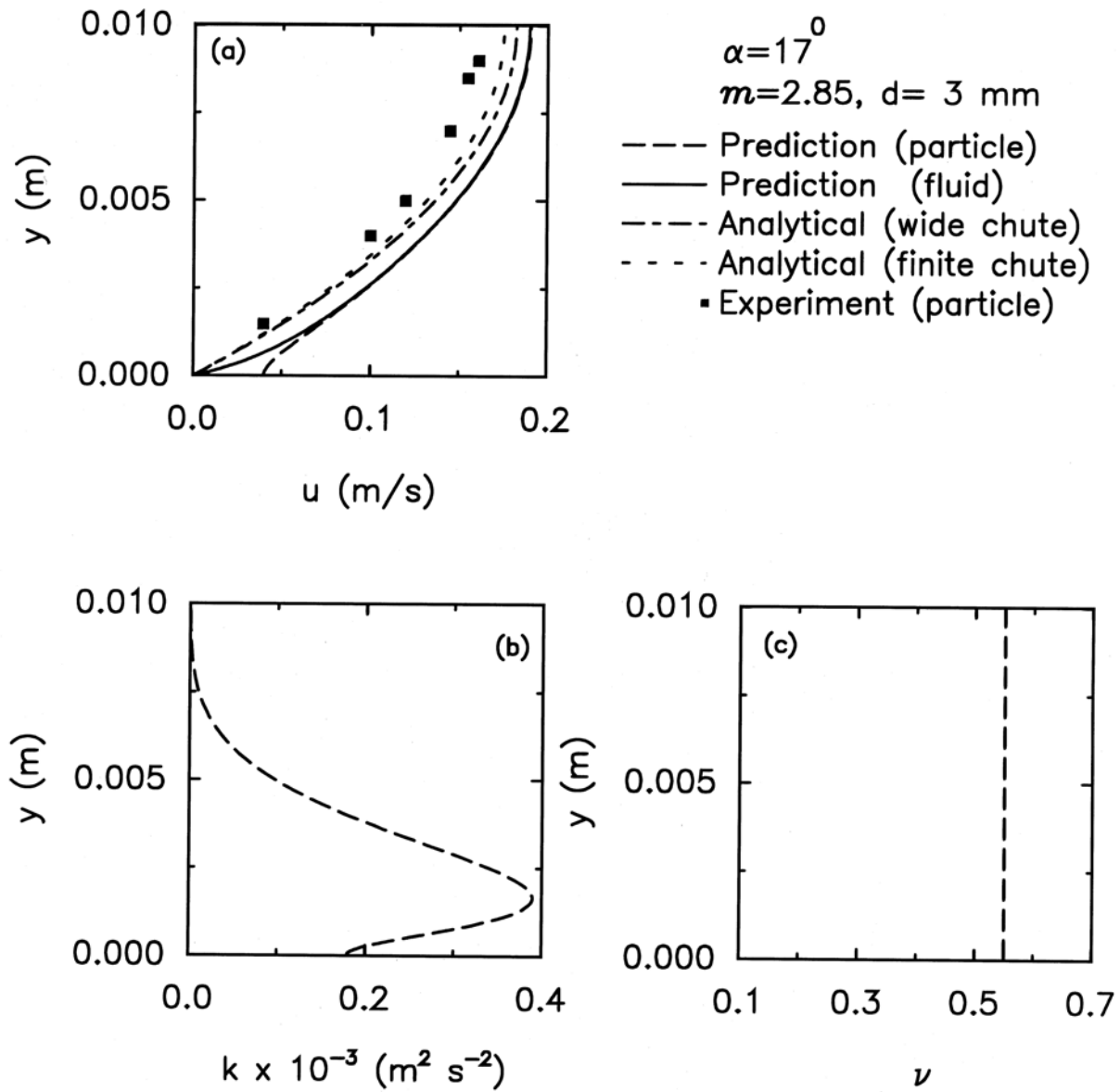


Figure 20. Variations of mean velocity, fluctuation kinetic energy and solid volume fraction profiles for 3 mm glass bead-liquid (20% BDP and 80% ABP) mixture down a 17 degrees inclined chute. Comparison with the experimental data of Malekzadeh and 1-D and 2-D analytical solutions.

For a mixture of 0.5 mm glass beads-water flowing down a 15° inclined chute, the predicted phasic velocity, fluctuation kinetic energy and solid volume fraction profiles were described in the earlier reports. Here the flow height is 3 cm and loading ratio is $m=0.125$. Figure 21 presents the variations of the phasic coefficients of viscosity μ (effective particulate viscosity), μ^T (particulate collisional/ turbulence viscosity), μ^f (effective fluid viscosity), and μ^{fT} (fluid turbulence viscosity), across the chute. It is observed that the mean coefficient of viscosity μ and μ^f first increase with the distances from the wall, and then decreases toward the free surface. The combined collisional and kinetic particulate viscosity, μ^T , is nearly constant with a slightly increase near the wall. The fluid turbulence viscosity, μ^{fT} , however, monotonically increases with the distance from the wall. The collisional and turbulence viscosities μ^T and μ^{fT} are much larger in magnitudes when compared with μ and μ^f with μ^{fT} playing the dominant role.

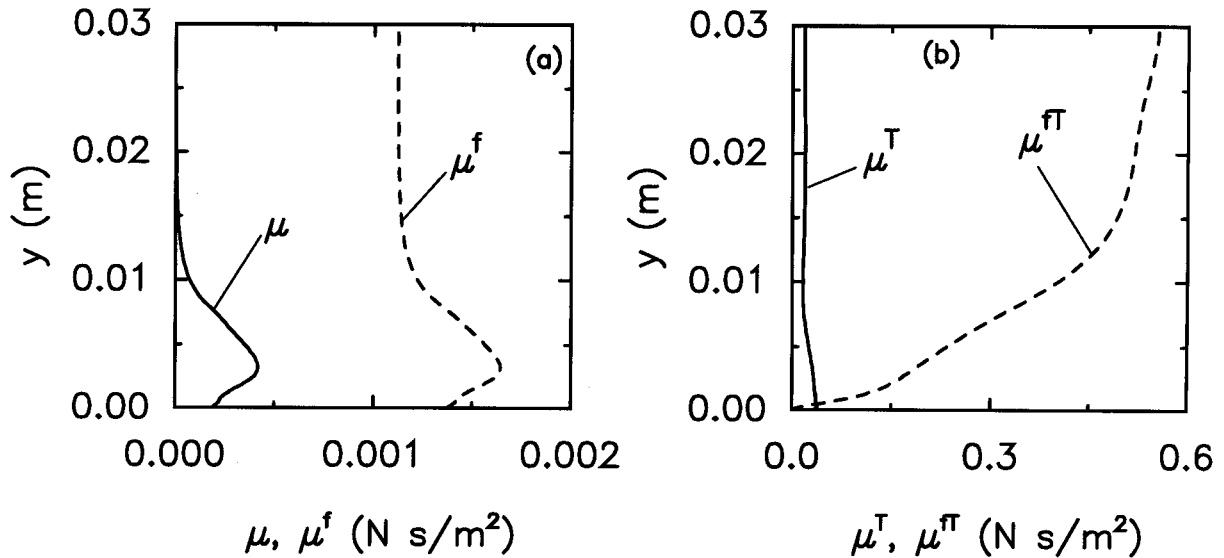


Figure 21. Variations of phasic mean and turbulence viscosities for 0.5 mm glass bead-water suspension flowing down an inclined chute at an angle of 15°.

Figure 22 presents the phasic energy production and dissipation profiles. It is observed that both the particulate and the water phasic fluctuation kinetic energy productions and dissipations are quite large at the wall, and decrease rapidly with the distance from the wall. This figure also indicates that the energy production of each phase is nearly balanced by its energy dissipation rate and the amount of fluctuation energy transfer between the phases is relatively small.

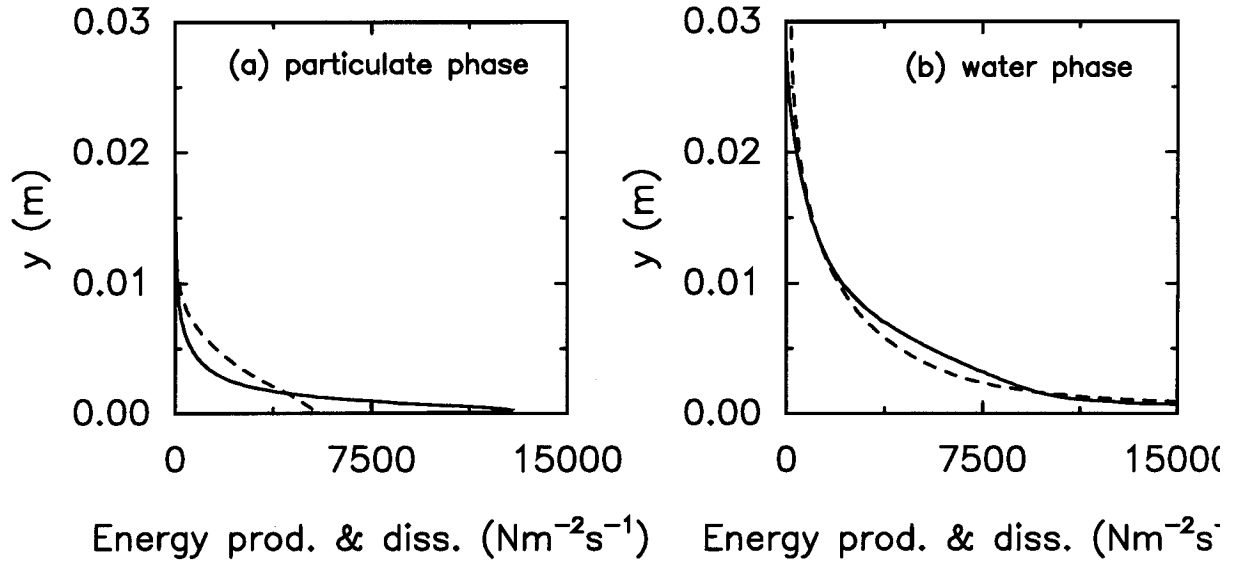


Figure 22. Variations of energy production and dissipation profiles for 0.5 mm glass bead- water suspension flowing down an inclined chute at an angle of 15°.

Two-Phase Liquid-Gas Flows in fractured Media

We have initiated a series of analysis of gas-liquid flows in fractured media with application to the flow process during hydrate dissociation. After the hydrate dissociates, it is expected that the flow of natural gas and water (and possibly solid phases) will be channeled into fractures of the reservoir rather than homogenous matrix. To gain an understanding of the flow process, several simulations are initiated and the preliminary results are described in this section.

a) Gas-liquid Flows

Gas-liquid mixture flows in a fracture is simulated using a volume-of-fluid model. In this model the density in each computational cell is evaluated based the amount of gas and liquid present in the cell. As a result, the density variation accounts for the level of concentration of different phases. For a two-dimensional section of a fracture, Figure 23 shows a sequence of simulation results for time evolution of density. It is seen that the density changes from the density of the gas to that of the liquid in various region. It also appears that the flow resembles an annulus flow with liquid covering the areas near the walls, while the gas flows in the central areas.

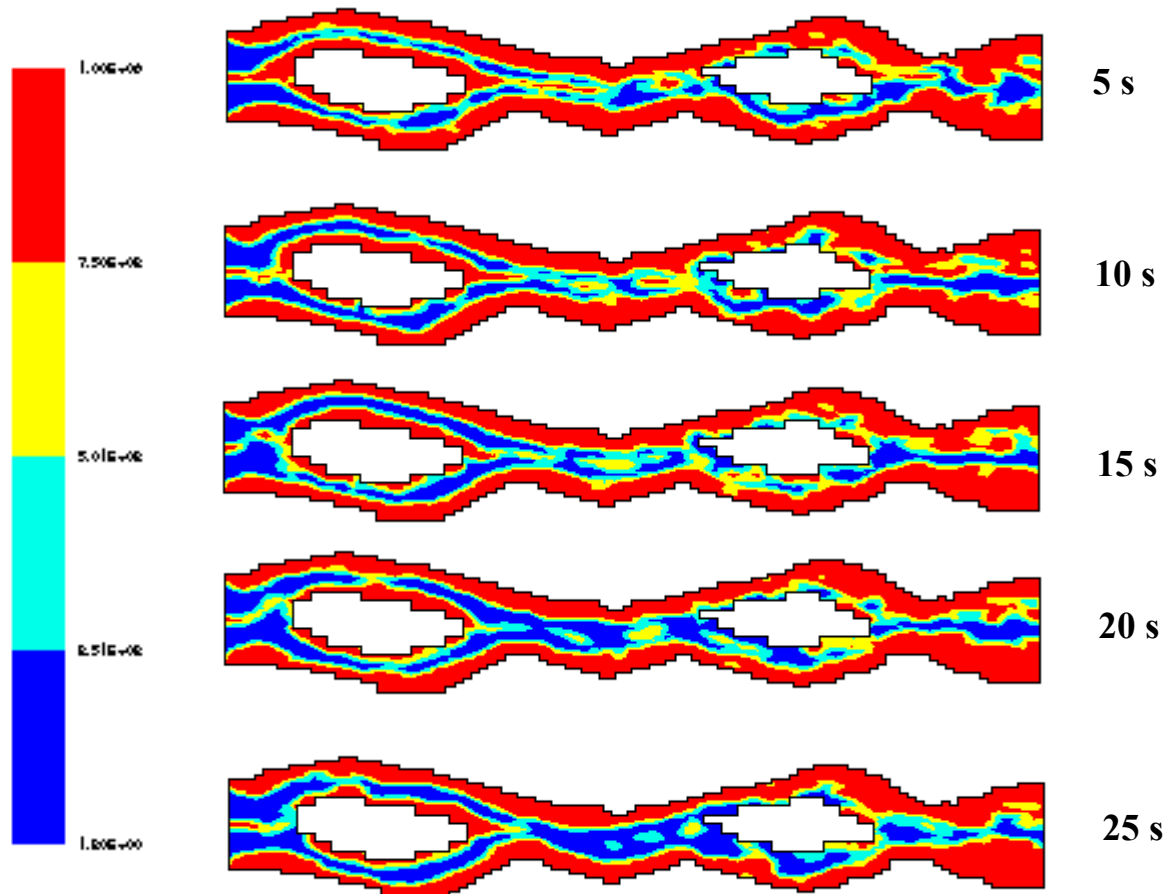


Figure 23. Variations of density for a gas-liquid flow in a fracture.

Figure 24 shows the details of the density variation in another model of fracture. Here the surface fracture is more smooth compare to the one shown in Figure 23. It is also assumed that fracture is originally water saturated. Natural gas generated by the hydrate dissociation moves as the invading fluid in the complex flow region in the fracture.

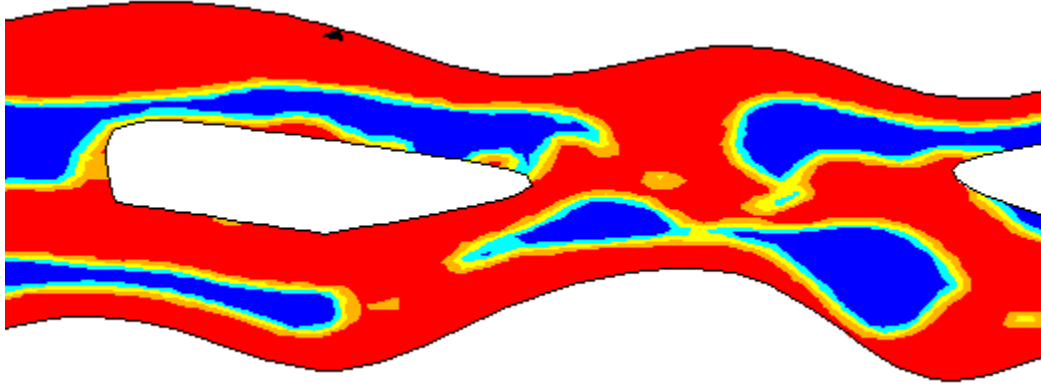


Figure 24. Details of density variation for a gas-liquid flow in a fracture model.

b) Gas-liquid-solid Flows

We have also initiated a new set of simulations for three-phase gas-liquid-solid flows in fractures. Here an Eulerian-Lagrangian model is used, where liquid is treated as the continuous media and gas are assumed to be in bubble forms. The particles are model as rigid spheres. The interactions of the three phases are included in the model.

Experimental Hydrate Formation and Dissociation in Unconsolidated Media

A series of experiments for providing quantitative data during hydrate formation and dissociation in unconsolidated sediment in the experimental setup were performed. In this section the experimental data for the time evolutions of pressure, temperature and propane mass flow rate during hydrate formation and dissociation are presented. Crushed ice and mixtures of crushed ice and glass bead were used as the media in this experimentation.

Experimental Setup

An experimental setup for studying propane hydrate formation and dissociation was fabricated. The setup was designed to provide for a visual inspection of hydrate formation and dissociation process in non-consolidated sediments. The setup consists of a transparent pressure vessel, data acquisition system, propane supply tank, pressure regulator, cold-water bath, circulating heat pump, and refrigeration unit. A schematic of the experimental setup is shown in Figure 25. Various component of the setup are described in this section.

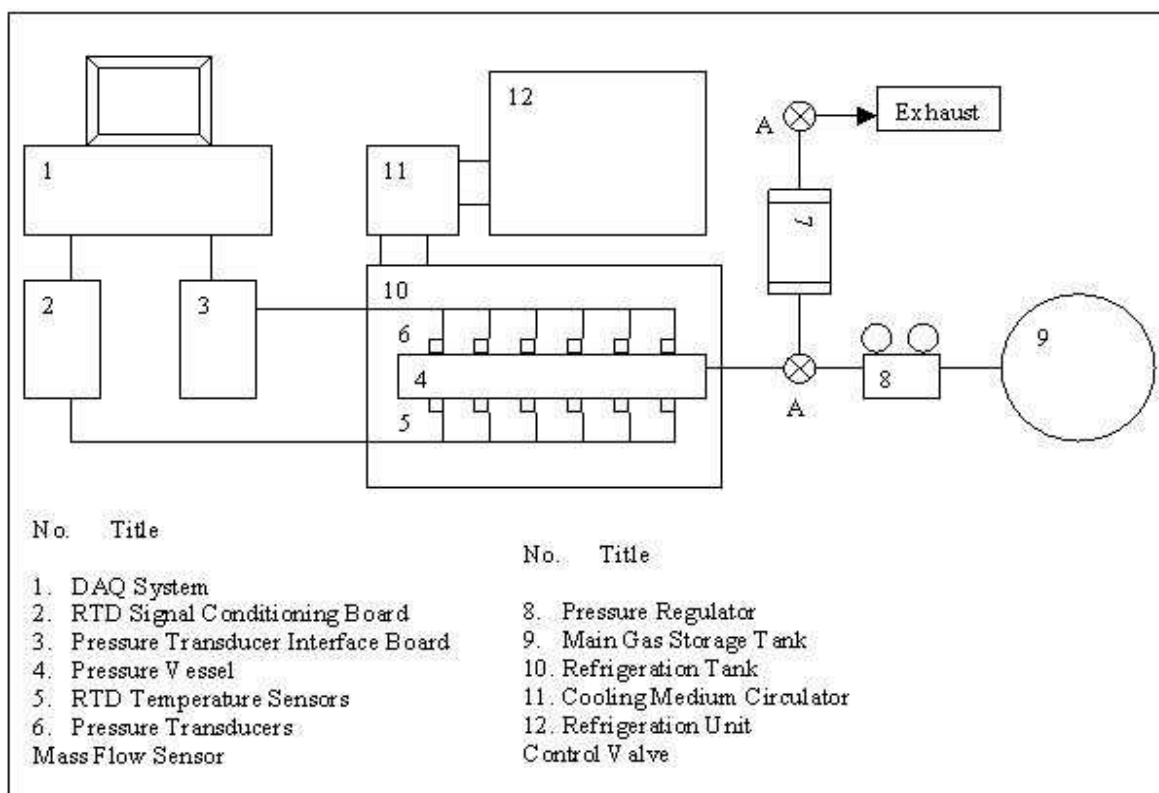


Figure 25. Schematic of the experimental setup.

The propane used for the experiments was chemically pure 99.95% propane. A pressure regulator on the tank outlet was used to maintain system pressure. From the tank and regulator, the propane enters the switching valve system, through a mass flow meter and into the pressure vessel. A switching valve system was incorporated so that the mass flow rate during formation and dissociation can be measured by the flow meter. A vacuum pump was also connected to the valve for evacuating the system before initiating the hydrate formation process. The outlet was routed to a fume hood to allow for exhausting the gas during the dissociation process.

From the valve system, the propane enters the pressure vessel through the inlet/outlet orifice. The pressure vessel is a billet 7075 aluminum unit with a Plexiglas top and bottom to allow for visual inspection of the sample during propane hydrate formation and dissociation. The vessel has internal dimensions of $25.5 \times 7.8 \times 6.5 = 1,293 \text{ cm}^3$. The top and bottom surface are constructed of 1.0 cm thick Plexiglas, which is reinforced with 0.4 cm thick aluminum trim rings. A 0.3 cm thick Buna-n (Nitrile) rubber gasket seals the Plexiglas to the aluminum body. Figure 26 shows a schematic of the components of the pressure vessel. A picture of the pressure vessel is shown in Figures 27 and 28.

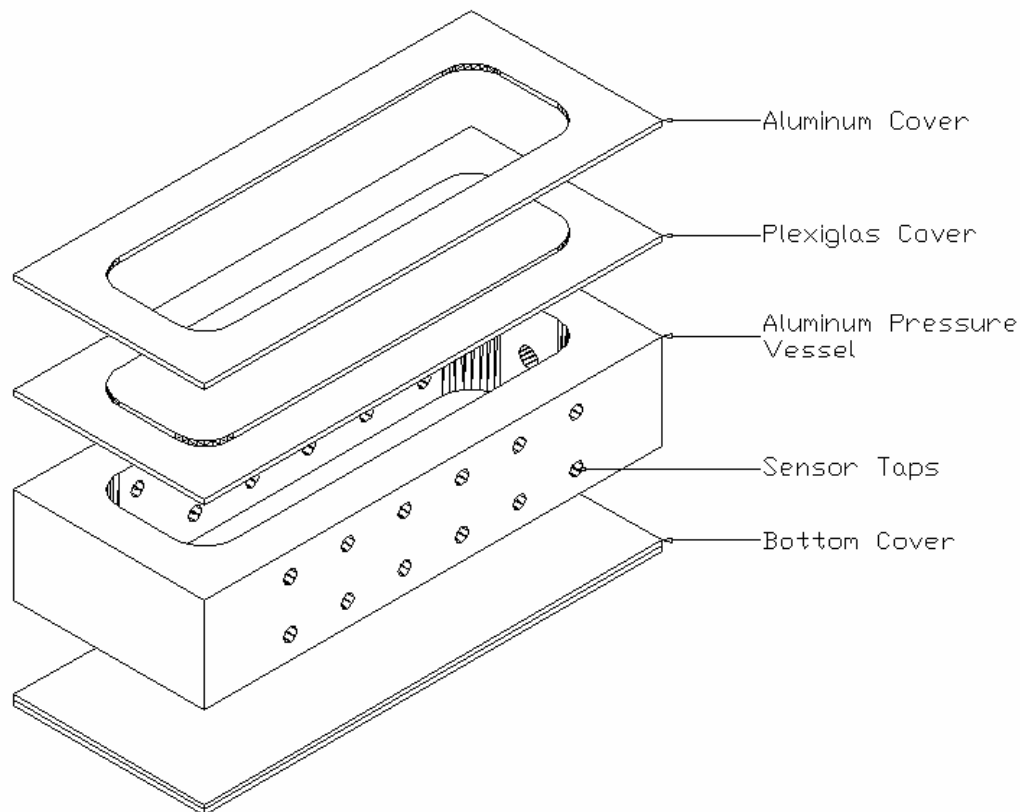


Figure 26. Schematic of the pressure vessel.

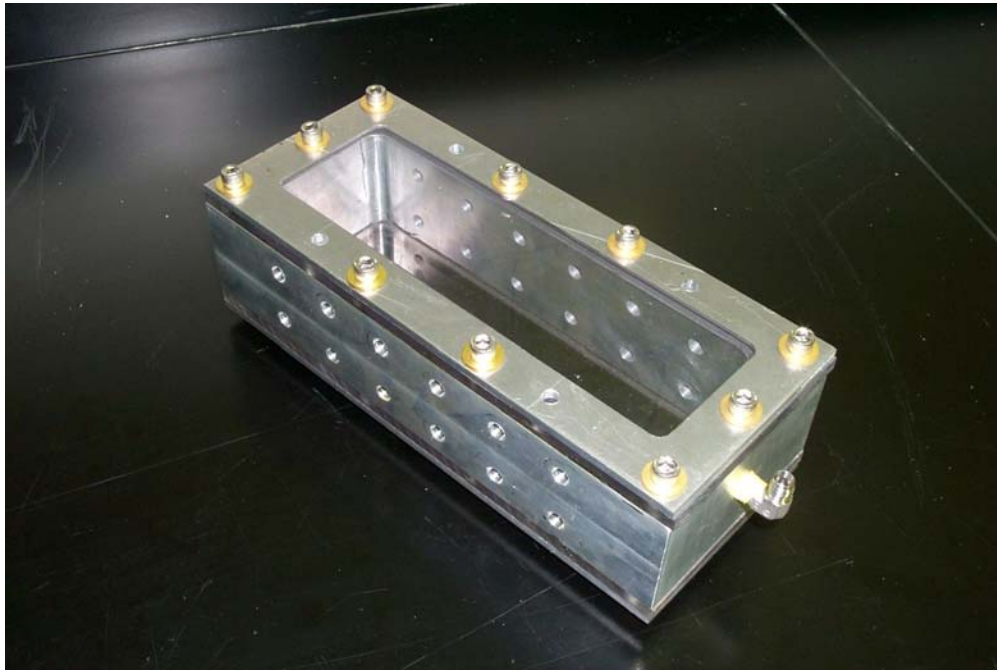


Figure 27. Fabricated hydrate pressure vessel.



Figure 28. Fabricated hydrate pressure vessel with the measuring sensors. As shown in Figures 28 and 29, the vessel body houses six pressure sensors and six

temperature sensors for monitoring the sample conditions at any time during the experimentation. The pressure sensors are 0-60 psi gauge units (Druck PTX/PMP 1240) with an output from 1 to 5 volts. The pressure sensors are powered by an external, regulated power supply. Pressure taps allow the sensors to be remotely mounted, with pressure lines connecting the taps to the sensors. Swagelok® connectors are used throughout to ensure a leak free system. The temperature sensors are 3-wire, platinum, 100 Ω RTD probes. The 3-wire RTD's alleviate the long lead wire resistances from affecting the signal reading. The tips of all sensors are located at the horizontal centerline of the vessel. All pressure and temperature sensors are connected to two National Instruments PCI-6023E DAQ boards, housed within an 800Mhz AMD® Duron computer system. The data acquisition system is controlled by a National Instruments LabView® code that has been developed. The code allows up to a sample rate of 1024 samples per second and can perform statistical evaluation of the data as needed. The data in the course of each experiment was recorded on a computer for compilation and analysis.

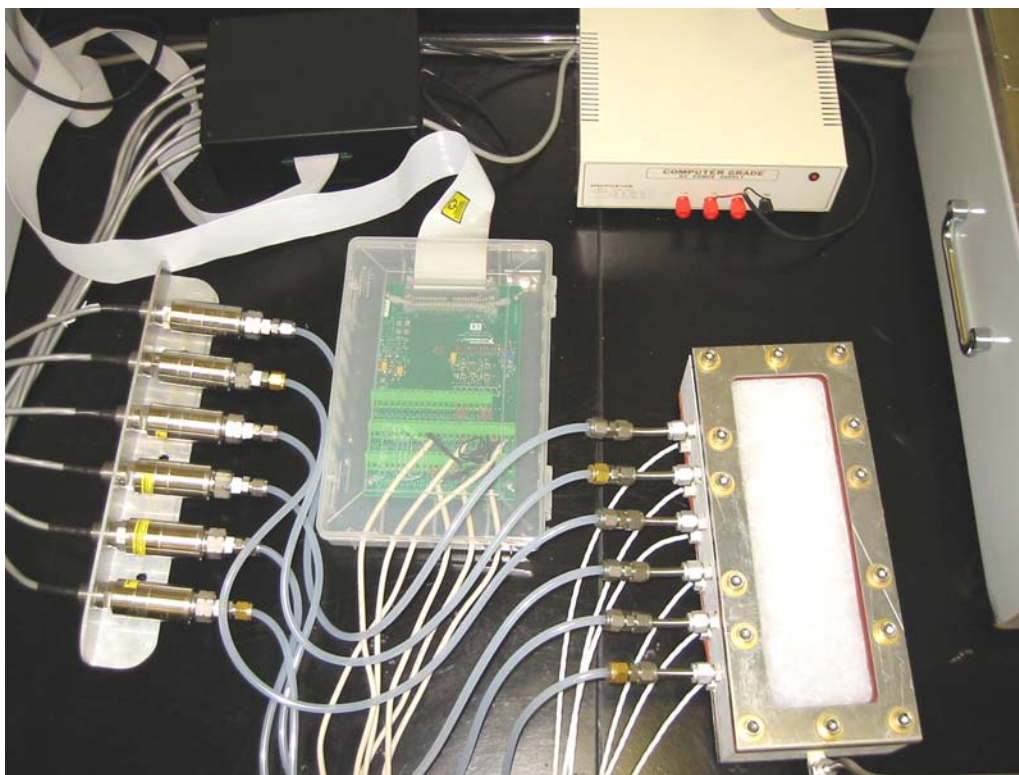


Figure 29. A picture of pressure and temperature sensors.

A mass flow meter recorded the amount of propane entering and exiting the pressure

vessel. Since the mass flow meter can only read flow in one direction, a switching valve system was incorporated into the system to allow for mass flow rate measurements. The mass flow meter had a range of 0 to 50 standard liters per minute (sLPM). The meter is also temperature compensated and is calibrated to the density of propane. A schematic of the switching valve system is shown in Figure 30.

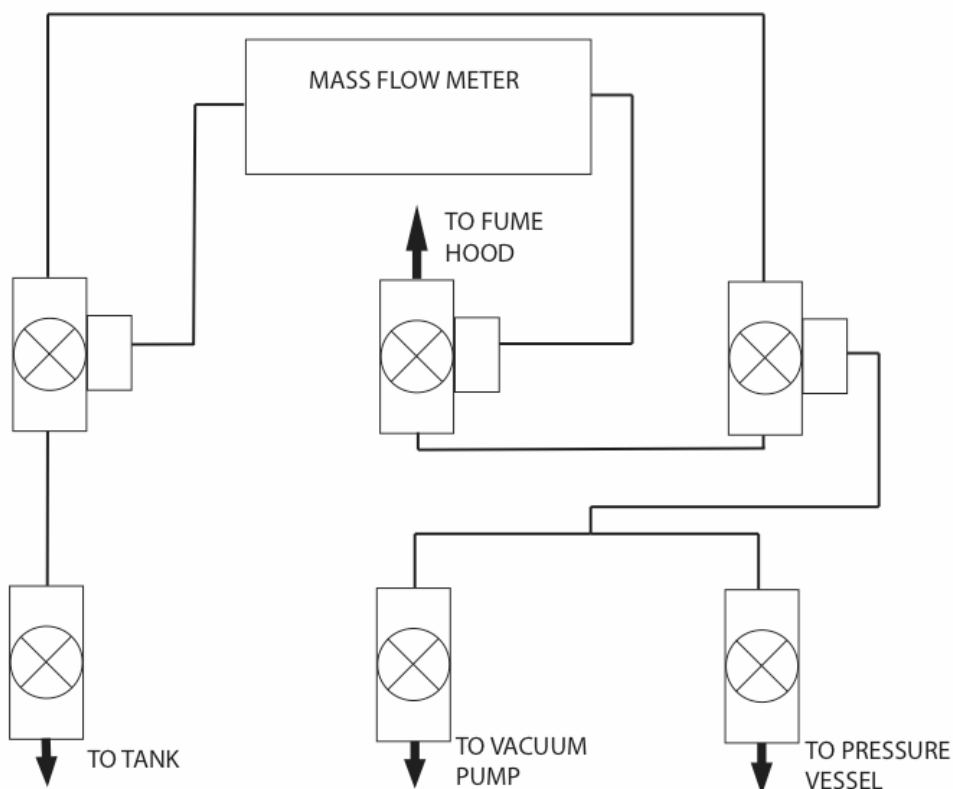


Figure 30. Schematic of valve switching system.

The pressure vessel and the attached sensors was submerged in a cold water/glycol bath and was kept at to -10°C during the entire formation and dissociation experiment. The 50/50 mixture of water and glycol coolant is contained in a Lauda M30 bath, with a Lauda MS circulator/heater attached. The MS circulator/heater pumps the coolant through a Cole-Parmer chiller, and with the chiller/heater combination, a constant temperature is maintained at all times. The bath circulation ensures a constant bath temperature throughout the experiment. Pictures of the cooling bath system are shown in Figures 31 and 32.



Figure 31. A picture of constant temperature bath system.

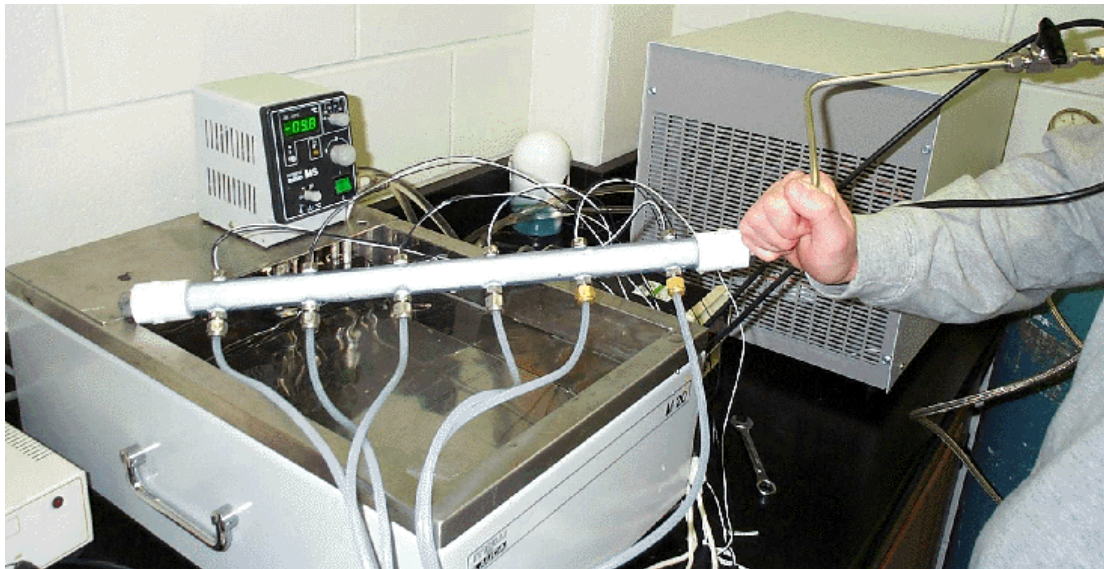


Figure 32. A picture of constant temperature with an earlier pressure vessel.

The following step-by-step procedure was used in the experimentation:

- Chill the bath to -10 °C with circulator and chiller.
- Place vessel and hardware in -20 °C environment.
- Shred ice and mix with glass beads as required.
- Place ice-glass beads mixture in -20 °C environment.
- Pack uniformly the ice-glass beads mixture into the pressure vessel.
- Seal top to vessel and place in -10 °C constant temperature bath.
- Start the data acquisition system.
- When media in the pressure vessel reaches to a constant temperature, evacuate air from system with the vacuum pump.
- Start propane injection at a constant pressure (40-50 psi).
- Record data as pressure falls during hydrate formation process.
- When pressure reaches to a roughly steady state, inject additional propane at constant pressure.
- When pressure decrease becomes negligible (normally after five days), assume that sufficient hydrate was formed and initiate the dissociation study by depressurization.
- When mass flow meter reading approaches zero, assume that the dissociation experiment is completed.

This procedure was followed for each experiment to ensure consistency.

Simplified Hydrate Formation and Dissociation Model

A simplified model for hydrate formation and dissociation in the pressure vessel is described in this section and is used for interpreting the experimental data. The statement of conservation of mass for propane in the pressure vessel during the hydrate formation or dissociation process is given as

$$\frac{d(\rho V)}{dt} = -k(p - p_{eq})^n + \dot{m} \quad (118)$$

Here V is the available void space in the vessel, ρ is the mass density of the propane, p is propane pressure, p_{eq} is the propane hydrate equilibrium pressure, k and n are reaction rate constants, and \dot{m} is the rate of mass of propane injected into the vessel during formation or rate exhausted during the hydrate dissociation. (\dot{m} is considered positive for flow into the vessel.) The first term on the right hand side of Equation (118) is rate of production or dissociation of hydrate in the vessel. Here a simplified version of Kim-Bishnoi rate model is used. Equation (118) may be restated as

$$\frac{V}{RT} \frac{dp}{dt} = -k(p - p_{eq})^n + \dot{m} \quad (119)$$

where a simple perfect gas law is assumed.

Hydrate Formation

At the initial stage when the propane is pumped into the vessel, neglecting the hydrate formation for the short time duration, Equation (119) reduces to

$$\frac{dp}{dt} = \frac{RT}{V} \dot{m} \quad (120)$$

Integrating (120), the pressure at the end of injection, p_1 in the vessel becomes

$$p_1 - p_o = \frac{RT}{V} \Delta m \quad (121)$$

where p_o is the initial pressure and T is the sample temperature which is assume to a constant equal to the bath temperature, and Δm is the total amount mass injected into the vessel. Equation (121) relates the change in the vessel pressure to the amount mass injected.

During the process of hydrate formation, neglecting the gas injection period, Equation (119) may be restated as

$$\frac{dp}{dt} = -k_1(p - p_{eq})^n, \quad k_1 = \frac{kRT}{V} \quad (122)$$

Integrating Equation (122), for $n \neq 1$, we find the time variation of the pressure in the vessel. That is,

$$\frac{1}{(p - p_{eq})^{n-1}} - \frac{1}{(p_1 - p_{eq})^{n-1}} = (n-1)k_1 t \quad (123)$$

where p_1 is the initial pressure after the vessel is pressurized. Similarly for $n = 1$, the expression for pressure becomes

$$\frac{p - p_{eq}}{p_1 - p_{eq}} = e^{-k_1 t} \quad (124)$$

Equations (123) and (124) show the decay of pressure in the vessel during propane hydrate formation. The rate of decay (value of k_1) may be found from the experimental data for different cycles and under different conditions.

Hydrate Dissociation

During the dissociation process, the vessel outlet is opened to the atmosphere. It is assumed that the mass flow rate leaving the vessel is proportional to the pressure difference and is given as

$$\dot{m} = -k_2(p - p_{atm}) \quad (125)$$

Equation (119) may then be restated as

$$\frac{dp}{dt} = -\frac{RT}{V}(k + k_2)p + \frac{RT}{V}(kp_{eq} + k_2p_{atm}) \quad (126)$$

Integrating Equation (126), the pressure variation during the dissociation is given as

$$p = p_o e^{-k_3 t} + \frac{A}{k_3}(1 - e^{-k_3 t}), \quad p_o = p|_{t=0} \quad (127)$$

where

$$k_3 = \frac{RT}{V}(k + k_2), \quad A = \frac{RT}{V}(kp_{eq} + k_2p_{atm}) \quad (128)$$

and p_o is the initial vessel pressure just before the dissociation by depressurization begin. Equations (127) and (128) give the expression for the pressure in the vessel during the propane hydrate dissociation process.

For large time, Equation (127) leads to

$$p = \frac{A}{k_3} = \frac{kp_{eq} + k_2p_{atm}}{k + k_2} \quad (129)$$

When all the hydrated in the vessel is depleted, neglecting the term involving the rate of dissociation (i.e., $k=0$), and the pressure approaches atmospheric condition.

Hydrate Formation Results

A series of experiments were performed for obtaining details of variation of pressure, temperature and mass flow rate data during the formation and dissociation of propane hydrate in porous media composed of crushed ice, and mixtures of crushed ice and glass beads. The pure crushed ice was used for basic understanding and as a base line. The cases that the mixture contained 25% and 50% glass beads were also studied. The percentage of glass beads to ice were on volumetric basis in these experiments. The glass beads-crushed ice mixtures were used to simulate the natural in-situ hydrate formation and dissociation in the unconsolidated sediments. Glass beads were selected to represent sands in geological formation but with a known particle size, distribution and shape. Having a known particle size and shape is expected to facilitate the interpretation of the data and is important to the model development for hydrate formation and dissociation in geological reservoirs. The crushed ice particles that were generated by shaving ice cubes tend to be flakes of about 2mm wide. The corresponding equivalent diameter sphere radius was 0.45mm.

As described earlier, the top and bottom walls of the pressure vessel were constructed of Plexiglas, which allowed the visual inspection of the hydrate formation and dissociation process. This provided an additional tool for physical interpretation of the experimental data. In addition, any formation irregularities or dissociation patterns could have been visually apparent through the transparent vessel walls.

The computer data acquisition system, described in Experimental Setup section, ensured the reproducibility of the data collection procedure. The duration of an experiment was approximately six days, which would vary somewhat depending on the requirements of the particular experiment. The first five days were typically necessary for hydrate formation, while a 24-hour period was required for the hydrate to dissociate to a point where the gas output dropped to below measurable levels.

The data collected for pressure, temperature and mass flow rate variations, during formation and dissociation phase are described separately in the following sections.

Propane Hydrate Formation in Pure Crushed Ice

The experiments with crushed ice were performed as a baseline study and for providing a fundamental understanding of the process of formation in bulk hydrate systems. Figure 33 shows a representative pressure time evolution for one experiment encompassing the entire formation and dissociation period. As noted before, there were six sensors in the vessel that were arranged at a distance of 5 cm apart with sensor 1 being closest to the

inlet/outlet and sensor 6 being the furthest.

Figure 33 shows are all the components of the hydrate formation and dissociation cycle. As outlined in the section on experimental procedure, the hydrate formation in the experimental pressure vessel required several steps. At the time initial time, when the vacuum pump is connected to the pressure vessel, the pressure drops to -13.5 psig. Then the regulator on the propane tank opens, which raises the pressure sharply to about 50 psi. In the first few hours at the start of the experiment, pressure regulator is opened several times in order to maintain the vessel pressure above the equilibrium hydrate formation pressure.

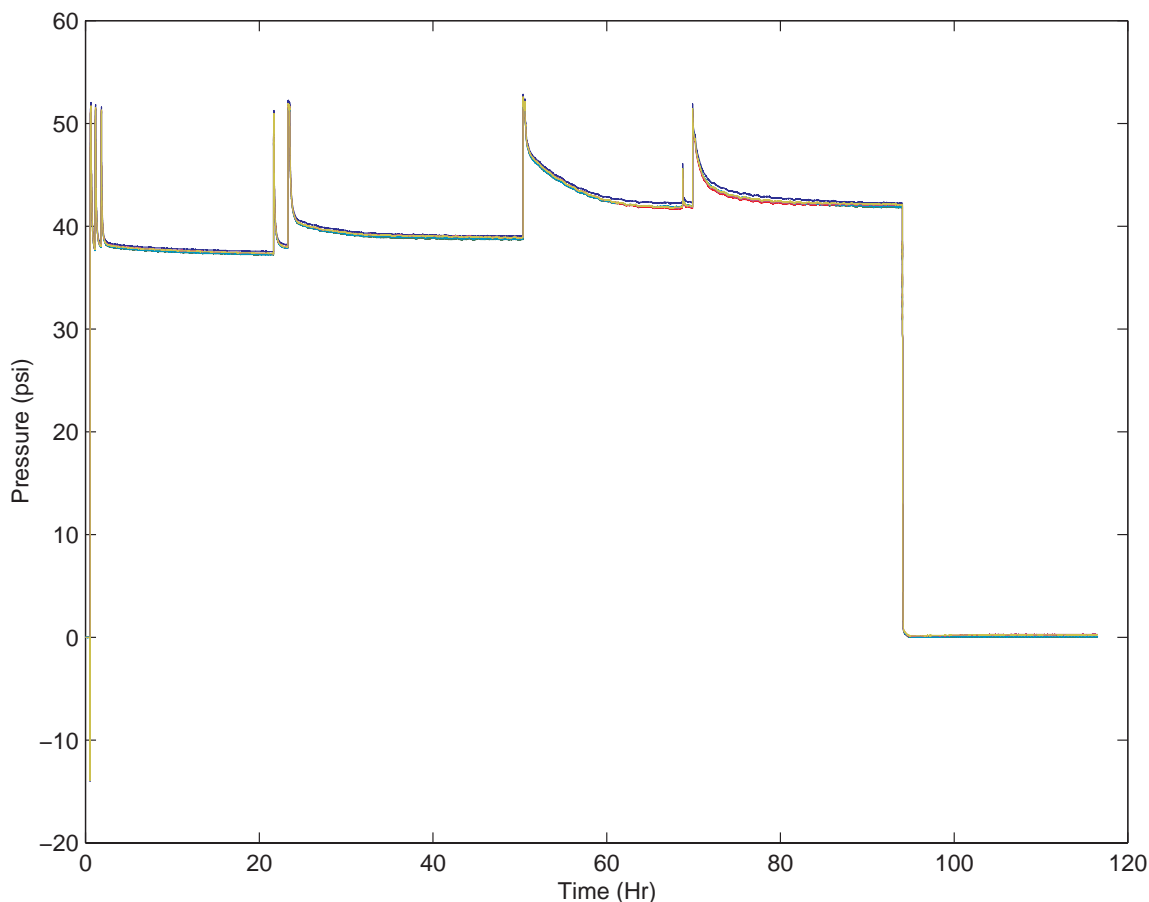


Figure 33. Time evolution of gauge pressure for hydrate formation and dissociation in crushed ice.

Every time after pressurization of the vessel, the pressure decays roughly exponentially approaching the equilibrium pressure. The hydrate formation process decreases as the equilibrium pressure approached. The bath temperature was kept constant at -10 °C in these experiments. Figure 33 shows that as the hydrate forms, decreasing the

available surface of crushed ice particles present in the vessel, the time required to approach the equilibrium condition increases with each pressurization cycle. The equilibrium pressure also increases gradually after every cycle. These behaviors are particularly evident for cycles after 40 hours. After 95 hours, the process of propane hydrates formation is considered to be roughly complete for the dissociation test to be initiated. The outlet of the vessel is then opened to atmospheric condition to allow hydrate dissociation by the depressurization mechanism.

Details of the pressure variations during the hydrate formation process can be better seen from Figure 34 with the adjusted scale. It is seen that the rapid increase in pressure, follows by a roughly exponential decrease, which is also changing as the number of pressure cycles increases. The time required to approach the equilibrium pressure also increases with each cycle.

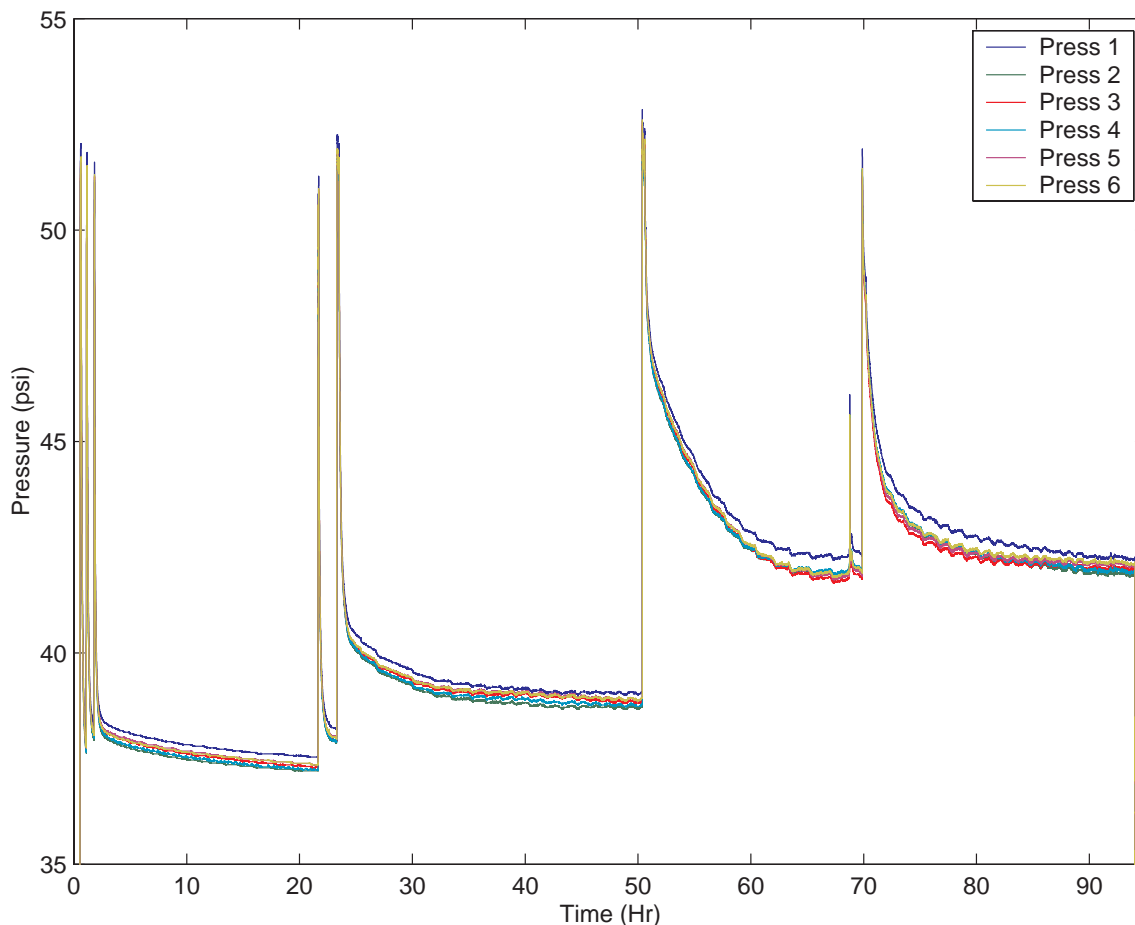


Figure 34. Time evolution of gauge pressure for hydrate formation in crushed ice.

The details of the pressure variation during propane hydrate formation process are

shown in Figure 35. This figure shows after the first propane injection, the system pressure approaches the equilibrium pressure in about half an hour and the process of hydrate formation will slow down until the regulator valve is opened up and the pressure is again increased. During the initial stages of propane hydrate formation in crushed ice, the rate at which the pressure approaches equilibrium remains roughly the same. As time increases, however, the time to equilibrium increases also the pressure approaches a larger equilibrium value, as indicated by Figures 33 and 34. The equilibrium pressure is initially about 38 psi, while after 90 hours it approaches 43 psi. That is a 5 psi increase in equilibrium pressure, while the bath temperature is kept constant at $-10\text{ }^{\circ}\text{C}$.

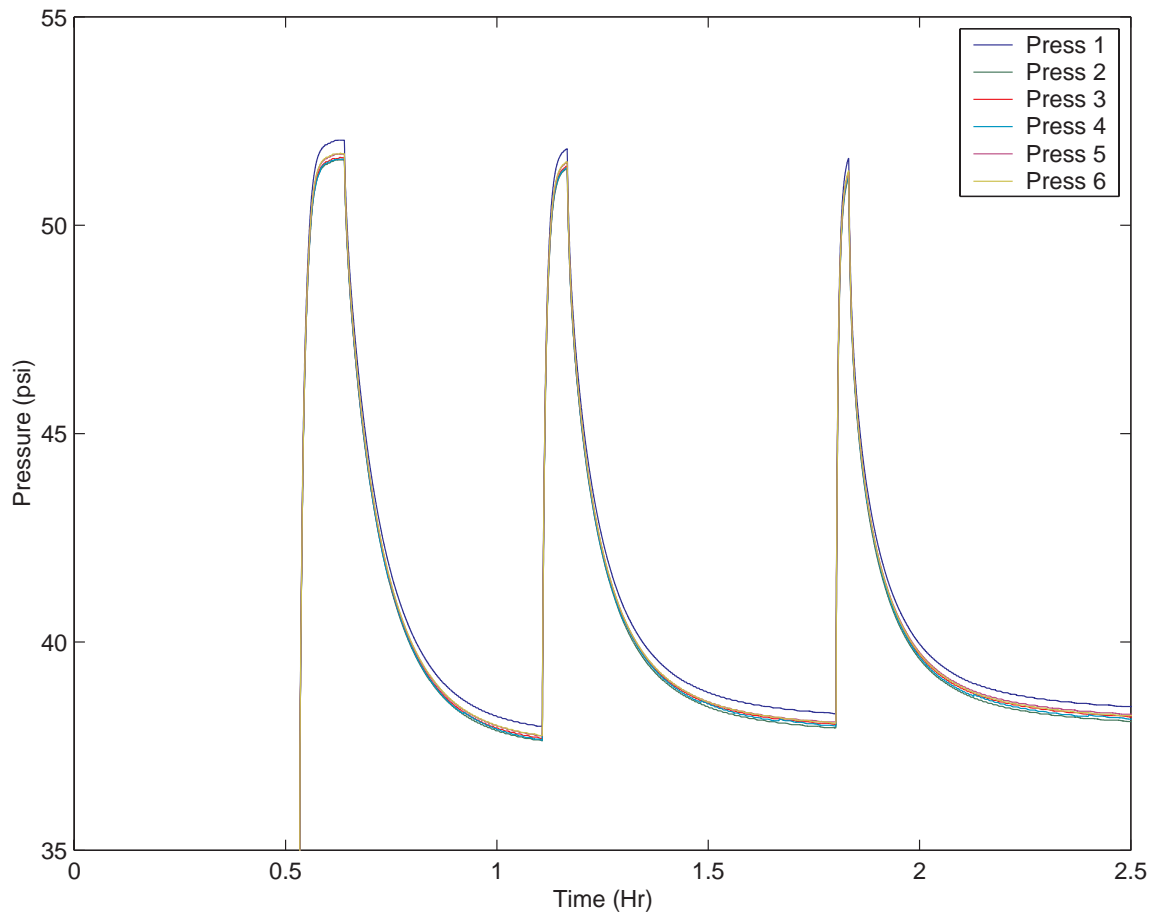


Figure 35. Details of pressure variations in the earlier stages during formation of propane hydrate in crushed ice.

The fitting of the exponential decay as given by Equation (124) to the decay of the first and third pressurization cycle are shown in Figure 36. Here the average of the six pressure sensors is used for the fitting. The corresponding k -values are also determined and is shown in this figure.

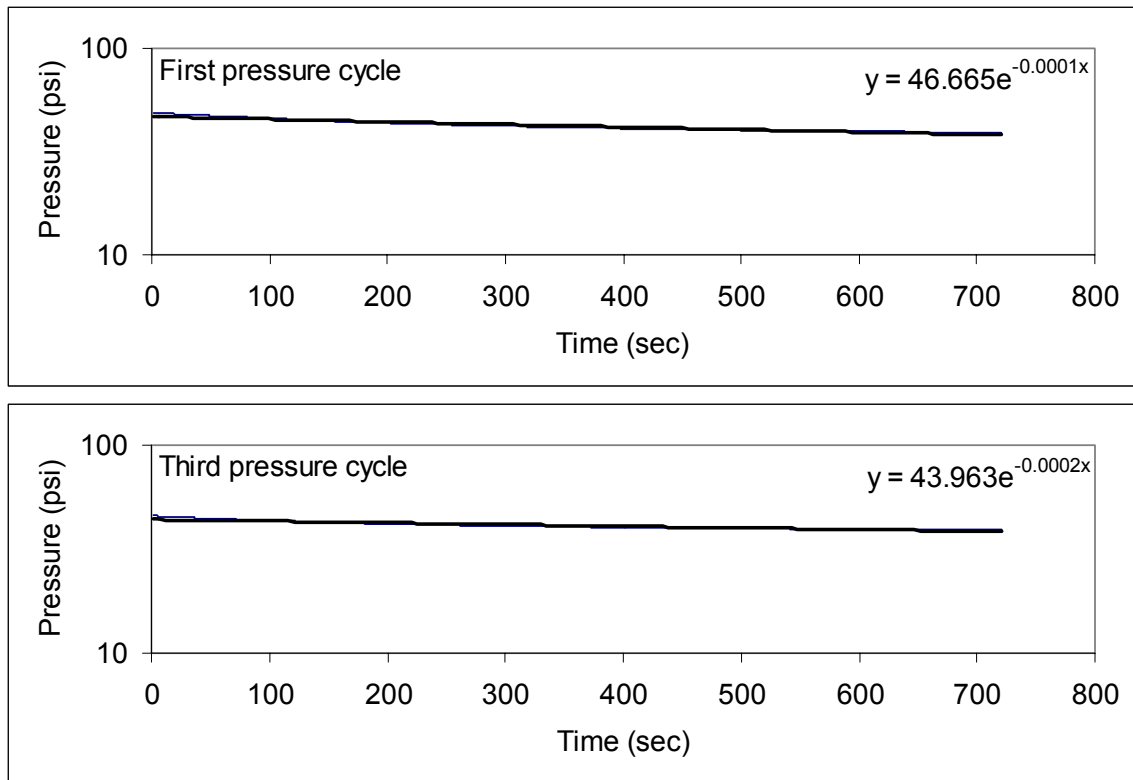


Figure 36. Exponential fit to pressure decay during hydrate formation in cycle 3 in crushed ice.

The details of the fifth pressure cycle are shown in Figure 37. It is seen that the pressure readings of sensor 1, which is closed to the inlet, is the highest. The reading of the other sensors, however, do not show a specific trend. This in part is due to accuracy of the pressure sensors. The exponential fit to the data is shown in Figure 38. The corresponding k-value for this pressure cycle is 0.0002, which is the same as the k-value for the third cycle.

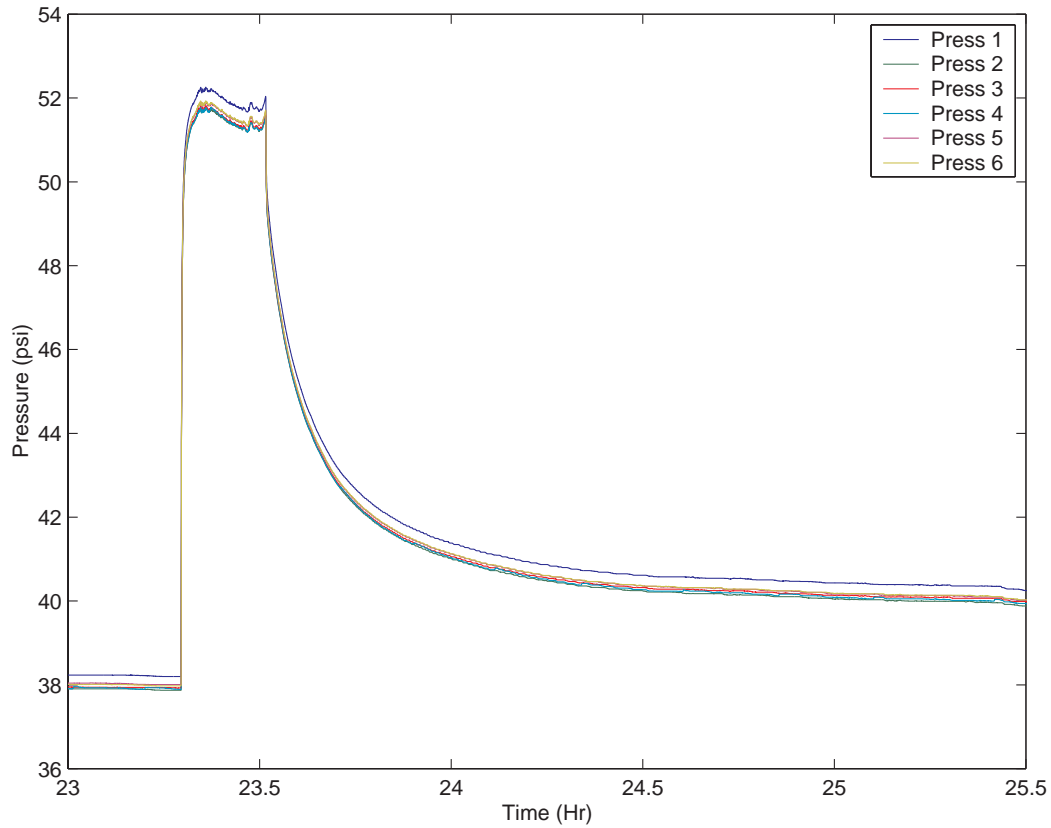


Figure 37. Details of pressure variation during the fifth pressure cycle for hydrate formation in pure crushed ice.

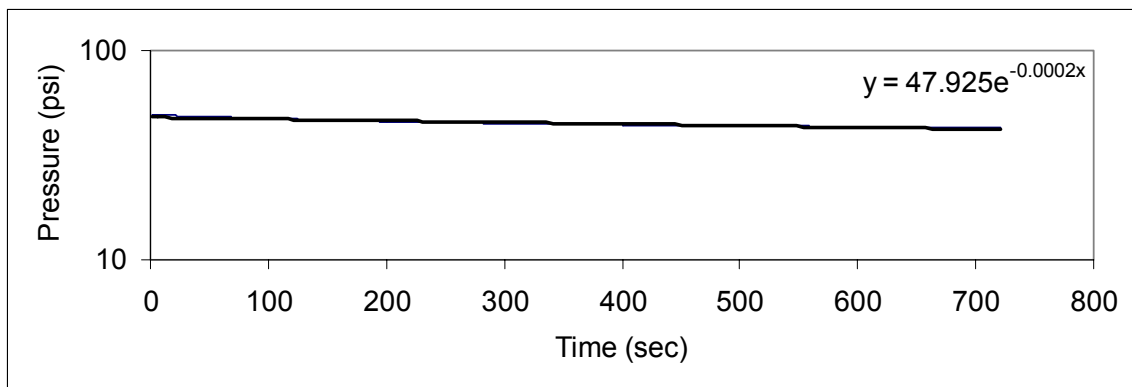


Figure 38. Exponential fit to pressure decay during hydrate formation in cycle 5 in crushed ice.

As noted in the section on the experimental setup, six pressure and temperature sensors, distributed spatially along the vessel, record the time evolution of pressure and temperature. This allows for the detection of any spatial variation of pressure and

temperature in the vessel during the hydrate formation. Enlarged segments of the pressure distribution for the fifth cycle and at latter stages of hydrate formation are shown in Figures 39 and 40. These figures exhibit a pressure distribution along the length of the vessel with a distinguishable pattern. Pressure sensor 1 shows the highest reading in both figures, the remaining sensor readings, however, do not show a specific trend. But the trend is the same in both figures. The reason for the seemingly irregular order of the sensors 2-6 reading is not quite obvious. It should be emphasized that the accuracy of the pressure transducers used in these experiments is $\pm 0.25\%$, which results in a pressure error of ± 0.1 . The differences in the pressure readings in Figures 39 and 40 are about 0.4 psi. Therefore, part of the observed deviations may be attributed to the error in pressure sensor readings. Nevertheless the persistence of these patterns in both figures suggests that the sample may have formed fractured that generates low pressure drop passages that allow the gas to reach areas near sensors in the back of sample more readily.

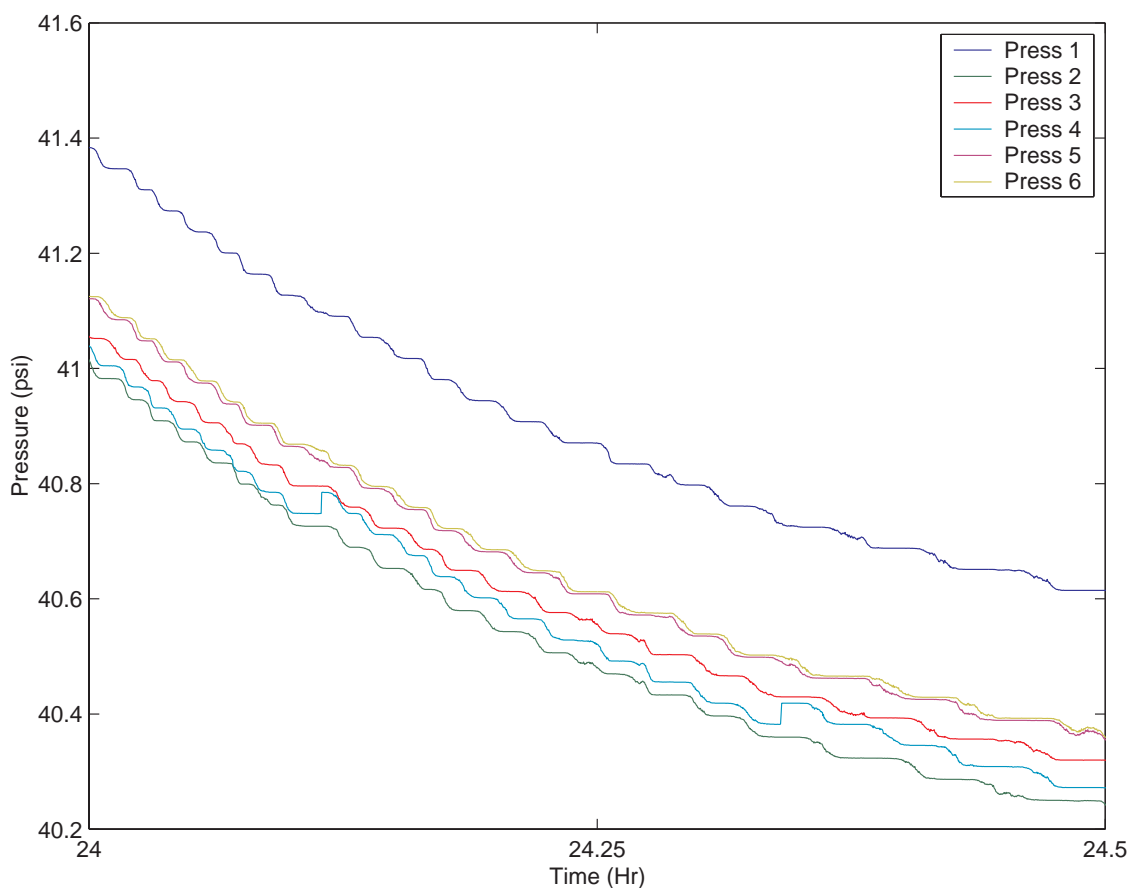


Figure 39. Spatial and temporal variations of pressure in the vessel during the fifth cycle of hydrate formation in crushed ice.

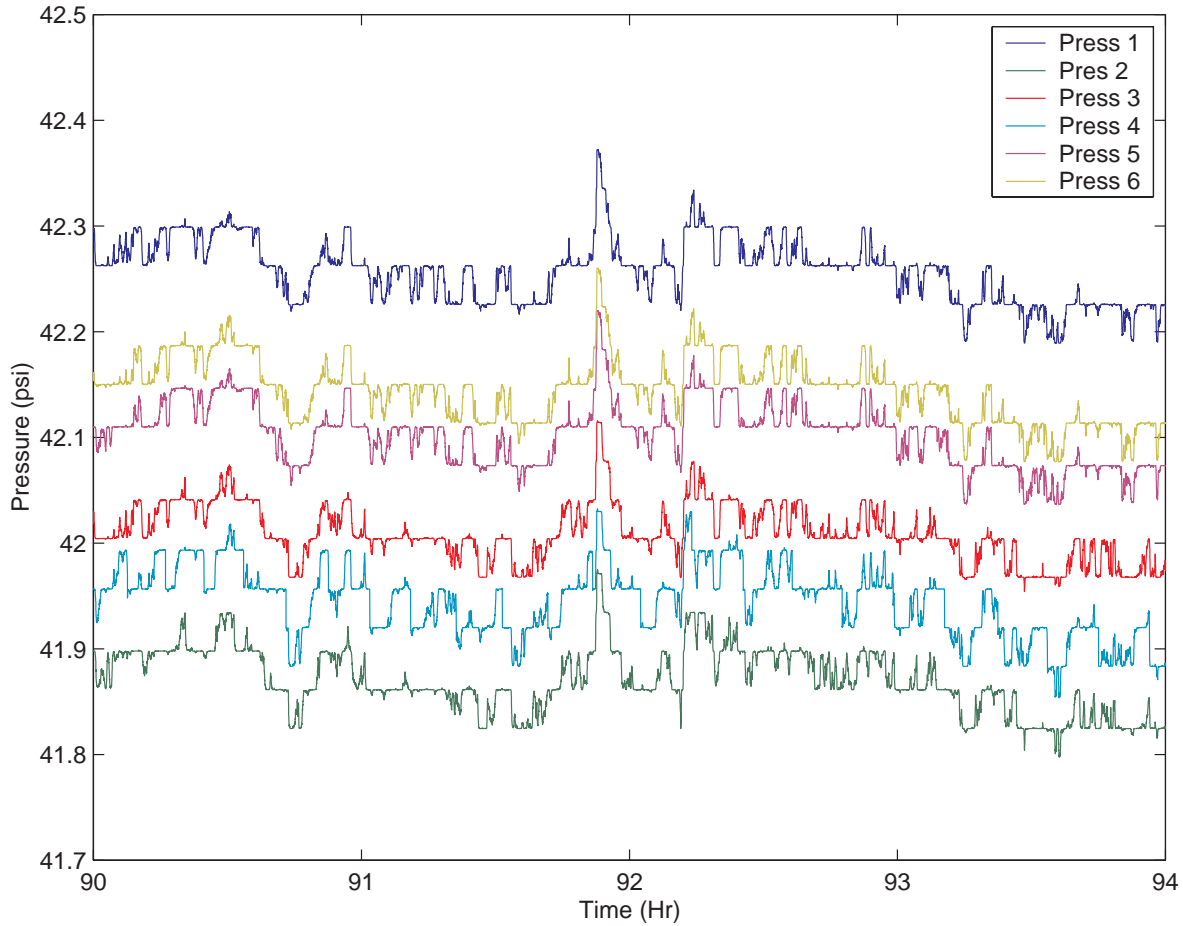


Figure 40. Spatial and temporal variations of pressure in the vessel during the latter stages of hydrate formation in crushed ice.

The time variation of temperature during the propane hydrate formation in the crushed ice is shown in Figure 41. As the propane is injected from the tank into the system, the temperature rises as the gas pressure increases. The temperature then decreases gradually with time. The increase in temperature is partially attributed to the propane gas injected into the vessel from the tank. The propane gas in the tank is at room temperature and when injected into the vessel leads to an increased temperature reading by the sensors. The increase of temperature at the earlier stages of hydrate formation is about 8°C. At the latter stages of hydrate formation, however, the increase in temperature reduces significantly. This is because the amount of propane that enters the vessel decreases, due to the decrease in available pore volumes for hydrate production.

Figure 42 shows the time histories of temperature at different locations of the vessel during the initial stages of propane hydrate formation process. It is seen that the sharp increase in temperature follows by a gradual roughly exponential decrease. Also

interestingly, spatial variations of temperatures measured by the sensors show a decreasing variation with the distance from the inlet pipe. That is, the temperature is highest at sensor 1 which is closest to the inlet, and decreases with the distance of the sensor from the inlet. There is some discrepancy with temperatures at sensors 5 and 6 in second and third cycles, which may be caused by the non-uniformity in the propane hydrate formation in the pressure vessel. It should also be emphasize that the accuracy of the temperature sensors is rather high.

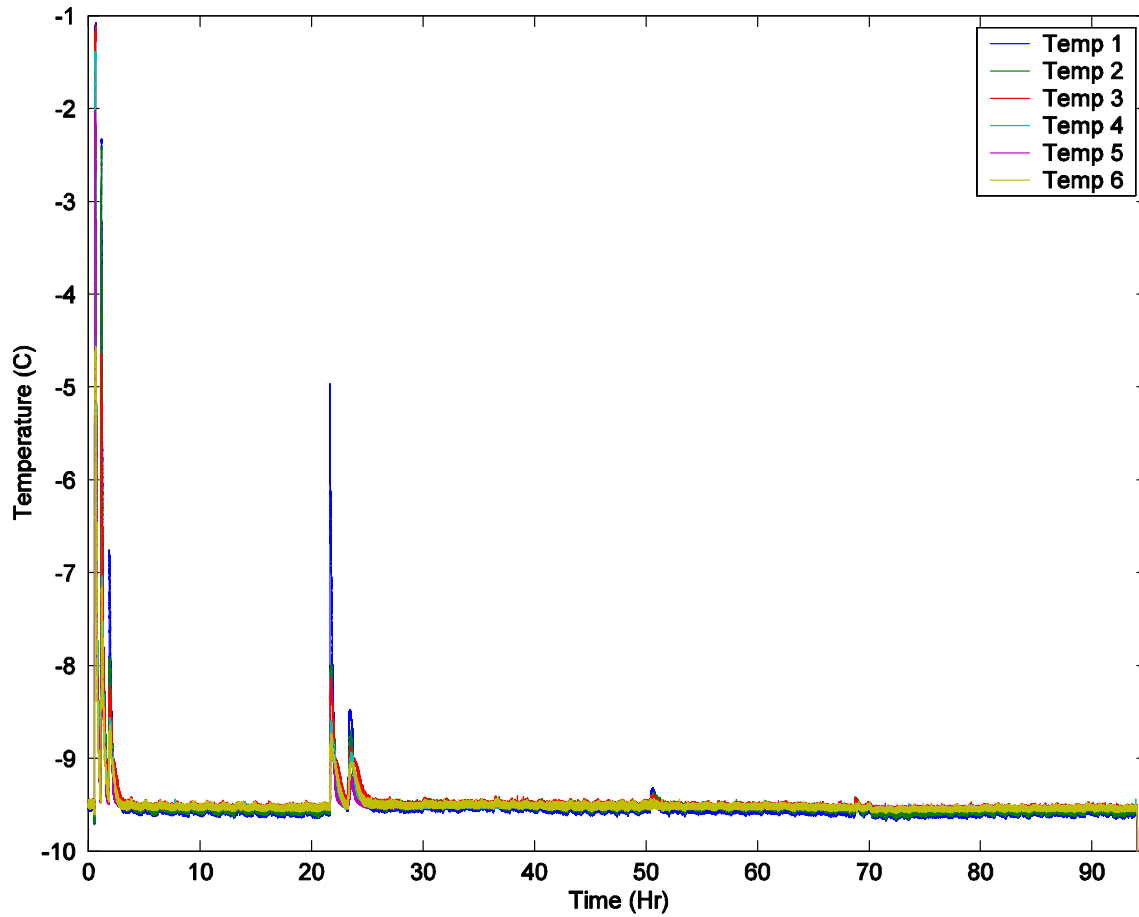


Figure 41. Time evolution of temperature during hydrate formation in crushed ice.

It is also seen from Figures 41 and 42 that the peak temperature in the subsequent pressurization cycle decreases and the decreasing trend continues as the number of cycle increases. This is in contrast with the peak pressure that remains roughly the same for different cycles. The decreasing trend of the pick temperature is mainly due to the decrease in the amount of gas injected into the vessel in the subsequent cycles.

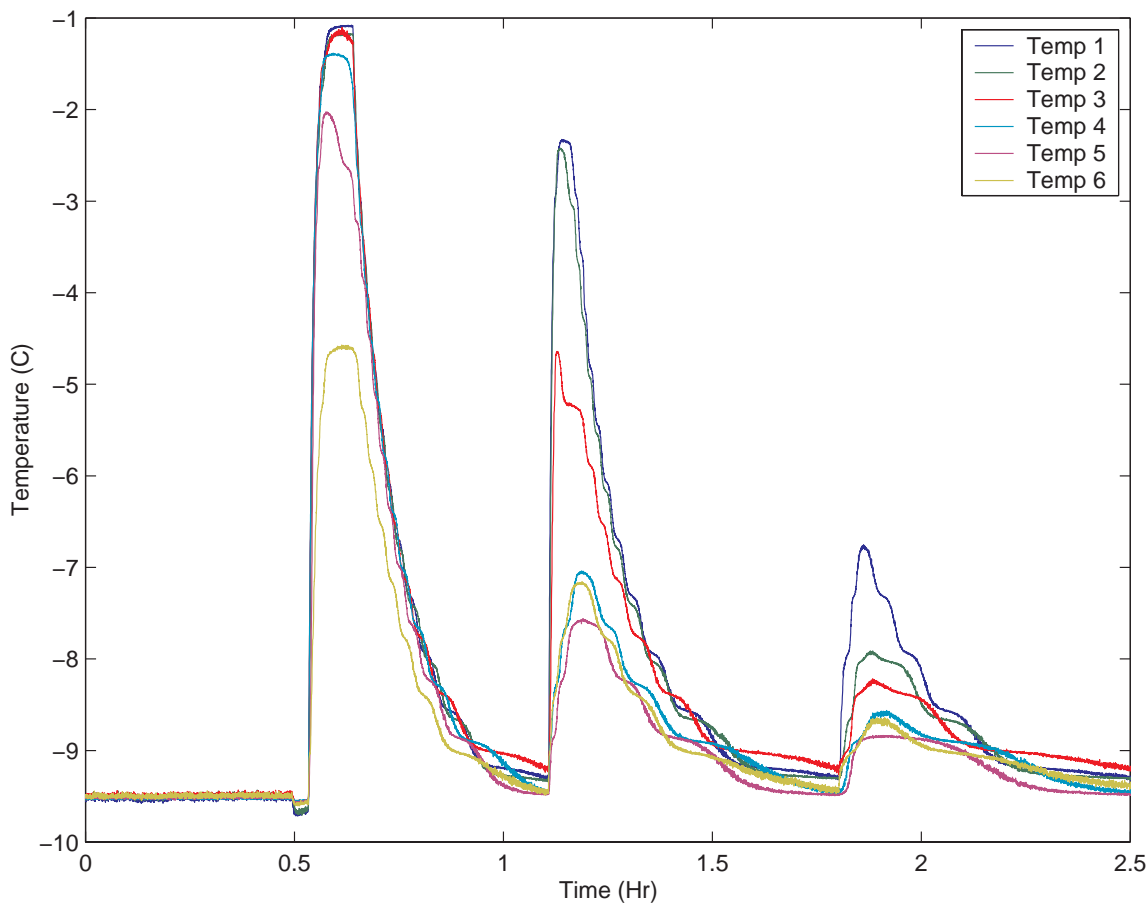


Figure 42. Details of temperature variations in the earlier stages of propane hydrate formation in crushed ice.

The amount of propane gas injected into the vessel was also continuously measured and the results are shown in Figure 43. The unit of the volume flow rate in this figure is standard liters per minute (sLPM). As noted before, the amount of mass entering the pressure vessel typically decreases in volume at the latter stages of hydrate formation process. The total amount of propane that was injected into the pressure vessel for this experiment was 8.4 L of propane.

Figure 44 shows the variations of pressure, temperature and volumetric flow rate during the hydrate formation in one graph. It is seen that the rise of the temperature and pressure coincide with those of injection of propane into the vessel. It is also seen that the peak pressure remains the same, while the peak temperature and mass flow decreasing with the number of pressurization cycle.

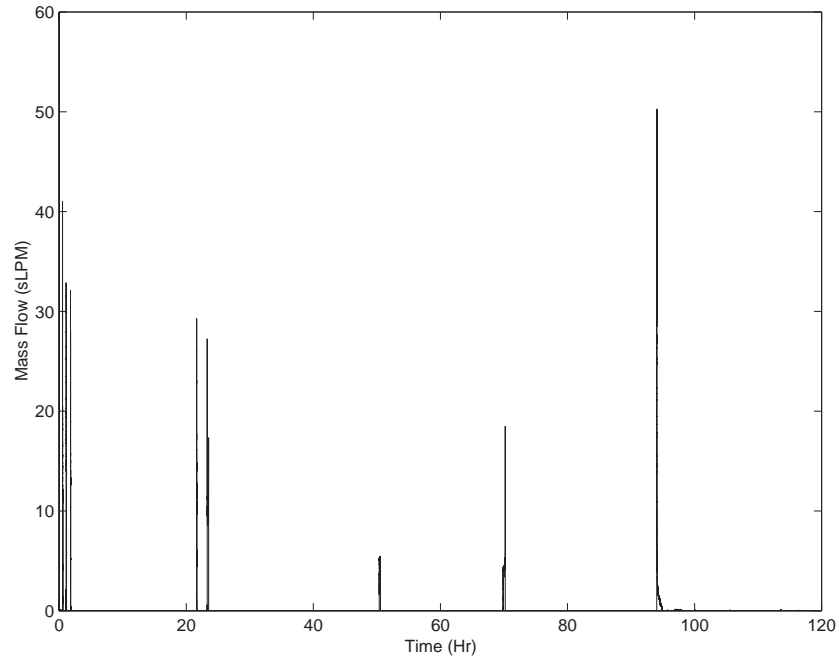


Figure 43. Mass Flow time evolutions for hydrate formation in crushed ice.

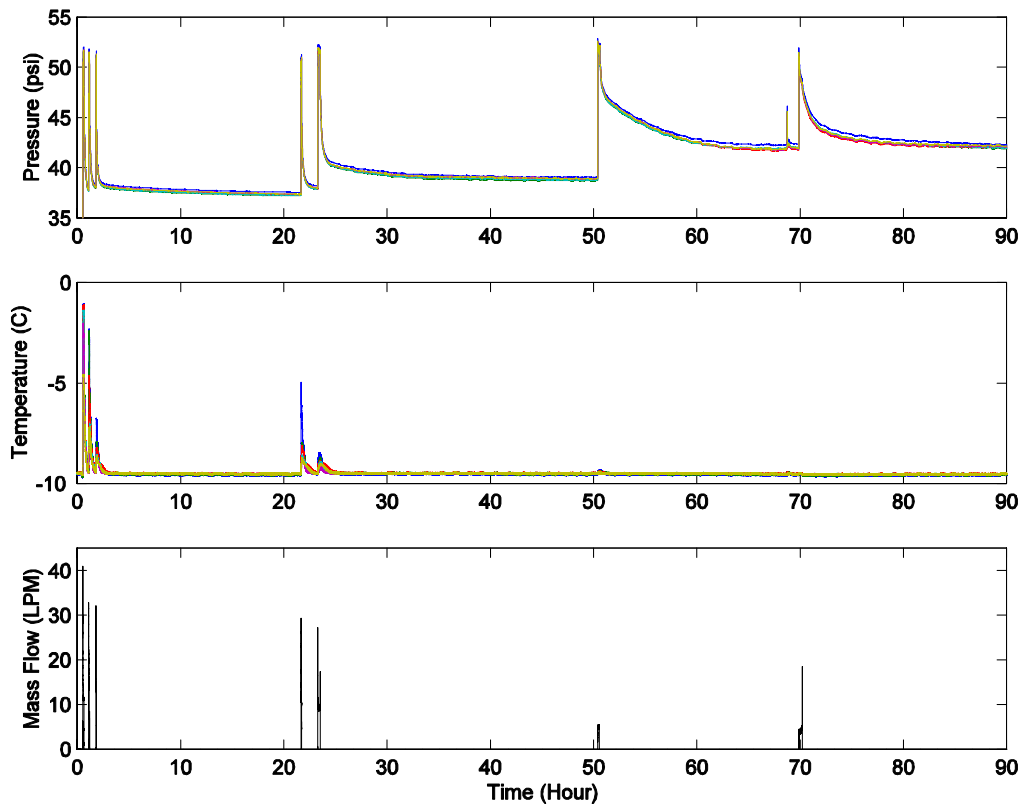


Figure 44. Time evolutions of pressure, temperature and flow rate for propane hydrate formation in crushed ice.

Propane Hydrate Formation in 75% Crushed ice and 25% Glass Bead

Propane hydrate formation and dissociation experiments were performed for a mixture of 75% crushed ice and 25% glass bead. The mixture was used to simulate hydrate formation and dissociation in unconsolidated sediments. The glass beads had a mean diameter of 100 μm and were nearly spherical. The crushed ice was flick like with a width of about 2 mm. The crushed ice and glass beads were mixed thoroughly before being packed uniformly into the vessel. The data was collected following the same procedure for the pure crushed ice outlined previously. The time evolution of the pressure during the hydrate formation is shown in Figure 45.

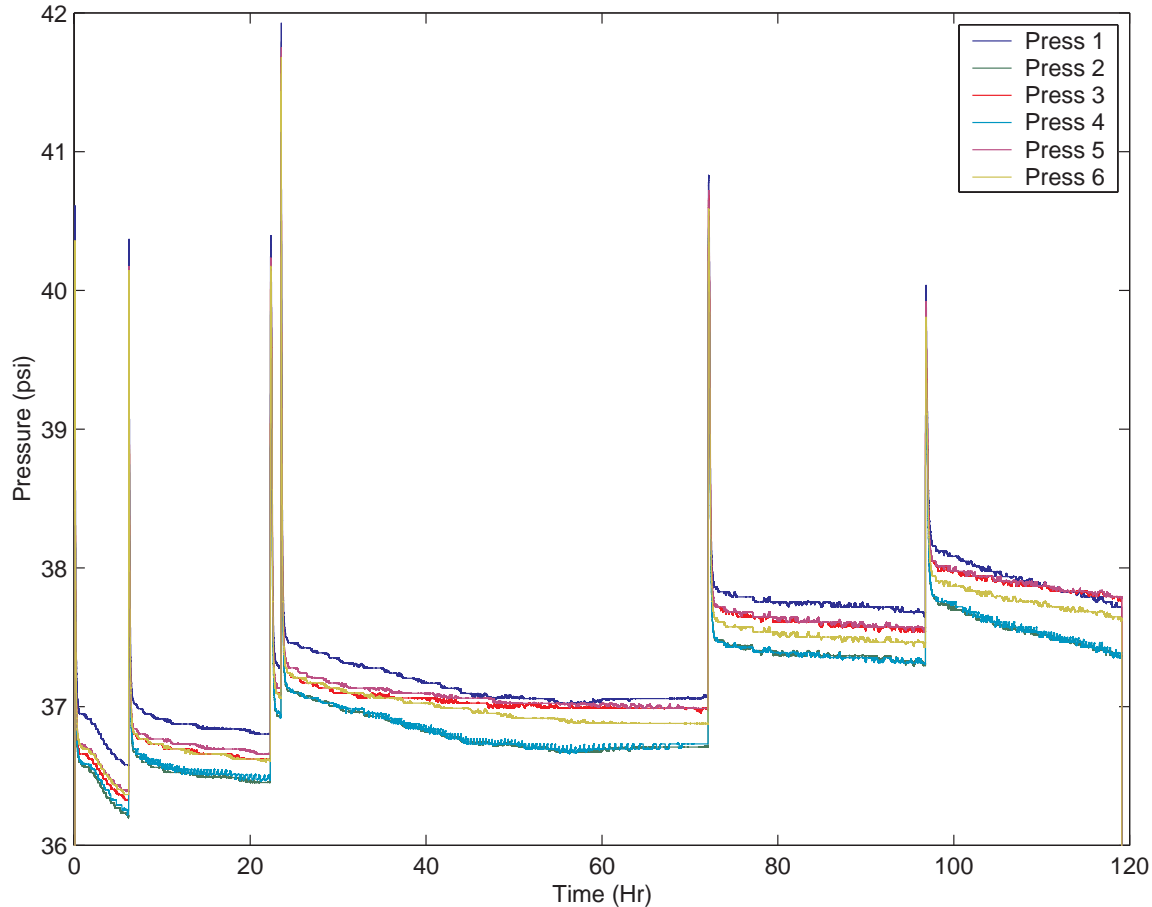


Figure 45. Time evolution of pressure during hydrate formation in the 75% crushed ice-25% glass beads mixtures.

The trends of variation of pressure in Figure 45 are similar to those of Figure 33 for the pure crushed ice sample. There is an exponential decay after the sharp increase in the pressure after each injection. A detailed view of the first pressure cycle for the 25% glass beads mixture is shown in Figure 46. When compared to Figure 35, the time for the cycle to approach the equilibrium pressure is approximately the same.

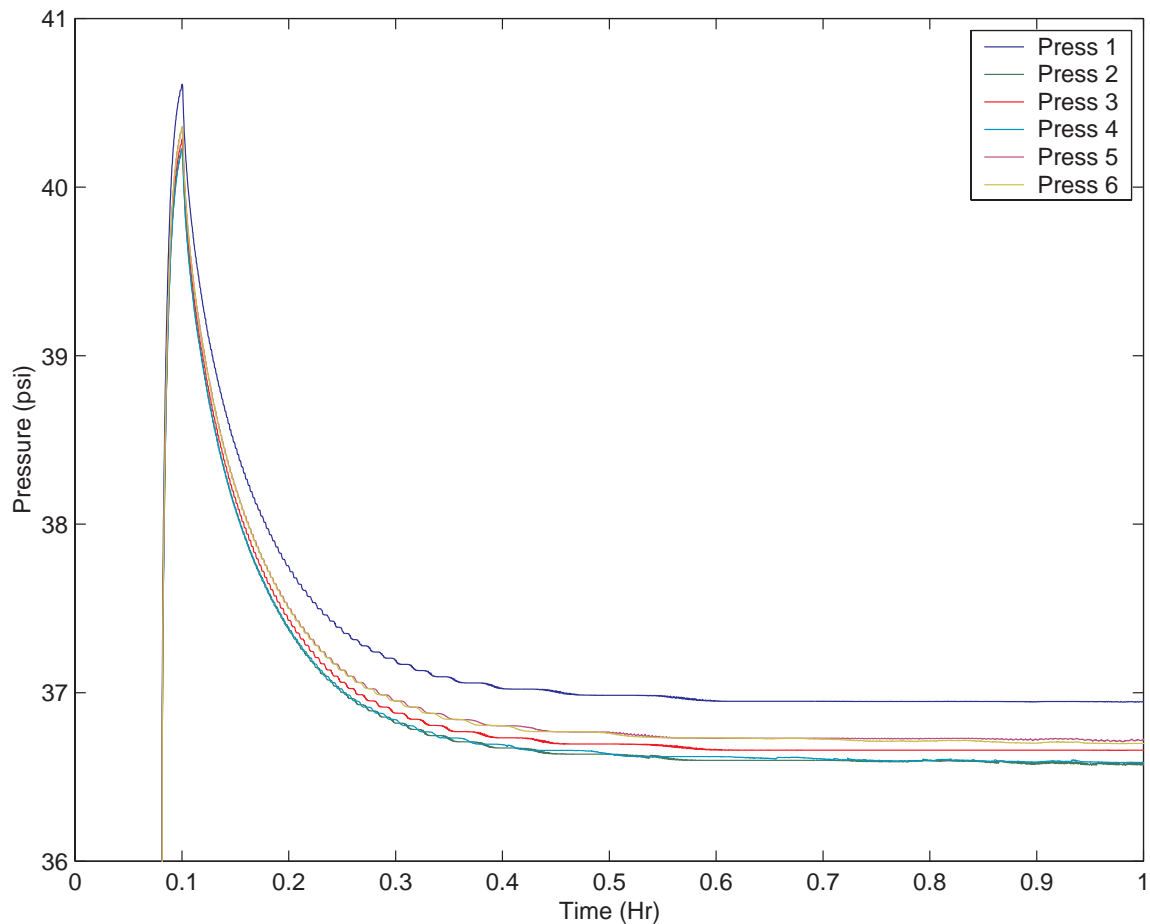


Figure 46. Time evolution of pressure during propane hydrate formation in the first cycle in the 75% crushed ice-25% glass beads mixture sample.

The exponential fit to the pressure variation in the first cycle of pressurization for the 75% crushed ice-25% glass beads mixture is shown in Figure 47. The corresponding k -value is found to be 9×10^{-5} which is smaller than that of the crushed ice. That is, the mixture with 25% beads will reach equilibrium in a longer time period.

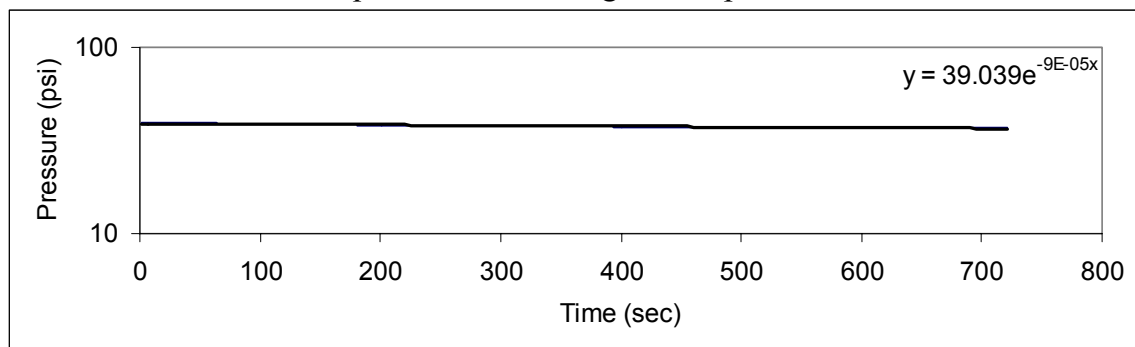


Figure 47. Exponential fit to pressure decay during hydrate formation in cycle 1 in the 75% crushed ice-25% glass beads mixture sample.

Time variation of temperature for the mixture of 75% crushed ice and 25% glass beads mixture is shown in Figure 48. The trend of temperature variation is similar to that of Figure 41 for pure crushed ice. The temperature appears to increase as propane is injected into the vessel and that is followed by an exponential decay. In the first cycle, the increase is less than that of the crushed ice. This is due to the fact that the mixture was subject to a lower gas pressure and the amount of gas injection was smaller. In contrast the case of pure crushed ice, however, the amount of temperature rise after each subsequent gas injection is relatively large compared to the temperature rise in the first cycle.

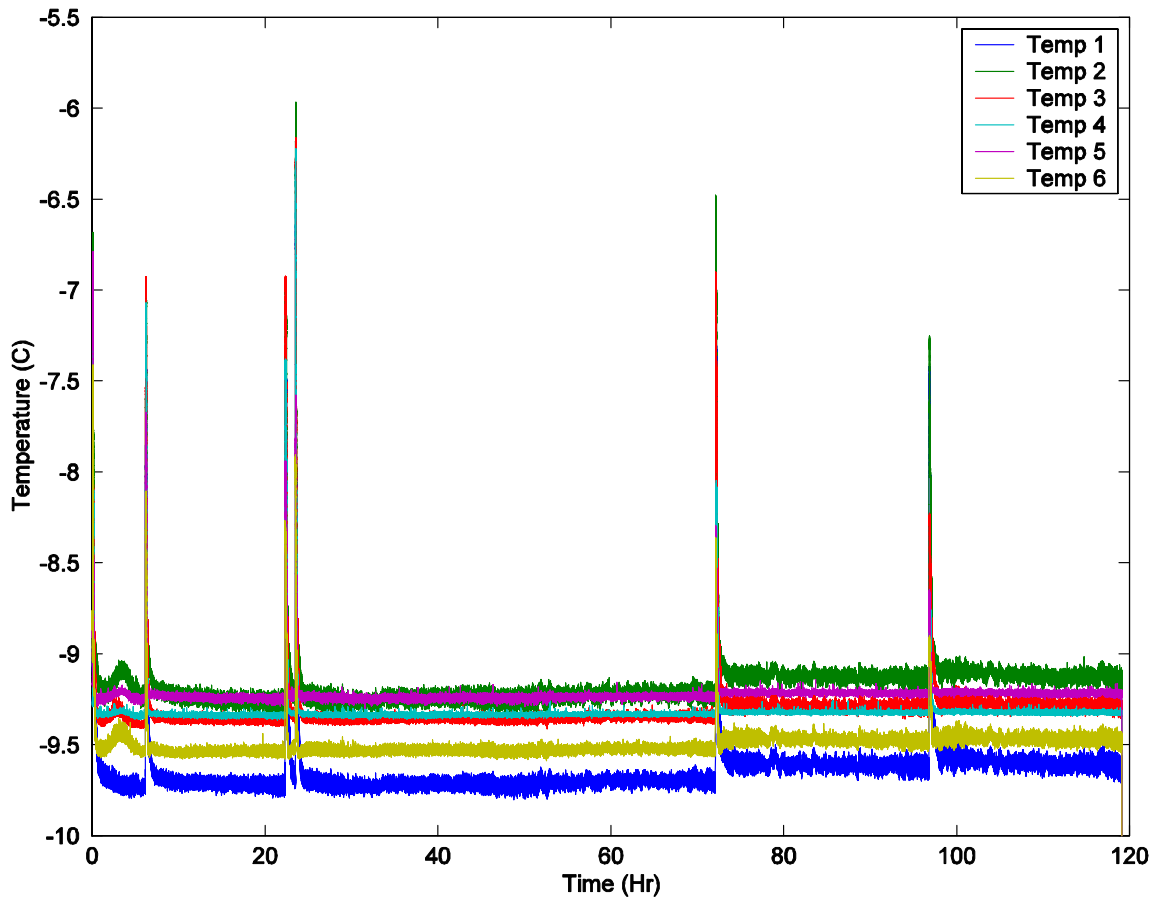


Figure 48. Time evolution of temperature during hydrate formation for the 75% crushed ice-25% glass beads mixture.

The cumulative volumetric amount of propane injected into the system is shown in Figure 49. This figure shows that the times for sharp changes in pressure and temperature coincide with the injection time. In the case of 75% crushed ice-25% glass beads sample, the total amount of propane injected was 3.87L, while for the pure crushed a total 8.37L of propane injected into the vessel.

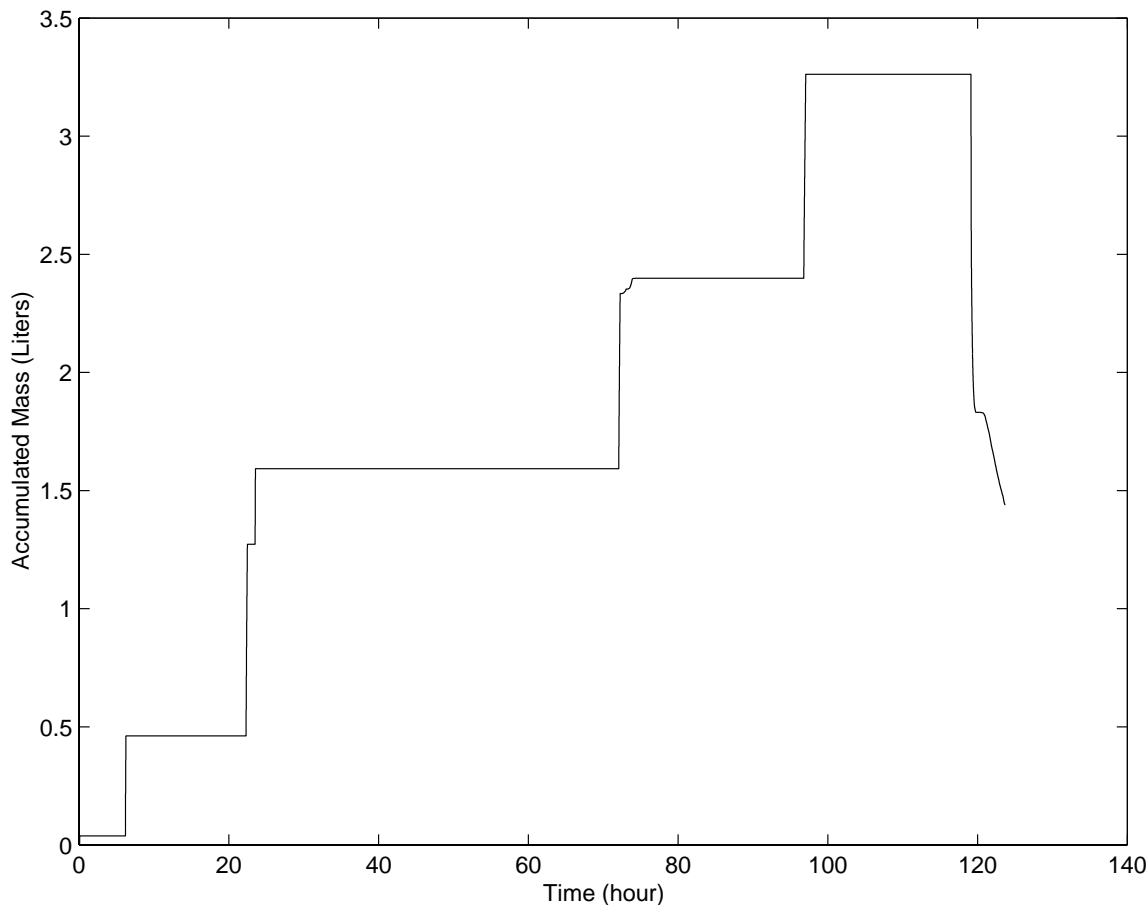


Figure 49. Cumulative volume of propane injection during hydrate formation for the 75% crushed ice-25% glass beads mixture.

Experimental Results for Hydrate Dissociation

The dissociation experiments were performed after the propane hydrate was formed. The dissociation process was initiated by opening the inlet/outlet valve and exposing the vessel to atmospheric pressure. The dissociation pressure and temperature data were obtained at high sampling rates for duration of two minutes after opening of the valve and initiation of depressurization process. The high sampling rate provided greater resolution of the variations for all parameters during dissociation. In this section, pressure, temperature and volumetric flow data are presented and discussed.

Hydrate Dissociation for Pure Crushed Ice Sample

As noted before, the depressurization was initiated after the hydrate formation, which typically took about five days. Figure 50 shows the variations of pressure during the

dissociation process for the pure crushed ice media. As the system is opened to the atmosphere, the propane hydrate dissociates rapidly and the vessel pressure decreases exponentially. This figure shows that approximately 1 hour is required for the vessel pressure to reach atmospheric pressure. At the initial stages of depressurization, Figure 50 shows that there are some small amplitude fluctuations in the pressure field. These fluctuations are attributed to the interaction of high speed gas flow and outlet piping and valve systems.

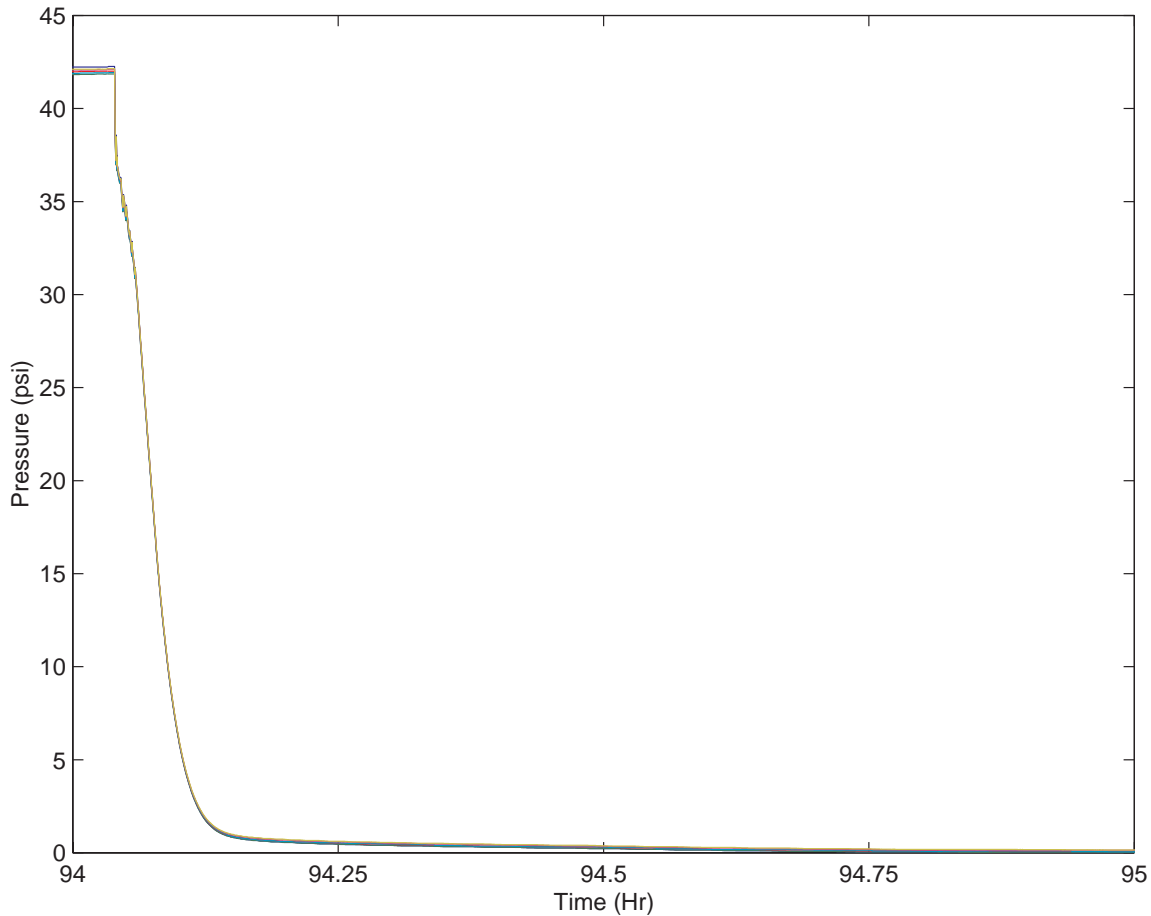


Figure 50. Time evolution of pressure for hydrate dissociation in crushed ice sample.

As described in the modeling section, the rate of hydrate dissociation depends on the pressure difference between the hydrate equilibrium pressure and the local gas pressure. Here the simplified version of Kim-Bishnoi model is used. Accordingly, the pressure decay is given by Equation (127). The decay rate for the pure ice sediment has been obtained by averaging the six sensors response during the depressurization. The data is then plotted on a semi log graph, where an exponential curve is fitted to the data and model parameters are evaluated. Figure 50 shows the averaged pressure data during the dissociation, and the exponential

curve fit, and the corresponding k_3 -value. (Note that the second term of Equation (127), which is assumed to be small and is neglect. The model shows a good agreement with the experimental data decay rate. Figure 50 also shows a k_3 -value of 0.011, which is much larger than the k -values for the hydrate formation.

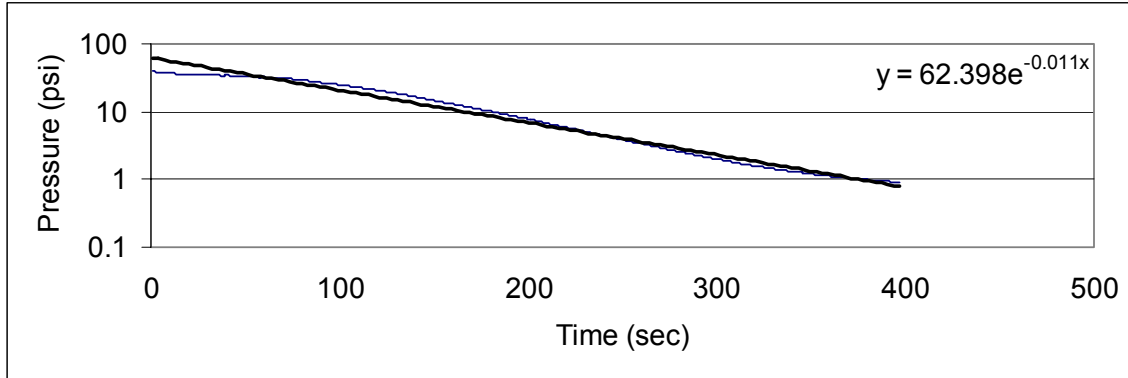


Figure 50. Comparison of the experimental data with an exponential fit for hydrate dissociation in pure crushed ice sample.

Figure 51 shows the first 15 minutes of the dissociation process. The pressure reduces to approximately 1 psi in 6 minutes after the valve is opened. This indicates that the hydrate dissociation is a comparatively a rapid process, compared to the 5 days needed for the formation.

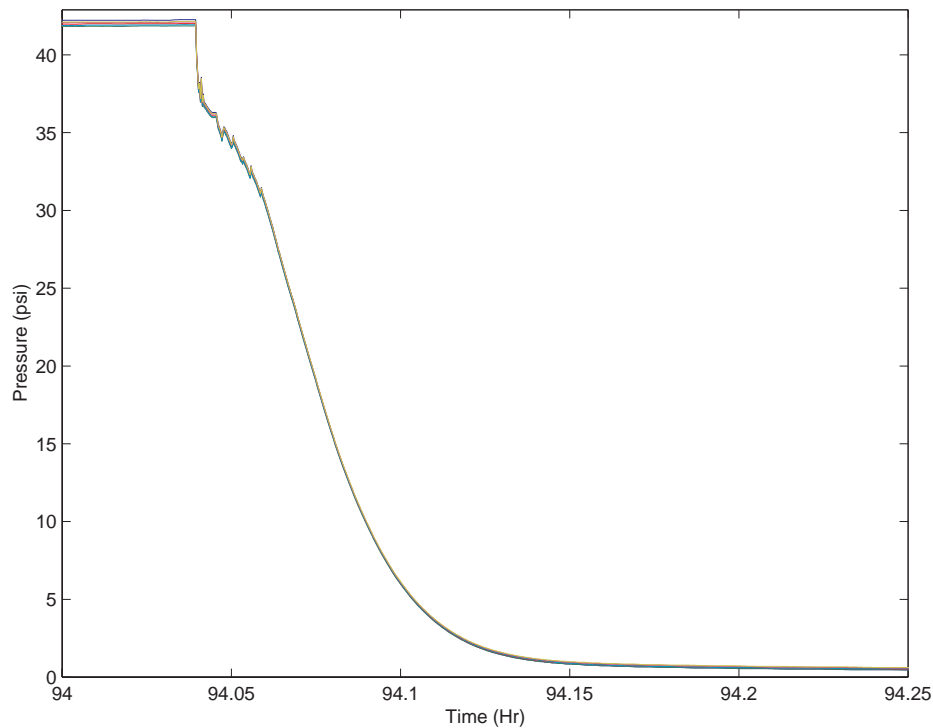


Figure 51. Details of time evolution of pressure for hydrate dissociation in pure crushed ice sample.

The time variation of temperature in the vessel for the propane dissociation in pure crushed ice sample is shown in Figure 52. The temperature drops sharply to -40°C when the dissociation is initiated as heat is absorbed by the process and gas pressure is reduced due to the gas leaving the vessel. The temperature is then gradually increases to the bath temperature. The sample temperature remains below the bath temperature for a long period of time (about 3 hours) compared to the pressure decay time which is about fraction of an hour. Temperature reading of sensor 1 shows that the temperature increases at a higher rate compared to the other sensors. The other sensors, however, do not show a specific order and their order also changes with times until the bath temperature is reached.

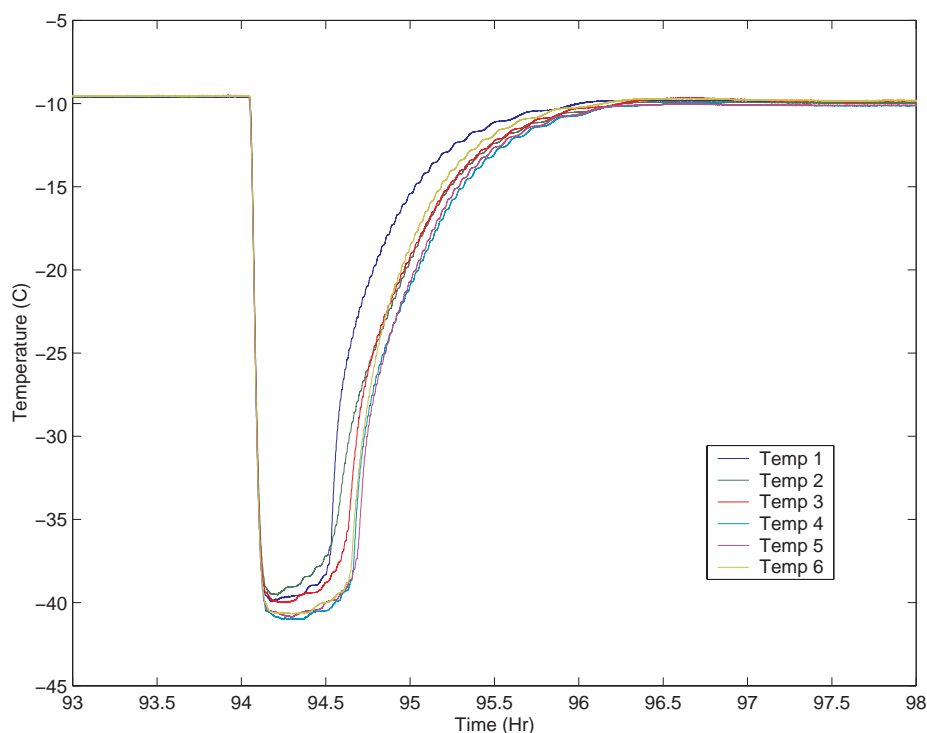


Figure 52. Time evolution of temperature for hydrate dissociation in the crushed ice sample.

The volumetric flow rate exiting the system is shown in Figure 53. The flow rate follows the same trend as the pressure, with 95% of the propane hydrates being dissociated and exited the system in about 15 minutes after the initiation of depressurization. Some fluctuations in the flow rate in the first 80 seconds after the depressurization is initiated is noticed in Figure 53. The initial fluctuations in the flow rate are attributed to the system piping.

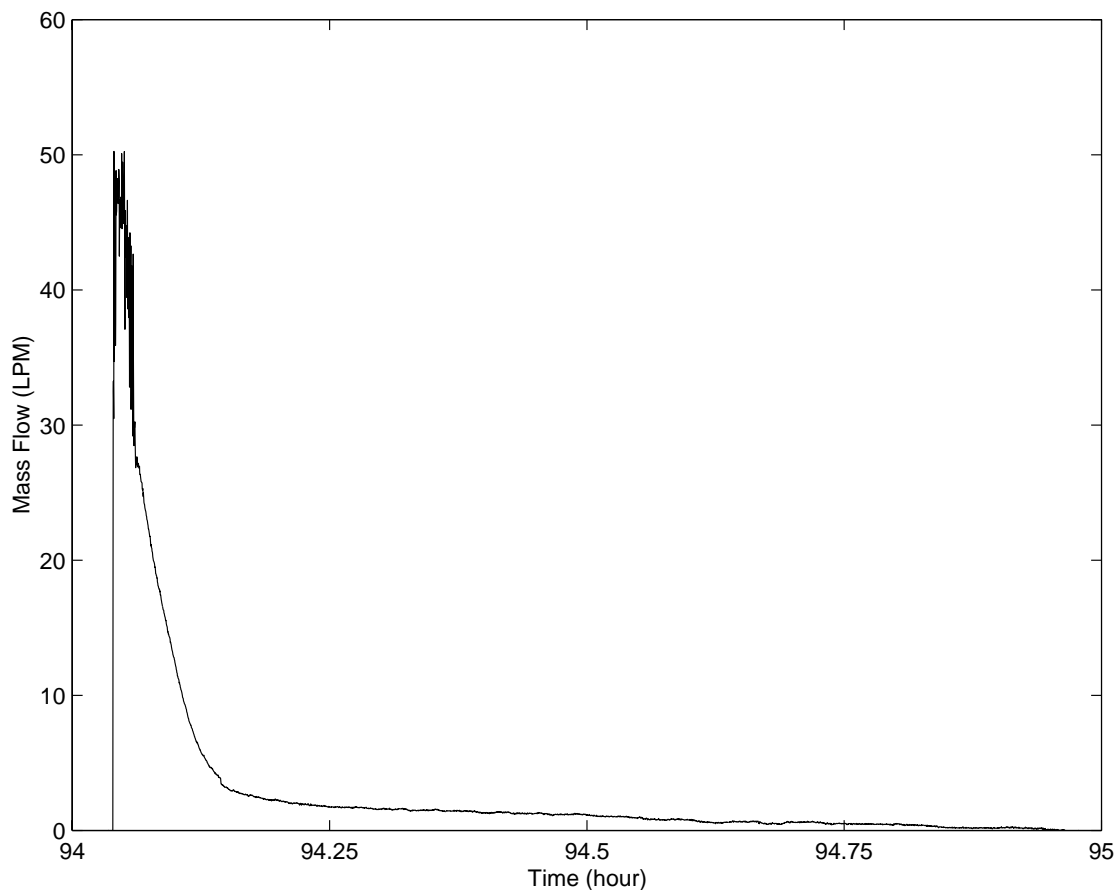


Figure 53. Time evolution of mass flow for hydrate dissociation in crushed ice sample.

Variations of vessel pressure and volumetric flow rate on an expanded scale are shown in Figure 54. It is seen that the decay patterns of pressure and volume flow rate follow the same trends. In particular, in the earlier stages both pressure and flow rate show some small scale oscillation, which is believed to be due to the high speed gas flow in the outlet plumbing. After the initial stages, the decay of the vessel pressure and volume flow rate decay follow a smooth exponential decay.

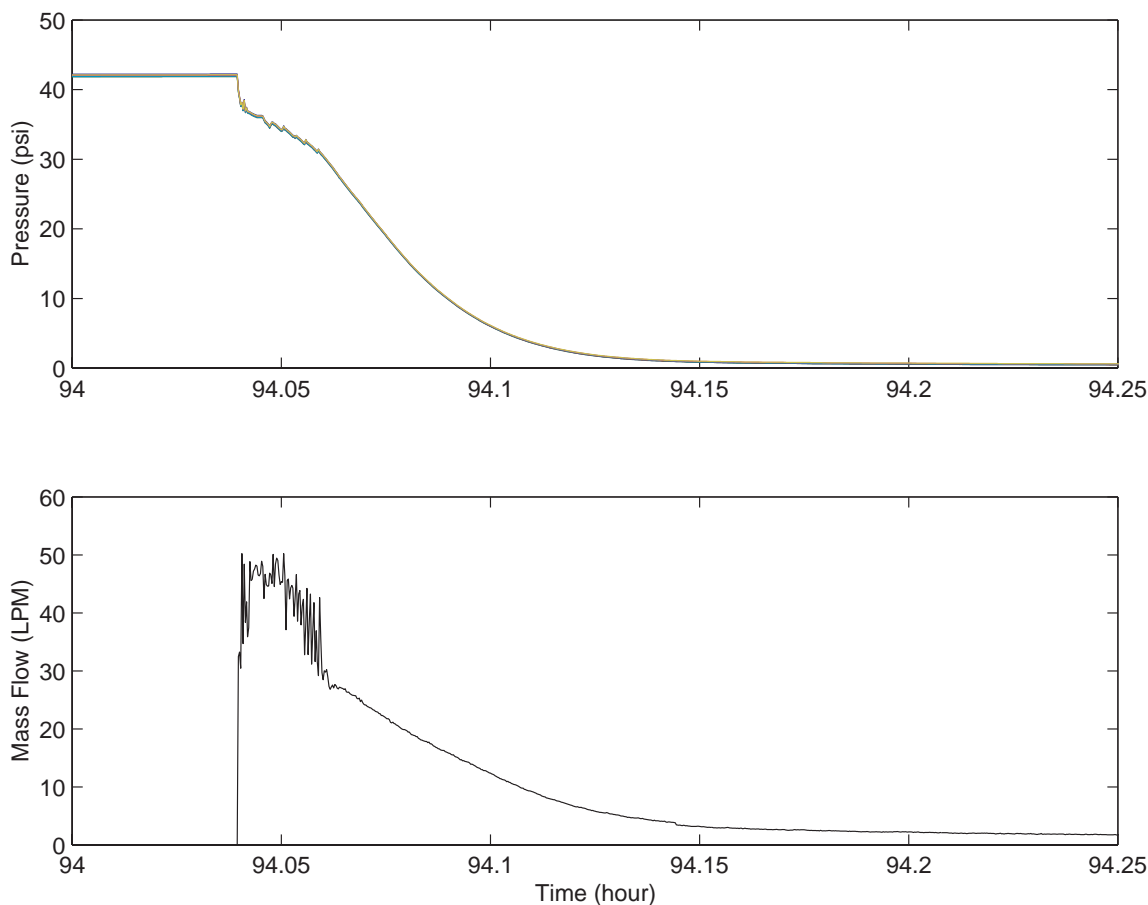


Figure 54. Time evolutions of pressure and mass flow rate for hydrate dissociation in The crushed ice sample.

Hydrate Dissociation in 75% Crushed Ice 25%-Glass Beads Mixtures

The experimental data for the propane hydrate dissociation for the mixture of 75% crushed ice and 25% glass beads are described in this section. Figure 55 shows the time evolution of the pressure. The rapid exponential decay of pressure is similar to that of the pure ice sample. However, the pressure for mixture of ice and glass beads approaches atmospheric condition in approximately half the time compared to the pure ice sample shown in Figure 50.

The experimental data for the pressure variation in the mixture sample is plotted in a semi-log scale in Figure 56 and is fitted to an exponential curve. This figure shows that the exponential decay fits the data very well. The corresponding decay rate is $k_3=0.0177$, which is higher than the decay rate of $k_3=0.011$ for crushed ice. It should also be emphasized that

the initial pressure for the pure crush ice case was 42 psi, while for the mixture case was about 38 psi.

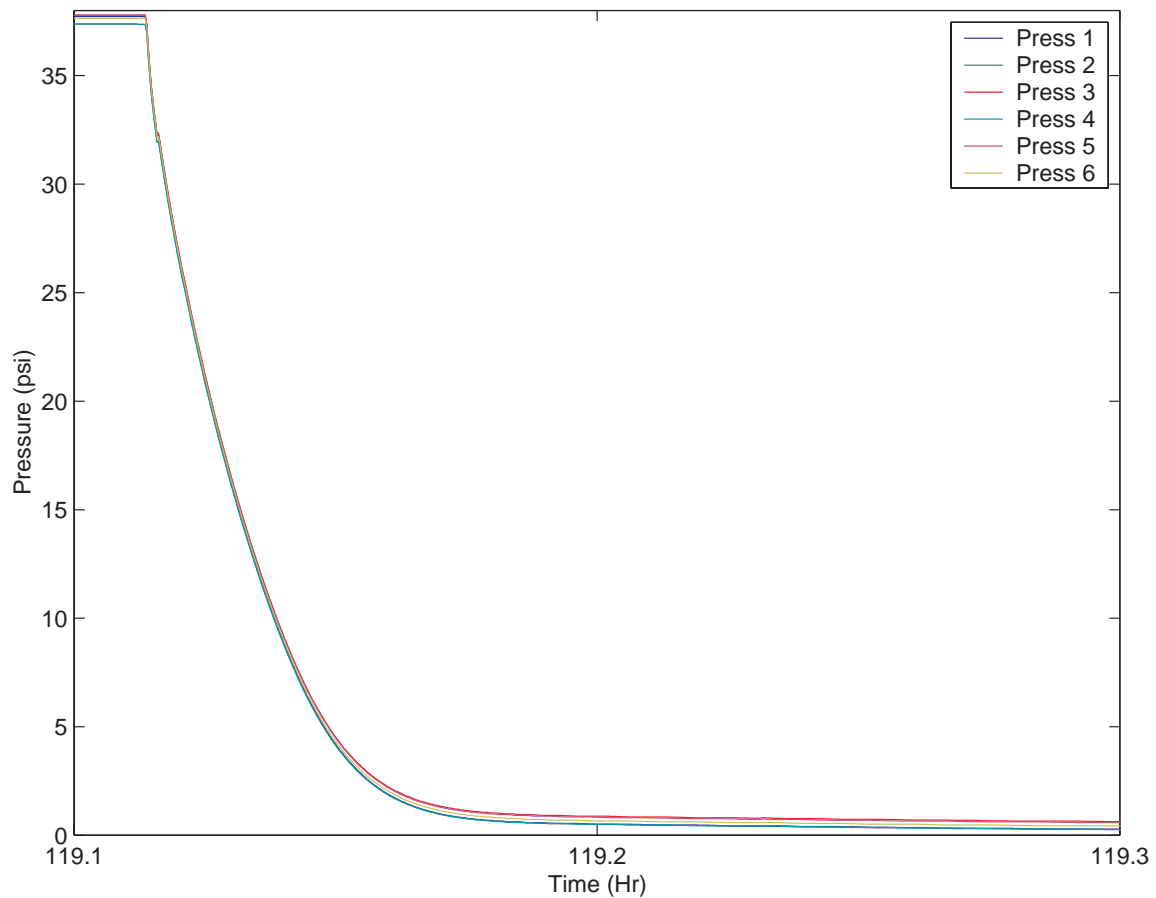


Figure 55. Time evolution of pressure for hydrate dissociation for the mixture of 75% crushed ice -25% glass beads sample.

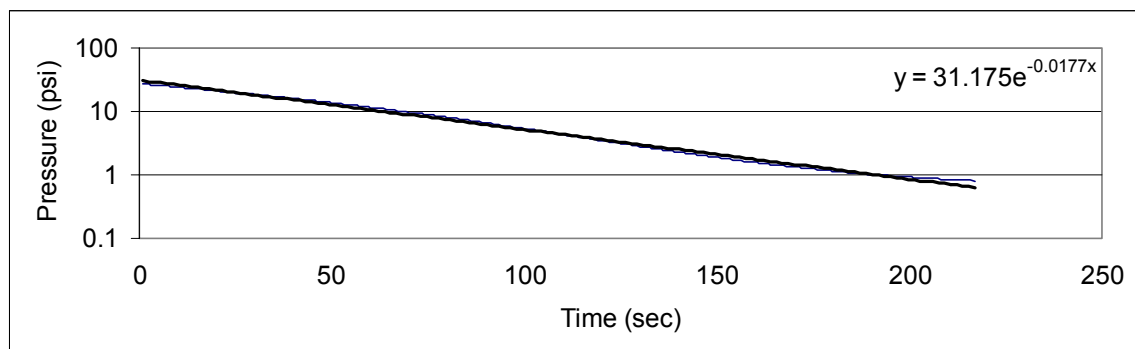


Figure 56. Comparison of the experimental data with an exponential fit for hydrate dissociation in mixture of crushed ice-glass beads sample.

Figure 57 compares the experimental data with the exponential curve fit. It is seen that the exponential decay provides for a reasonable representation of the pressure variation during the dissociation process.

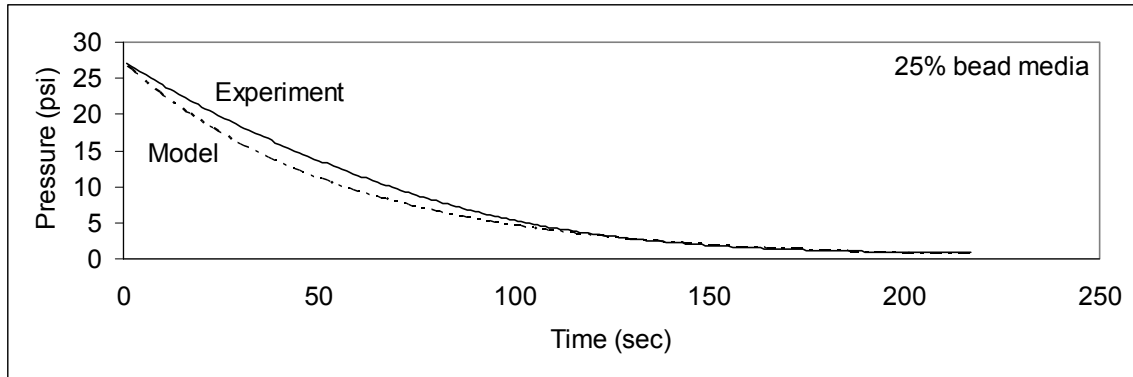


Figure 57. Comparison of the experimental data with the exponential fit for hydrate dissociation in the mixture of crushed ice-glass beads sample.

The time variations of temperature during the propane hydrate dissociation for the sample with 25% glass beads is shown in Figure 58. The general features of the temperature variation is similar those of Figure 52 for the pure crushed ice sample. The temperature drops rapidly from -9°C to about -35°C as the depressurization begins. The temperature then increases gradually and reaches the bath temperature in about 1.5 hours.

Figure 59 compares the temperature variations during the propane hydrate dissociation in pure crushed ice sample with the sample with 25% glass beads for first two hours. While the general features are comparable, there are certain differences. The temperature in the pure ice sample stays at -40°C for approximately 20 to 30 minutes before rising. The temperature in the sample with 25% glass remains at -38°C for about 10 to 12 minutes. One reason for the difference in behavior may be attributed to the fact that the crushed ice sample was prepared at higher pressure and contains larger amount of hydrate. The sample with 25% beads, however, was prepared at lower gas pressure and contains comparatively less hydrate. Thus, during the dissociation process the crushed ice sample maintains its lower temperature associated with the hydrate dissociation for a longer period.

Figures 58 and 59 show that the spatial distribution of the temperature in the vessel with 25% glass beads as recorded by the temperature sensors is different from that of the pure crushed ice sample. This observation further indicates that the flow and heat transfer in sample does not follow a simple trend. It is conjectured that the sample forms cracks and fracture that significantly affect the spatial distribution of pressure and temperature in the vessel. The spatial order of the temperature also appears to change in time.

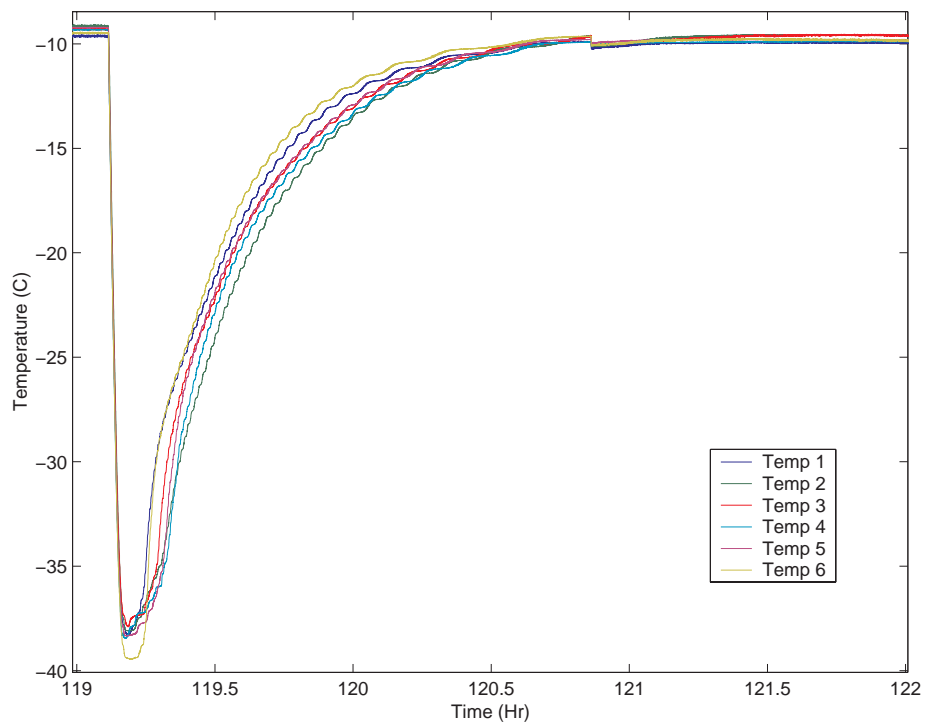


Figure 58. Time evolution of temperature for propane hydrate dissociation in the sample with 25% glass beads.

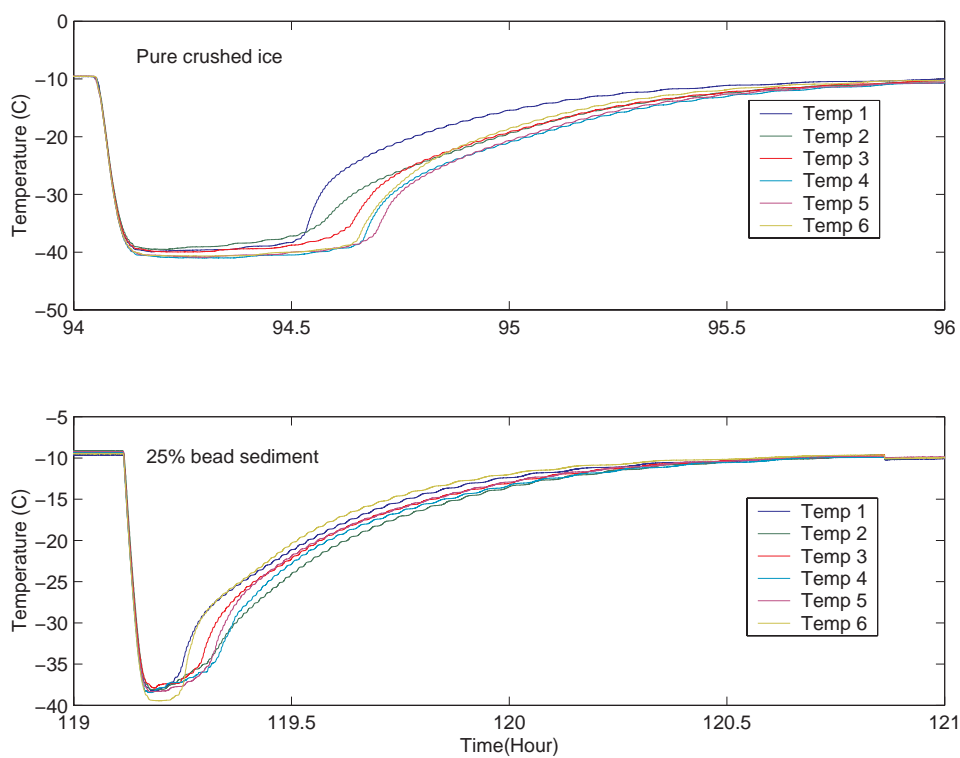


Figure 59. Comparison of time evolution of temperature during hydrate dissociation.

Figure 60 shows the volume flow rate during the propane hydrate dissociation in the sample with 25% glass beads. It is seen that the flow rate decreases sharply with time, and in about 6 minutes, 95% of the mass leaves the vessel. Comparing with the pure crushed ice case, the sample with 25% glass beads requires half as much time to reach to the limit of negligible flow rate. As noted before, the amount of propane injected into the vessel for the sample with 25% glass beads was about 3.9 L which is less than half of that for the pure crushed ice case.

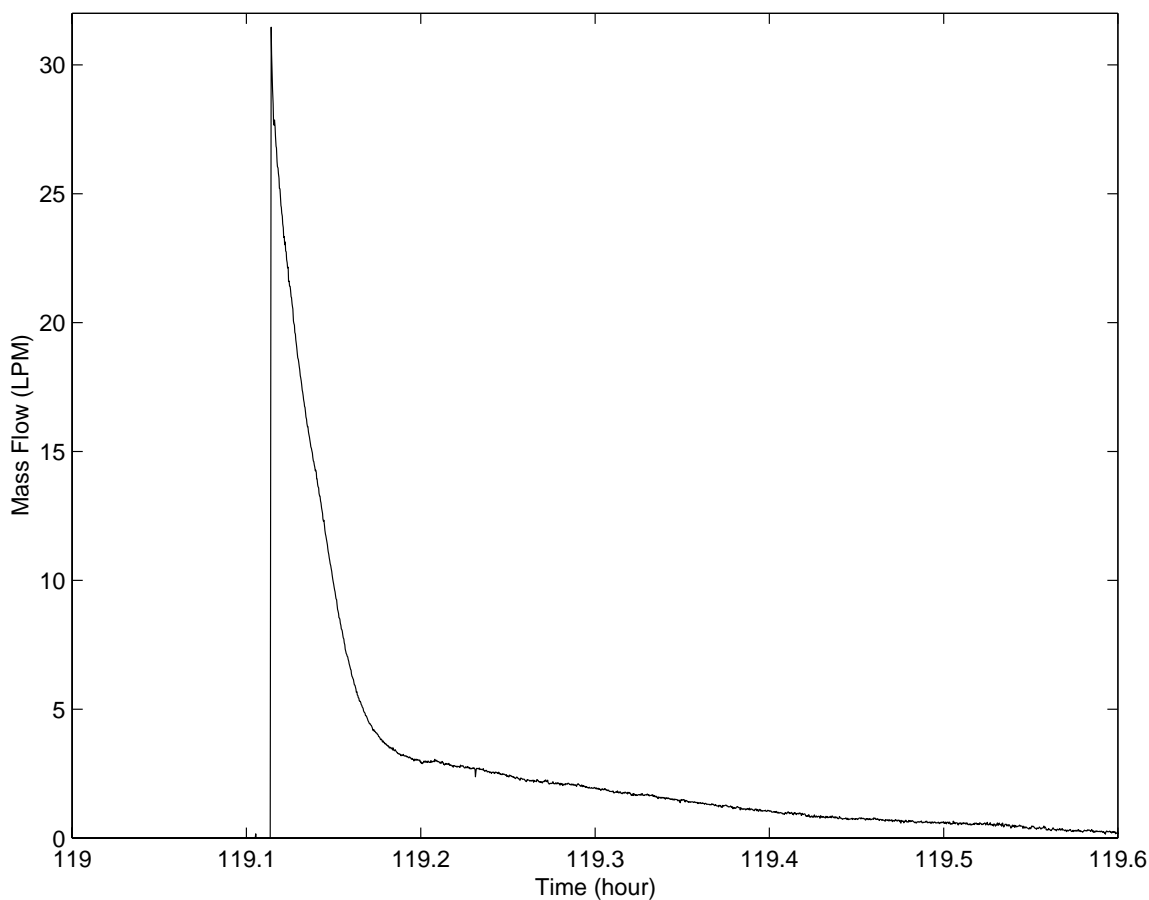


Figure 60. Time evolution of volumetric flow rate during propane hydrate dissociation for the sample with 25% glass beads.

Experimental Shear Flow Device

A shear flow device was fabricated for studying shearing of various fluids. The device is capable of generating a constant shearing rate in the entire fluid body being studied. Figure 61 shows the schematics of the device. Two rubber timing belt pass over pulleys with matching pitches that rotate in the same sense. Hence the belts move in opposite directions in the viewing section. The fluid is contained in the space between the two Plexiglas sheets and the aluminum block. Circular arches (two at each end) are machined in the aluminum block at the top and bottom of the apparatus. These semicircular sections ensure that the fluid is subjected to a constant shear flow field. The circular arches also reduce the end effects by facilitating smooth separation and reentry of the flows at the top and bottom.

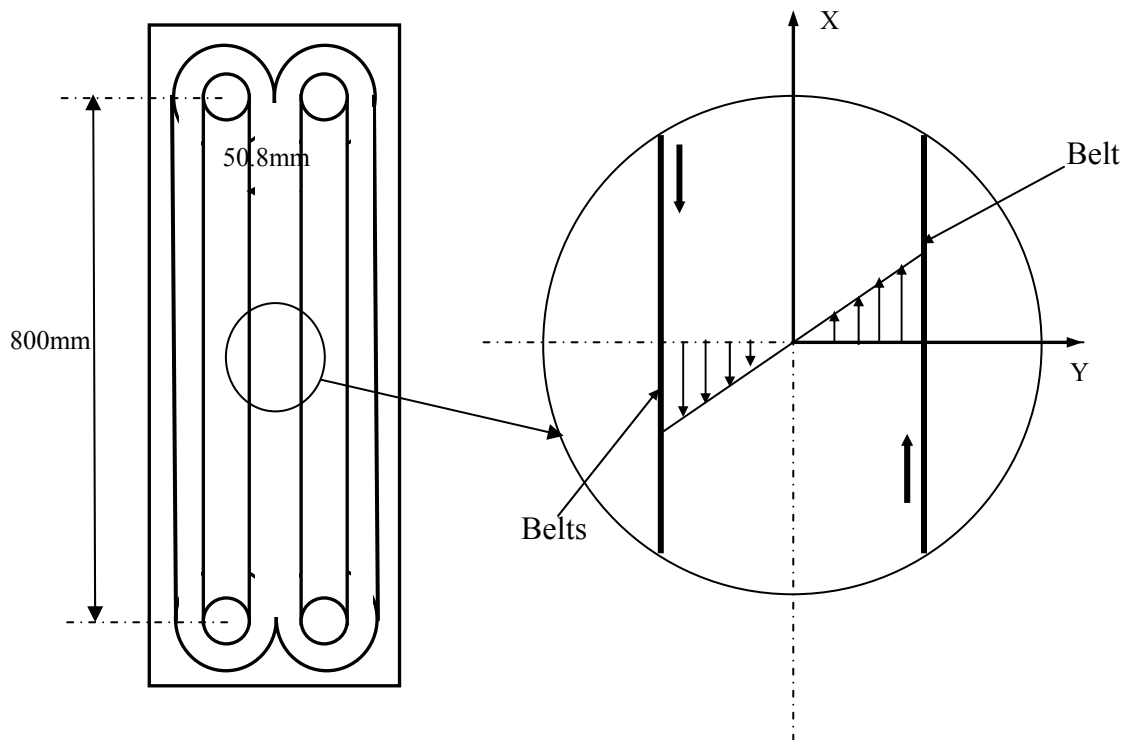


Figure 61. Schematic of simple shear flow apparatus.

The test window is in the middle of the viewing section. Sprockets are fixed to the shafts attached to the bottom pulley and these are driven by a chain drive attached to a DC motor. The speeds of motor can be controlled electronically. The gap between the belts is 50.8 mm, and the width of each belt is 101.6 mm. The belts speed is determined by rotation of pulleys that is measured by a rotation meter. Pictures of the fabricated shear flow setup are displayed in Figure 62.

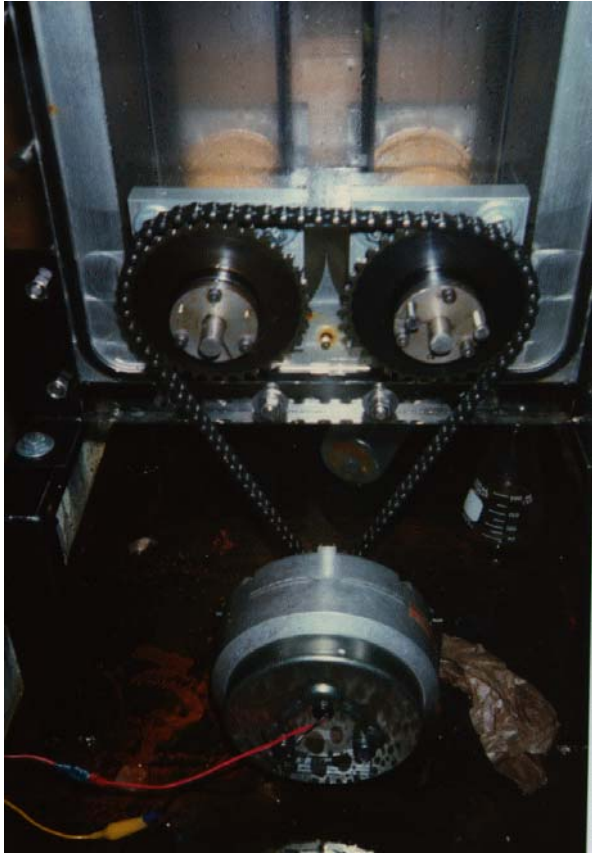
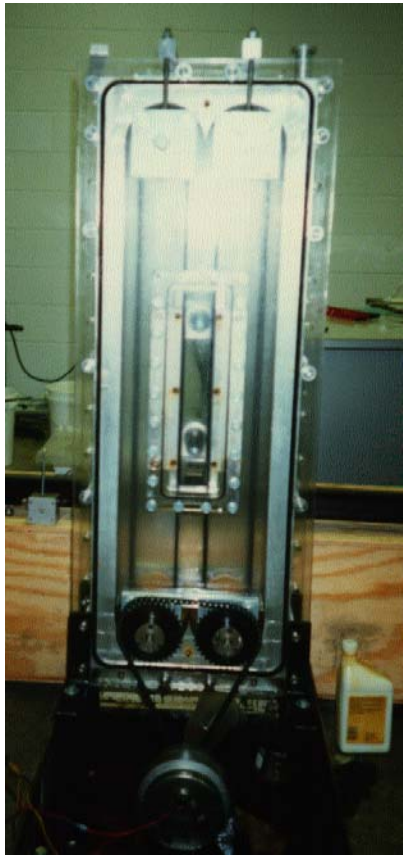


Figure 62. Pictures of simple shear flow apparatus.

PLANS FOR THE NEXT YEAR

- To perform additional set of experimental study of the propane hydrate formation and dissociation process with higher concentration of glass beads.
- To complete the computational model for evaluating the details of reservoir conditions during the hydrate formation and dissociation without the linearization assumption.
- To complete the thermodynamically consistent model for multiphase flows.
- To simulate multiphase flows during hydrate dissociation in fractures.
- To assess the sea floor stability during hydrate dissociation.

REFERENCES

PUBLICATIONS

Journals

Cao, J. and Ahmadi, G., "Gas-Particle Two-Phase Flow in Horizontal and Inclined Ducts," International Journal of Engineering Science, Vol. 38, pp. 1961-1981 (2000).

Ji, C., Ahmadi, G., and Smith, D.H., "Natural Gas Production from Hydrate Decomposition by Depressurization," Chemical Engineering Science, Vol. 56, pp. 5801-5814 (2001).

Ji, C., Ahmadi, G. and Smith, D.H., Experimental and Computational Study of Fluid Flow Phenomena in Carbon Dioxide Sequestration, Journal of Energy and Environment Research, Vol. 2, pp. 99-108 (2002).

Ji, C., Ahmadi, G. and Smith, D.H., Constant Rate Natural Gas Production from a Well in a Hydrate Reservoir, Energy conversion and Management, Vol. 44, pp. 2403-2423 (2003).

Conferences

C. Ji, G. Ahmadi and D.H. Smith, "Computational Simulation for Natural Gas Production from Hydrate Decomposition," Annual Technical Meeting of the Center for Advanced Material Processing (CAMP), Lake Placid, NY, May 23-25, 2000.

Sadiki, A. and Ahmadi, G., "A Thermodynamical Formulation for Chemically Active Multiphase Flows," Trends in Numerical and Physical Modeling for Industrial Multiphase Flows, Institut d'Etudes Scientifiques de Cargese (Corse), France. September 26-28, 2001.

Zhang, X. and Ahmadi, G., "Gas-Particle Two-Phase Flow in a Horizontal Channel," 20th Annual Conference of the American Association for Aerosol Research, AAAR 2001, Portland, Oregon, October 15-19, 2001.

G. Ahmadi, "Fundamentals of Natural Gas Flow in a Hydrate Reservoir," Methane Hydrates Interagency R&D Conference, Washington, DC, March 20-22, 2002.

K. Nazridoust, T. White, C. Ji, G. Ahmadi, D.H. Smith, M. Dean "Natural Gas Production from Hydrate Dissociation," Annual Technical Meeting of the Center for Advanced Material Processing (CAMP), Saratoga Spring, NY, May 13-15, 2002.

C. Ji, G. Ahmadi, W. Zhang and D.H. Smith, "Natural Gas Production from Hydrate Dissociation-A Comparison of Axisymmetric Models," 4th International Conference on Gas Hydrate, Yokohama, Japan, May 19-23, 2002.

K. Nazridoust, T. White, C. Ji, G. Ahmadi, M. Dean and D.H. Smith, "A Computer Model for Natural Gas Production from Hydrate Reservoirs," 21st Annual Conference of the American Association for Aerosol Research, AAAR 2002, Charlotte, NC, October 7-11, 2002.

D.H. Smith, G. Ahmadi, Chuang Ji, G. Bromhal, and M. Ferer, "Experimental and Numerical Studies of Gas-liquid Displacement In Flow Cells, With Application To Carbon Dioxide Sequestration In Brine Fields," FEDSM2002-31296, Proceedings of ASME FEDSM'02, ASME Fluids Engineering Division Summer Meeting, Montreal, Quebec, Canada, July 14-18, 2002.

K. Nazridoust, T. White, C. Ji, G. Ahmadi, M. Dean and D.H. Smith, "A Computer Model for Natural Gas Production from Hydrate Reservoirs," 21st Annual Conference of the American Association for Aerosol Research, AAAR 2002, Charlotte, NC, October 7-11, 2002.

E. M. Noto and G. Ahmadi, "A Preliminary Study of Rheological Behavior of Bauxite Residue," 21st Annual Conference of the American Association for Aerosol Research, AAAR 2002, Charlotte, NC, October 7-11, 2002.

G. Ahmadi, A. R. Mazaheri and D.H. Smith, "Multiphase Flow Through Poro-Elastic Media-A Continuum Model," IMECE2002-32492, Proceedings of ASME International Mechanical Engineering Congress, New Orleans, LA, November 17-22, 2002.